Ph.D. thesis supervisor: Prof. RNDr. Jiří Horáček, DrSc

Work partially contained in:

Chapter 3:
M. Čížek, J. Horáček, H.-D. Meyer, 1999, *Comp. Phys. Comm.*, submited.
Chapter 4:
M. Čížek, J. Horáček, W. Domcke, 1998, *J. Phys. B* **31**, 2571-2583.
Chapter 5:
J. Horáček, M. Čížek, W. Domcke, 1998, *Theor. Chem. Acc.* **100**, 31-35.
M. Čížek, J. Horáček, W. Domcke, 1999, *Phys. Rev. A* **60**, 2873-2881.

Author's address: Institute of Theoretical Physics,
Faculty of Mathematics and Physics,
Charles University,
V Holešovičkách 2,
180 00 Praha 8,
Czech Republic

e-mail: cizek@mbox.troja.mff.cuni.cz

Acknowledgements

I would like to thank all the people at many different places, without whose help and inspiration this work could not be possible in the present form.

First of all I would like to express my sincere gratitude to Jiří Horáček for his friendly approach and for finding interesting subjects for scientific exploration. I would also like to thank him for his support which helped me to establish interesting international contacts.

I thank professor Wolfgang Domcke who supervised my DAAD scholarship in Düsseldorf and whose ideas also influenced significantly this work. Thanks also to other people in Institute for Theoretical Chemistry on Heinrich Heine University of Düesseldorf for generous help and friendly environment.

I spent almost one year in Utrecht, having oportunity to broaden my knowledge in physics and possibility to see remarkable experiments on cold collisions of laser manipulated atoms. I would like to thank Henrik Rudolph, Arend Niehaus, Mark Pieksma and Morten Lundsgaard for stimulating discussions and especially to Peter van der Straten for having patience to answer all my questions about laser cooling and cold collisions. I could also experience almost one year of life in Netherlands together with my wife which I appreciate greatly. I therefore gratefully acknowledge help of Henrik Rudolph without whom I would never had this opportunity.

Part of my calculations of electron spectra for associative detachment processes have been carried out in Kaiserslautern in the group of professor Hartmut Hotop. I thank him for his hospitality and for the idea to simulate the effects which experimental set up may have on the electron spectra. Without these simulations I would never think that experimental conditions may enhance some effect to be seen better than under idealized conditions. I would also like to thank Frank Thiel for guiding me through the new environment in University of Kaiserslautern.

Last but not least I would like to thank to professor Ilya Fabrikant from Nebraska for sending me data for construction of the model for HF.

This work was partially supported by grant from "Fond rozvoje vysokých škol". I thank to DAAD, Utrecht University and Forschersgruppe "Niederenergetische Elektronenstreuprozesse" for finantial support during the time I spent in Duesseldorf, Utrecht and Kaiserslautern.

Contents

Chapter 1

Introduction

In this chapter we introduce the subject of the thesis—low energy resonant collisions. First we show the processes of interest. Then we proceed with a few notes about their applications and about the history of their theoretical investigation. Finally, the main objectives of this thesis are outlined.

Resonant phenomena are quite common in the scattering of particles and/or light and are often encountered in many branches of physics. Main subject of this work is the investigation of the low-energy resonant processes occurring in electron-molecule and ion-atom collisions. General scheme for such resonant process is

$$\begin{array}{rl} & \mathrm{e}^- + AB(\nu,l) \\ \text{or} & A+B^- \end{array} \rightarrow \left(AB^-\right) \rightarrow \begin{array}{rl} & \mathrm{e}^- + AB(\nu,l) \\ \text{or} & A+B^- \\ \text{or} & A+B+\mathrm{e}^-, \end{array}$$

where A and B substitutes an arbitrary atom. This scheme contains vibrational excitation (VE) of the molecule AB by electron impact, dissociative attachment (DA) of an electron to the molecule, the associative detachment (AD) and collisional detachment (CD) of the negative ion B^- in the collision with the atom A:

$$\begin{array}{rcll} \mathrm{e}^- + AB(\nu,l) & \rightarrow & \mathrm{e}^- + AB(\nu',l'), & \text{(VE)} \\ \mathrm{e}^- + AB(\nu,l) & \rightarrow & A+B^-, & \text{(DA)} \\ A+B^- & \rightarrow & \mathrm{e}^- + AB(\nu,l), & \text{(AD)} \\ A+B^- & \rightarrow & A+B+\mathrm{e}^-. & \text{(CD)} \end{array}$$

Formation of the unstable collision complex AB^- is responsible for the resonant nature of these processes and the cross sections attain often unexpectedly high values. In the last chapter we will investigate also another resonant processes, not included in the scheme above, the process of Penning ionization (PI) and associative ionization (AI)

$$\begin{array}{rcll} A+B^* & \rightarrow & \mathrm{e}^- + A^+ + B & \text{(PI)} \\ A+B^* & \rightarrow & \mathrm{e}^- + AB^+(\nu,l) & \text{(AI)} \end{array}$$

occurring in collisions of excited atoms[1]. These processes are very similar to collisional and associative detachment and also the theory underlying their description is to large extent similar.

[1] Both atoms A and B can actually be in excited state.

The above schemes contain a broad variety of processes of great practical interest. Such collisional reactions are often encountered in plasma physics both in laboratory and nature including physics of ionosphere, stellar atmospheres and nebulae in the outer space. The cross sections determine equilibrium densities of electrons, ions, atoms and molecules in such environments. Spectrum of light coming from distant nebulae is determined by distribution of states of H_2 molecules which can be formed by associative detachment process in $H+H^-$ collisions. Dissociative attachment process may serve as source for negative ion beams used for loading of thermonuclear devices or for electro-magnetic propulsion of space vehicles. AD and DA are found to be of importance in the chemistry of flames and play also important roles in gas lasers (see [1] and references therein). Additionally, the reactions are of considerable interest as destruction mechanism of halogen ions of anthropogenic origin in the ionosphere. More about applications of dissociative electron attachment to molecules including radiocarbon dating and very sensitive detection of explosives or drugs can be found for example in the review paper [2].

Cross sections of the resonant processes often exhibit pronounced features interesting from the theoretical point of view. For some molecules, the cross sections for VE attains high values in a very vicinity of the threshold. Such a phenomenon is called threshold peak and was observed for the first time by Rohr and Linder in 1976 [3]. The cross sections for AD, DA and VE are not smooth functions of the collision energy and abrupt changes of a slope called Wigner cusps are often observed near opening of a new channels in the reaction. In spite of two decades of theoretical study these phenomena are still not fully comprehended. The most successful approach, which describes qualitatively well all the observed features, is the nonlocal resonance model reviewed by Domcke in [4].

The main goal of this work is to generalize existing methods for numerical solution of the scattering equations in the presence of nonlocal potential and to apply them to calculation of associative detachment cross sections. Such a calculation requires inclusion of many partial waves and has never been done before in its full complexity. Previous calculations for associative detachment have been done using local complex approximation. This approximation proved to fail for certain systems [5, 6]. On the other hand, all fully nonlocal calculations done up to now consider the s-wave only. This is justified for VE and DA processes where electron collides with molecule AB, which may be assumed to be in the ground state. On the contrary, many partial waves contribute to the cross section for associative detachment process even for small collision energies of the order 100 meV. We are not aware of any other calculation including several partial waves in nonlocal resonance model.

Our generalization of the numerical methods for treating many partial waves in the nonlocal scattering problem enables us to consider in addition to associative detachment also electron scattering on hot molecules, where many ro-vibrational states are populated, and to compare the results with the measurements of Allan and Wong for several systems [7, 8].

We start with brief review of theory in the Chapter 2. The chapter contains mainly the results derived elsewhere [9, 4, 10]. We have introduced the partial wave decomposition of the quantities important for the description of nonlocal dynamics of the resonant processes originally derived for Penning and associative detachment by Bieniek [10] into resonant theory of electron-molecule scattering reviewed by Domcke in [4] obtaining thus consistent description of all AD, DA and VE processes.

In Chapter 3 we briefly review the methods for the numerical treatment of the nonlocal dynamics arising in the description of the processes of interest and we introduce some generalizations and improvements. We pay special attention to the numerical solution of the nonlocal Lippmann-Schwinger equation and we develop a new method, called here the generalized Schwinger-Lanczos algorithm. The method is tested and found to be converging faster than original version of the algorithm. Unfortunately, the new method requires more calculations and when tested for computer time demands it proves to be of almost the same efficiency as original one.

Following chapters contain the applications of the theory and numerical procedures to several systems of both fundamental and practical interest. Chapter 4 is devoted to processes proceeding via formation of H_2^- resonance complex. Such processes are important mainly in astrophysical applications. In Chapter 5 we investigate resonance processes for hydrogen halides with one additional electron. These processes are rich in threshold phenomena due to strong interaction of the additional electron with the electrical dipole of the molecule. Most of the chapter is devoted to HCl^- but we also investigate the electron spectra for associative detachment in collisions of other negative halogen ions with hydrogen in connection with the experiment planned in Kaiserslautern. The theoretical results are important for planning and building of appropriate experimental setup for investigation of the effects the nonlocal dynamics has on the spectra. Models for the description of the systems of interest have previously been constructed fitting *ab initio* electron-molecule scattering data for fixed positions of nuclei. Here we adjust the long range part of the models to new *ab initio* potential data. It was previously believed that this part of the potential does not have significant influence on electron molecule scattering but it considerably influences AD process for very low energies. We show that omitting the proper long range behaviour may cause disappearance of interesting resonant features from VE cross sections, recently seen in experiments [11, 12]. We hope that our calculations will help to close in near future more than 20 years of exciting investigation of resonant and threshold effects in scattering of electrons on hydrogen halides started with already mentioned discovery of threshold peaks in VE cross section in 1976 and cusp structure in DA cross section in 1977 [13].

In Chapter 6, we give a few remarks on Penning and associative ionization and we present a model study of electron spectra for collisions of two metastable helium atoms. The process is important in collision experiments with laser-cooled helium and its dynamics determines the possibility of obtaining the Bose-Einstein condensation with helium in magneto-optical traps. The system is also of considerable theoretical interest because of involvement of more resonant states.

We conclude our work with short account of results and future prospects in Chapter 7. Appendix A gives some formulas for Wigner 3j symbols and spherical harmonics used mainly in the Chapter 2, Appendix B contains the description of the models used in the calculations for different systems and Appendix C is devoted to scattering in the local complex potential or several coupled complex potentials; formulae derived there are relevant for the Chapter 6.

Notation and conventions

Atomic units ($e = \hbar = m_e = 1$) are used throughout the work. The scattering processes are described in the framework of time-independent resonant theory as given in [14, 15]. Because of specific nature of atomic collisions we use following modification of bracket notation. To distinguish between the vectors from Hilbert space of electrons moving in the potential field of the nuclei fixed in the space and the vectors describing the nuclei in the centre of mass system we denote former (electrons) with round bra and kets like $(\phi|$ or $|\psi)$ and the later (nuclei) with $\langle\phi|$ or $|\psi\rangle$. Whenever the vectors from complete Hilbert space, describing both electrons and nuclei are needed, we use double ket symbols like $|\Psi\rangle\!\rangle$. In the Chapter 2 we use $|\psi\rangle$ symbol only for three dimensional wave function but the same notation is used for radial wave functions in Chapter 3. We hope this will cause no confusion.

Chapter 2

Theoretical description of resonant processes

2.1 Resonant electron-molecule collisions

Let us first investigate the scattering of an electron by a molecular target. In this section we will assume that the positions of the atomic nuclei in the molecule are fixed in space and that only electronic coordinates are dynamic variables. Nuclear coordinates are just parameters in the Hamiltonian and we will suppress them in notation throughout this section. Theoretical description of such a process is in general quite complicated task since the target is a many-body system. It is, however, possible to reduce the problem to an effective one-body scattering problem using many-body optical potential formalism[1] (see [16] and references therein). The optical potential V_{opt} is energy dependent, nonlocal and in general complex. When the scattering electron is at infinity $V_{\text{opt}}(\vec{r} \to \infty) = V_0$, where V_0 is the Born-Oppenheimer potential of the target molecule. In scattering calculations it is advantageous to shift the energy scale so that potential goes to zero at infinity; $V(\vec{r}) = V_{\text{opt}}(\vec{r}) - V_0$.

Resonant phenomena are common in electron-molecule scattering. For energy near resonance the electron is captured into unstable quasi-bound state. The cross sections attain high values and vary rapidly. The wave function near a resonance can well be described by square integrable function since the amplitude of oscillatory tail for large $\vec{r}$ is much smaller than the values of the wave function in the vicinity of the molecule. This suggests the idea of subtraction of a small part $\mathcal{Q}$ of Hilbert space $\mathcal{H}_{\text{el}}$ containing the most of the resonance wave function to get rid of the fast variations of scattering quantities with changes of the energy and (which is important in the next section) also with changes of inter-nuclear coordinates. Scattering in the remaining non-resonant part $\mathcal{P}$ of the Hilbert space is usually called background scattering. The separation of the scattering process into $\mathcal{H}_{\text{el}} = \mathcal{P} \oplus \mathcal{Q}$ can be performed using the projection formalism of Feshbach [17] developed originally in nuclear physics. In the following we show briefly how to achieve this separation for wave function and scattering T-matrix. The details

[1] This reduction is not necessary for the formulation of the following projection operator treatment of the problem, but it simplifies some formulas.

can be find in the works of Domcke [18, 4].

Let us denote by Q the projection operator on the resonance part $\mathcal{Q}$ and by P the projection on the background part $\mathcal{P}$ of $\mathcal{H}_{\text{el}}$ so that

$$P + Q = 1, \qquad PQ = QP = 0. \tag{2.1}$$

Our goal to separate the scattering process into resonant and background parts will be achieved in three steps. First, we solve the problem of "a free particle" in $\mathcal{P}$ space, or more precisely potential free scattering with additional constraint $Q|\bar{\epsilon}^{(\pm)}) = 0$. Second, we construct background scattering wave functions $|\phi_\epsilon^{(\pm)})$, which describe scattering of an electron on potential V with the constraint $Q|\phi_\epsilon^{(\pm)}) = 0$. The third, and the last, step is to achieve the separation of the complete scattering wave function $|\psi^{(\pm)})$ obeying the Lippmann-Schwinger equation

$$|\psi^{(\pm)}) = |\vec{\epsilon}) + G_0^{(\pm)}(\epsilon)V|\psi^{(\pm)}) \tag{2.2}$$

into $\mathcal{Q}$ and $\mathcal{P}$ parts. Here $|\vec{\epsilon})$ denotes the energy-normalized free electron wave function and the vector $\vec{\epsilon}$ describes the energy and the direction of the incoming electron. Hamiltonian $H_{\text{el}} = K + V$ (K is the kinetic energy operator of the electron) of the electron-molecule scattering can be divided into four parts

$$H_{\text{el}} = K + (K_P - K) + (H_P - K_P) + (H_{\text{el}} - H_P), \tag{2.3}$$

where subscript P denotes the projection of an operator A into $\mathcal{P}$: $A_P \equiv PAP$. Using two-potential formula [14] we can write:

$$\begin{aligned} |\bar{\epsilon}^{(\pm)}) &= |\vec{\epsilon}) + G_0^{(\pm)}(\epsilon)[K_P - K]|\bar{\epsilon}^{(\pm)}), && (2.4)\\ |\phi_\epsilon^{(\pm)}) &= |\bar{\epsilon}^{(\pm)}) + \bar{G}_0^{(\pm)}(\epsilon)[H_P - K_P]|\phi_\epsilon^{(\pm)}), && (2.5)\\ |\psi^{(\pm)}) &= |\phi_\epsilon^{(\pm)}) + \bar{G}_{\text{bg}}^{(\pm)}(\epsilon)[H_{\text{el}} - H_P]|\psi^{(\pm)}), && (2.6) \end{aligned}$$

where $G_0^{(\pm)}$, $\bar{G}_0^{(\pm)}$ and $\bar{G}_{\text{bg}}^{(\pm)}$ are Green functions for Hamiltonians K, K_P and H_P respectively. It is possible to show that (2.4) and (2.5) imply $Q|\bar{\epsilon}^{(\pm)}) = Q|\phi_\epsilon^{(\pm)}) = 0$. Note that $|\vec{\epsilon})$, $|\bar{\epsilon}^{(\pm)})$, $|\phi_\epsilon^{(\pm)})$ and $|\psi^{(\pm)})$ are eigenfunctions of the operators K, K_P, H_P and H_{el} respectively, corresponding to the eigenvalue ϵ. Repeated use of the two-potential formula for the T-matrix yields the separation of the T-matrix into the background and resonance terms:

$$\begin{aligned} T(\vec{\epsilon}', \vec{\epsilon}) &= T_{\text{bg}}(\vec{\epsilon}', \vec{\epsilon}) + T_{\text{res}}(\vec{\epsilon}', \vec{\epsilon}), && (2.7)\\ T_{\text{bg}}(\vec{\epsilon}', \vec{\epsilon}) &= (\vec{\epsilon}'|K_P - K|\bar{\epsilon}^{(+)}) + (\bar{\epsilon}'^{(-)}|H_P - K_P|\phi_\epsilon^{(+)}), && (2.8)\\ T_{\text{res}}(\vec{\epsilon}', \vec{\epsilon}) &= (\phi_{\epsilon'}^{(-)}|H_{\text{el}} - H_P|\psi^{(+)}) = (\phi_{\epsilon'}^{(-)}|PH_{\text{el}}Q|\psi^{(+)}). && (2.9) \end{aligned}$$

The background scattering T-matrix T_{bg} consists of two terms. The first appears in consequence of the additional condition $Q|\phi_\epsilon^{(+)}) = 0$ and is called orthogonality scattering T-matrix and the second is so called direct scattering T-matrix. The resonance term T_{res} can be expressed in terms of background scattering functions $|\phi_\epsilon^{(\pm)})$ if we formally solve the equation (2.6), first applying the projection operators P and Q on equation (2.6):

$$\begin{aligned} P|\psi^{(\pm)}) &= |\phi_\epsilon^{(\pm)}) + P\bar{G}_{\text{bg}}^{(\pm)}(\epsilon)PH_{\text{el}}Q|\psi^{(\pm)}), && (2.10)\\ Q|\psi^{(\pm)}) &= (\epsilon \pm i\varepsilon)^{-1}[H_Q + QH_{\text{el}}P]|\psi^{(\pm)}), && (2.11) \end{aligned}$$

where ε is the usual positive infinitesimal. After substitution for $P|\psi^{(\pm)})$ from (2.10) and some rearrangements we obtain from (2.11)

$$Q|\psi^{(\pm)}) = [\epsilon - H_Q - QH_{\mathrm{el}}P\bar{G}^{(\pm)}_{\mathrm{bg}}(\epsilon)PH_{\mathrm{el}}Q \pm i\varepsilon]^{-1}QH_{\mathrm{el}}P|\phi^{(\pm)}_{\epsilon}). \tag{2.12}$$

Substitution of this expression for Q-space part of $|\psi^{(+)})$ into (2.9) yields

$$T_{\mathrm{res}}(\vec{\epsilon}', \vec{\epsilon}) = (\phi^{(-)}_{\epsilon'}|PH_{\mathrm{el}}Q[\epsilon - H_Q - QH_{\mathrm{el}}P\bar{G}^{(+)}_{\mathrm{bg}}(\epsilon)PH_{\mathrm{el}}Q + i\varepsilon]^{-1}QH_{\mathrm{el}}P|\phi^{(+)}_{\epsilon}). \tag{2.13}$$

The treatment so far was at least in principle exact[2]. At this point we introduce certain assumptions which are reasonably valid for many interesting systems. First, we assume that the resonance part $\mathcal{Q}$ contains only one state $|\phi_{\mathrm{d}})$ (often called discrete state), i. e. $Q = |\phi_{\mathrm{d}})(\phi_{\mathrm{d}}|$. The Second assumption is that the target molecule can not be excited electronically for the energy range of interest and that there are no bound states in background scattering problem so that background scattering states form a complete set in $\mathcal{P}$, i. e.

$$P = \int \mathrm{d}\epsilon \mathrm{d}\hat{\epsilon}|\phi^{(\pm)}_{\epsilon})(\phi^{(\pm)}_{\epsilon}|, \tag{2.14}$$

where $\int d\hat{\epsilon}$ denotes the integration over direction of $\vec{\epsilon}$. The generalization for more discrete states and/or more continua is straightforward. Inclusion of bound states, which would be necessary for description of Penning ionization process, would cause no principle problems. Most of the results shown below are valid also for this case if we suppose that the $\int \mathrm{d}\epsilon$ contains also the sum over the bound states.

Let us define the discrete state energy E_{d}, the discrete-state-continuum coupling $V_{\mathrm{d}\vec{\epsilon}}$, and the level-shift operator $F(\epsilon)$ as follows:

$$\begin{aligned} E_{\mathrm{d}} &= (\phi_{\mathrm{d}}|H_{\mathrm{el}}|\phi_{\mathrm{d}}), & (2.15)\\ V_{\mathrm{d}\vec{\epsilon}} &= (\phi_{\mathrm{d}}|H_{\mathrm{el}}|\phi^{(+)}_{\epsilon}), & (2.16)\\ F(\epsilon) &= (\phi_{\mathrm{d}}|H_{\mathrm{el}}P\bar{G}^{(+)}_{\mathrm{bg}}(\epsilon)PH_{\mathrm{el}}|\phi_{\mathrm{d}}) \equiv \Delta(\epsilon) - \tfrac{i}{2}\Gamma(\epsilon). & (2.17) \end{aligned}$$

If we employ relation (2.14) and the fact that $|\phi^{(+)}_{\epsilon})$ diagonalize operator $\bar{G}^{(+)}_{\mathrm{bg}}$, we can write the real and the imaginary parts of the level-shift $F(\epsilon)$ as:

$$\begin{aligned} \Gamma(\epsilon) &= 2\pi \int \mathrm{d}\hat{\epsilon}|V_{\mathrm{d}\vec{\epsilon}}|^2, & (2.18)\\ \Delta(\epsilon) &= \tfrac{1}{2\pi}\wp \int \mathrm{d}\epsilon' \Gamma(\epsilon')/(\epsilon - \epsilon'). & (2.19) \end{aligned}$$

The well known formula $(x + i\varepsilon)^{-1} = \wp\frac{1}{x} - i\pi\delta(x)$ has been used to obtain this result. The quantities E_{d} and $V_{\mathrm{d}\vec{\epsilon}}$ fully describe resonant scattering

$$T_{\mathrm{res}}(\vec{\epsilon}', \vec{\epsilon}) = V^*_{\mathrm{d}\vec{\epsilon}'}[\epsilon - E_{\mathrm{d}} - F(\epsilon)]^{-1}V_{\mathrm{d}\vec{\epsilon}}. \tag{2.20}$$

[2]Of course, certain approximations have to be introduced when solving the background scattering problem.

If we are interested only in integral scattering cross section (averaged over incoming directions) we do not need information about direction contained in $V_{\mathrm{d}\vec{\epsilon}}$ and the resonant total scattering cross section σ_{res} is fully described by E_{d} and $\Gamma(\epsilon)$:

$$\sigma_{\mathrm{res}} = \tfrac{2\pi}{\epsilon}\frac{(\Gamma(\epsilon)/2)^2}{[\epsilon - E_{\mathrm{d}} - \Delta(\epsilon)]^2 + [\Gamma(\epsilon)/2]^2}. \tag{2.21}$$

This is the famous Breit-Wigner resonance formula (if we neglect ϵ-dependence of Δ and Γ). It is possible to show [9] that the decomposition into background and resonance term can be performed also for eigenphases (the phases of eigenvalues of the S-matrix)

$$\delta = \delta_{\mathrm{bg}} - \tan^{-1}\frac{\Gamma(\epsilon)/2}{\epsilon - E_{\mathrm{d}} - \Delta(\epsilon)}. \tag{2.22}$$

We demonstrated that the electron-molecule scattering quantities can be decomposed into slowly varying and usually small background term and a resonant term, containing all singularities and fully described by quantities . We would like to stress that this decomposition is not unique and that there is no apriory choice for Q operator (or for $|\phi_{\mathrm{d}})$). It has been demonstrated [9, 16] that sensitive choice of $|\phi_{\mathrm{d}})$ based on physical intuition or resonance theory indeed gives a reasonable decomposition, removing fast variations from background scattering. The procedure outlined above provides not only formal theoretical separation of the scattering problem into resonant and background part,but it can also be applied numerically to construct the quantities E_{d} and Δ and Γ [9, 16] which contain all information about the resonance behaviour.

Let us finally express the Hamiltonian H_{el} in terms of E_{d}, $V_{\mathrm{d}\vec{\epsilon}}$ and basis functions $|\phi_{\mathrm{d}})$, $|\phi_{\vec{\epsilon}}^{(+)})$ in $\mathcal{H}_{\mathrm{el}}$. Formulas for P and Q together with $H_P|\phi_{\vec{\epsilon}}^{(+)}) = \epsilon|\phi_{\vec{\epsilon}}^{(+)})$ and with the orthogonality relation $(\phi_{\mathrm{d}}|\phi_{\vec{\epsilon}}^{(+)}) = 0$ readily yield

$$\begin{aligned} H_{\mathrm{el}} &= |\phi_{\mathrm{d}})V_{\mathrm{d}}(\phi_{\mathrm{d}}| + \int \mathrm{d}\epsilon \mathrm{d}\hat{\epsilon}|\phi_{\vec{\epsilon}}^{(+)})[\epsilon + V_0](\phi_{\vec{\epsilon}}^{(+)}| + \\ &\quad + \int \mathrm{d}\epsilon \mathrm{d}\hat{\epsilon}|\phi_{\mathrm{d}})V_{\mathrm{d}\vec{\epsilon}}(\phi_{\vec{\epsilon}}^{(+)}| + \int \mathrm{d}\epsilon \mathrm{d}\hat{\epsilon}|\phi_{\vec{\epsilon}}^{(+)})V_{\mathrm{d}\vec{\epsilon}}^{*}(\phi_{\mathrm{d}}|, \end{aligned} \tag{2.23}$$

where for future convenience we again introduced the Born-Oppenheimer potential energy V_0 of the target molecule. We had to shift also the discrete state energy $E_{\mathrm{d}} \rightarrow V_{\mathrm{d}} \equiv E_{\mathrm{d}} + V_0$.

2.2 Dynamics of resonant processes

The equations describing resonant processes in electron-molecule and ion-atom scattering will be derived using resonance formalism in this chapter. Simplified one dimensional case, when all rotational degrees of freedom are neglected, is treated for example in the review [4]. Here we generalize the nonlocal treatment to include also the rotations. We owe much to the article of Bieniek [10] where this problem is addressed for the Penning ionization. The formulae for the associative detachment and the dissociative attachment process are obtained directly from his treatment. Vibrational excitation needs a little bit of generalization.

First, the nuclear coordinates has to be included into dynamical description of the system. The respective Hilbert space is $\mathcal{H} = \mathcal{H}_{\rm el} \otimes \mathcal{H}_{\rm N}$. The separation of $\mathcal{H}_{\rm el}$ into $\mathcal{P}$ and $\mathcal{Q}$ (and corresponding operators P and Q) defined in the previous section can be extended to $\mathcal{H}$ in an obvious way, i. e. $\mathcal{P} \to \mathcal{P} \otimes \mathcal{H}_{\rm N}$, $P \to P \otimes 1$ and the same for $\mathcal{Q}$. We will use the same notation $\mathcal{P}$, $\mathcal{Q}$ (P, Q) for these new spaces (operators). It is important that the relations (2.1) are fulfilled for the extended operators P, Q. The Hamiltonian H describing the system is

$$H = T_{\rm N} + H_{\rm el}, \tag{2.24}$$

where $T_{\rm N} = -\frac{1}{2\mu}\triangle$ is the kinetic energy operator for the nuclei. It can be separated into two parts $H = H_0 + V$, where $H_0 = PHP + QHQ \equiv H_P + H_Q$ and $V = PHQ + QHP \equiv H_{PQ} + H_{QP}$. We assume, that for large inter nuclear separation R the space $\mathcal{Q}$ contains the bound state B^-, i. e. H_Q is the channel Hamiltonian for $A + B^-$ channel, whereas H_P is the channel Hamiltonian for $AB + e^-$. Initial state $|\Phi_{\rm i}^{(+)}\rangle\!\rangle$ for a scattering process of interest is eigenstate of H_0 for both channels and the Lippmann-Schwinger equation for the scattering wave function $|\Psi^{(+)}\rangle\!\rangle$ with boundary condition $|\Phi_{\rm i}^{(+)}\rangle\!\rangle$ can be written in the form

$$|\Psi^{(+)}\rangle\!\rangle = |\Phi_{\rm i}^{(+)}\rangle\!\rangle + [E - H_P + H_Q + i\varepsilon]^{-1}(H_{PQ} + H_{QP})|\Psi^{(+)}\rangle\!\rangle, \tag{2.25}$$

where ε is the usual positive infinitesimal. Multiplying this equation with Q and P we obtain the system of equations

$$\begin{aligned} Q|\Psi^{(+)}\rangle\!\rangle &= Q|\Phi_{\rm i}^{(+)}\rangle\!\rangle + G_Q H_{QP} P|\Psi^{(+)}\rangle\!\rangle & (2.26)\\ P|\Psi^{(+)}\rangle\!\rangle &= P|\Phi_{\rm i}^{(+)}\rangle\!\rangle + G_P H_{PQ} Q|\Psi^{(+)}\rangle\!\rangle, & (2.27) \end{aligned}$$

where we have introduced the Green functions $G_Q = Q(E - H_Q + i\varepsilon)^{-1}Q$ and $G_P = P(E - H_P + i\varepsilon)^{-1}P$. Substitution of (2.27) into (2.26) gives

$$Q|\Psi^{(+)}\rangle\!\rangle = Q|\Phi_{\rm i}^{(+)}\rangle\!\rangle + G_Q H_{QP} P|\Phi_{\rm i}^{(+)}\rangle\!\rangle + G_Q H_{QP} G_P H_{PQ} Q|\Psi^{(+)}\rangle\!\rangle. \tag{2.28}$$

We thus reduced the scattering problem in the complete Hilbert space $\mathcal{H}$ to scattering problem in its small subspace $\mathcal{Q}$. By multiplying of eq. (2.28) with $E - H_Q + i\varepsilon$ it is easy to show, that the $\mathcal{Q}$-space part of the wave function $Q|\Psi^{(+)}\rangle\!\rangle$ obeys inhomogeneous[3] Schrödinger equation with the effective Hamiltonian [19]

$$H_{\rm eff} = H_Q + H_{QP} G_P H_{PQ}. \tag{2.29}$$

We did not use any property of operators P, Q thus far. Proper choice of $|\phi_{\rm d})$ discussed in previous section ensures that the functions $|\phi_\epsilon^{(+)})$ depend weakly on R. We can thus assume that the coupling terms arising from off-diagonal matrix elements of $T_{\rm N}$ in electronic basis $|\phi_{\rm d})$, $|\phi_\epsilon^{(+)})$ are negligible. Smallness of these terms can (in principle) be verified directly and we can also take these into account as a perturbation. The assumption yields

$$[T_{\rm N}, P] = [T_{\rm N}, Q] = 0. \tag{2.30}$$

[3] the right hand side is $H_{QP} P|\Phi_{\rm i}^{(+)}\rangle\!\rangle$

Employing this relations and expression (2.23) for the electronic Hamiltonian, the formula (2.29) implies

$$H_{\text{eff}} = T_{\text{N}} + V_{\text{d}}(R) + F(E), \tag{2.31}$$

where

$$F(E) = \int \mathrm{d}\hat{\epsilon}\mathrm{d}\Omega V_{\mathrm{d}\vec{\epsilon}}(R)(E - T_{\text{N}} - V_0 - \epsilon + i\varepsilon)^{-1} V^*_{\mathrm{d}\vec{\epsilon}}(R) \tag{2.32}$$

The quantity R is the operator of the inter nuclear distance. The operator $F(E)$ is nonlocal, since in R-representation we have

$$F(E, \vec{R}, \vec{R}') = \Delta(E - T_{\text{N}} - V_0, \vec{R}, \vec{R}') - \tfrac{i}{2}\Gamma(E - T_{\text{N}} - V_0, \vec{R}, \vec{R}'), \tag{2.33}$$

where

$$\begin{aligned} \Gamma(\epsilon, \vec{R}, \vec{R}') &= 2\pi \int \mathrm{d}\hat{\epsilon} V_{\mathrm{d}\vec{\epsilon}}(\vec{R}) V^*_{\mathrm{d}\vec{\epsilon}}(\vec{R}'), &(2.34)\\ \Delta(\epsilon, \vec{R}, \vec{R}') &= \tfrac{1}{2\pi}\wp \int \mathrm{d}\epsilon' \Gamma(\epsilon', \vec{R}, \vec{R}')/(\epsilon - \epsilon'). &(2.35) \end{aligned}$$

We have separated the hermitian and anti-hermitian part of $F(E)$ using the relation $(x + i\varepsilon)^{-1} = \wp\frac{1}{x} - i\pi\delta(x)$. For $\vec{R} = \vec{R}'$ the functions (2.34) and (2.35) coincide with $\Gamma(\epsilon, R)$ and $\Delta(\epsilon, R)$ of the previous section.

Finally we write explicit formulas for the T-matrix for each of the processes AD, DA and VE in terms of $Q|\Psi^{(+)}\rangle\!\rangle$. The proper boundary condition for ionization channel $A + B^-$ is ensured by $|\Phi_i^{(\pm)}\rangle\!\rangle = |\vec{E}^{\,(+)}\rangle|\phi_{\text{d}})$ in the equation (2.25), where $|\vec{E}^{\,(+)}\rangle$ is scattering vector for the potential $V_d(R)$ and for the energy $\vec{E}$ (including incoming direction). Equation (2.28) yields

$$|\psi_I^{(+)}\rangle = |\vec{E}^{\,(+)}\rangle + G_Q^{(+)}(E)F(E)|\psi_I^{(+)}\rangle, \tag{2.36}$$

with $|\psi_I^{(+)}\rangle = (\phi_{\text{d}}|\Psi^{(+)}\rangle\!\rangle$ and $G_Q^{(+)}(E) = (E - V_{\text{d}} - T_{\text{N}} + i\varepsilon)^{-1}$. Similarly $|\Phi_{II}^{(+)}\rangle\!\rangle = |\nu_{\text{i}}\rangle|\phi_{\epsilon_{\text{i}}}^{(+)})$ for $AB + e^-$ channel and

$$|\psi_{II}^{(+)}\rangle = G_Q^{(+)}(E)V_{\mathrm{d}\vec{\epsilon}_{\text{i}}}|\nu_{\text{i}}\rangle + G_Q^{(+)}(E)F(E)|\psi_{II}^{(+)}\rangle, \tag{2.37}$$

where $|\nu_{\text{i}}\rangle$ describes initial vibrational state of the molecule AB and $\vec{\epsilon}_{\text{i}}$ refers to incoming electron. The resonant T-matrixes for AD, VE and DA are

$$\begin{aligned} T_{\text{AD}} &\equiv \langle\!\langle\Phi_{II}^{(-)}|PH_{PQ}Q|\Psi^{(+)}\rangle\!\rangle = \langle\nu_{\text{f}}|V^*_{\mathrm{d}\vec{\epsilon}_{\text{f}}}|\psi_I^{(+)}\rangle, &(2.38)\\ T_{\text{VE}} &\equiv \langle\!\langle\Phi_{II}^{(-)}|PH_{PQ}Q|\Psi^{(+)}\rangle\!\rangle = \langle\nu_{\text{f}}|V^*_{\mathrm{d}\vec{\epsilon}_{\text{f}}}|\psi_{II}^{(+)}\rangle, &(2.39)\\ T_{\text{DA}} &\equiv \langle\!\langle\Psi^{(-)}|QH_{QP}P|\Phi_{II}^{(+)}\rangle\!\rangle = \langle\psi_I^{(-)}|V_{\mathrm{d}\vec{\epsilon}_{\text{i}}}|\nu_{\text{i}}\rangle, &(2.40) \end{aligned}$$

where $\langle\psi_I^{(-)}|$ is the unique solution of

$$\langle\psi_I^{(-)}| = \langle\vec{E}^{\,(-)}| + \langle\psi_I^{(-)}|F(E)G_Q^{(+)}(E). \tag{2.41}$$

Equivalent expression for dissociative attachment T-matrix can be used for cross checking of numerical results

$$T_{\text{DA}} = \langle\!\langle\Phi_I^{(-)}|QH_{QP}P|\Psi^{(+)}\rangle\!\rangle = \langle\vec{E}^{\,(-)}|V_{\mathrm{d}\vec{\epsilon}_{\text{i}}}|\nu_{\text{i}}\rangle + \langle\vec{E}^{\,(-)}|F(E)|\psi_{II}^{(+)}\rangle, \tag{2.42}$$

where we used the formula (2.27) to express $P|\Psi^{(+)}\rangle\!\rangle$.

2.3 Partial wave expansion

Actual calculations are most often performed in partial wave expansions. This further reduces the three-dimensional problem into set of one-dimensional ones, which are more easily handled on computers (or with semi-classical methods [20, 21]). Following treatment is to some extent contained in [10], originally designed for Penning ionization. We briefly give the equivalent derivation for AD and also the formulas for DA and VE.

First of all we will derive the partial wave expansion of the discrete-continuum coupling $V_{\mathrm{d}\vec{\epsilon}}(\vec{R}\,)$ in the coordinate system fixed in the molecule and with the z-axis along the molecular symmetry axis. We will assume that the electronic state of the molecule AB has the Σ-symmetry (which is always true for the ground electronic state of diatomic molecule) and the same symmetry has also the discrete state $|\phi_{\mathrm{d}})$. This is the case for all processes studied in this work and this assumption considerably simplifies the formulas. The scattering problem then exhibits the symmetry with respect to rotations along the internuclear axis so that the partial expansion of $|\phi_{\vec{\epsilon}}^{(+)})$ is of the form

$$|\phi_{\epsilon}^{(+)}) = \sum_{l'lm} \phi_{l'lm}(\epsilon, r) Y_{l'm}(\hat{r}) Y^*_{lm}(\hat{\epsilon}). \tag{2.43}$$

With $\hat{\epsilon}$ we denote the unit vector in the direction of $\vec{\epsilon}$. Insertion of this expansion into the definition (2.16) of $V_{\mathrm{d}\vec{\epsilon}}(R)$ yields

$$V_{\mathrm{d}\vec{\epsilon}} = \sum_l Y^*_{l0}(\hat{\epsilon}) V_{\mathrm{d}\epsilon l} = \sum_l \sqrt{\frac{2l+1}{4\pi}} P_l(\cos\theta) V_{\mathrm{d}\epsilon l}, \tag{2.44}$$

where

$$V_{\mathrm{d}\epsilon l} = \sum_{l'} \int \mathrm{d}r \mathrm{d}\hat{r}\, \phi^*_{\mathrm{d}}(\vec{r}\,) H_{\mathrm{el}} \phi_{ll'm}(\epsilon, r) Y_{l'm}(\hat{r}) \bigg|_{m=0}. \tag{2.45}$$

The terms with $m \neq 0$ vanish due to Σ-symmetry. The expansion (2.44) was derived in the coordinate system fixed in the molecule and θ is the angle between $\hat{\epsilon}$ and $\hat{R}$. To rewrite the expansion into the center off mass system fixed in space we employ the relation (A.2) to obtain

$$V_{\mathrm{d}\vec{\epsilon}}(\vec{R}\,) = \sum_{lm} \sqrt{\frac{4\pi}{2l+1}} Y_{lm}(\hat{R}) Y^*_{lm}(\hat{\epsilon}) V_{\mathrm{d}\epsilon l}(R). \tag{2.46}$$

This formula, unlike the previous ones, employs the spherical harmonics $Y_{lm}(\hat{n})$ in arbitrary coordinate system, i. e. spherical coordinates are no longer measured from inter-nuclear axis $\hat{R}$.

In the second step we expand the nonlocal part F of effective Hamiltonian H_{eff}. This has been done in detail elsewhere [10] and we will only outline the derivation briefly. The potential $V_0(R)$ is spherically symmetric, which means that the Green function in the definition (2.32) is diagonal in angular momentum representation

$$\langle \vec{R}\,|(E - T_{\mathrm{N}} - V_0 + i\varepsilon)^{-1}|\vec{R}\,'\rangle = \sum_{JM} Y_{JM}(\hat{R}) \tfrac{1}{R} G_{0J}(E, R, R') \tfrac{1}{R'} Y^*_{JM}(\hat{R}'). \tag{2.47}$$

Employing this formula and the expansion (2.46) in the definition (2.32) yields

$$\int \mathrm{d}\hat{R}\mathrm{d}\hat{R}' Y^*_{JM}(\hat{R}) F(E,\vec{R},\vec{R}\,') Y^*_{J'M'}(\hat{R}') = \int \mathrm{d}\epsilon \mathrm{d}\hat{\epsilon} \mathrm{d}\hat{R}\mathrm{d}\hat{R}' \sum_{l_1 m_1} \sum_{J_0 M_0} \sum_{l_2 m_2}$$
$$Y^*_{JM}(\hat{R}) \sqrt{\frac{4\pi}{2l_1+1}} Y_{l_1 m_1}(\hat{R}) Y^*_{l_1 m_1}(\hat{\epsilon}) V_{\mathrm{d}\epsilon l_1}(R) \times$$
$$\times Y_{J_0 M_0}(\hat{R}) \tfrac{1}{R} G_{0J_0}(E,R,R') \tfrac{1}{R'} Y^*_{J_0 M_0}(\hat{R}') \times$$
$$\times \sqrt{\frac{4\pi}{2l_2+1}} V_{\mathrm{d}\epsilon l_2}(R') Y_{l_2 m_2}(\hat{\epsilon}) Y^*_{l_2 m_2}(\hat{R}') Y_{J'M'}(\hat{R}'). \qquad (2.48)$$

Since spherical harmonics are orthogonal we can perform integration over $\mathrm{d}\hat{\epsilon}$ and then employing the relations (A.3) and (A.4) for integrals of products of three harmonics the integrations over $\mathrm{d}\hat{R}$ and $\mathrm{d}\hat{R}'$ can be performed as well. Finally, using orthogonality of Wigner 3j symbols (A.5) we obtain

$$\int \mathrm{d}\hat{R}\mathrm{d}\hat{R}' Y^*_{JM}(\hat{R}) F(E,\vec{R},\vec{R}\,') Y^*_{J'M'}(\hat{R}') = \tfrac{1}{RR'} \delta_{JJ'} \delta_{MM'} f_J(E,R,R'), \qquad (2.49)$$

where

$$f_J(E,R,R') = \sum_{lJ'} (2J'+1) \begin{pmatrix} l & J' & J \\ 0 & 0 & 0 \end{pmatrix}^2 \int \mathrm{d}\epsilon V_{\mathrm{d}\epsilon l}(R) G_{0J'}(E-\epsilon,R,R') V^*_{\mathrm{d}\epsilon l}(R') \qquad (2.50)$$

or

$$F(E,\vec{R},\vec{R}'\,) = \sum_{JM} Y_{JM}(\hat{R}) \tfrac{1}{R} f_J(E,R,R') \tfrac{1}{R'} Y^*_{JM}(\hat{R}'). \qquad (2.51)$$

This form of expansion of nonlocal operator F is a consequence of its spherical symmetry. It is an important property since equations for partial waves with different J are not coupled through nonlocal potential although they are coupled with several partial waves of molecular channel (sum over J' in (2.50)) accounting thus for angular momentum of the electron released in the detachment or captured in the attachment process.

If we define partial waves ψ_J and φ_J with

$$\langle \vec{R}\,|\vec{E}^{\,(+)}\rangle = N \sum_{JM} i^J \tfrac{1}{KR} \varphi^I_J(R) Y^*_{JM}(\hat{E}) Y_{JM}(\hat{R}) \qquad (2.52)$$
$$\langle \vec{R}\,|\psi^{(+)}_I\rangle = N \sum_{JM} i^J \tfrac{1}{KR} \psi^I_J(R) Y^*_{JM}(\hat{E}) Y_{JM}(\hat{R}) \qquad (2.53)$$

and expand the Green function

$$\langle \vec{R}\,|G^{(+)}_Q(E)|\vec{R}\,'\rangle = \sum_{JM} Y_{JM}(\hat{R}) \tfrac{1}{R} G_{QJ}(E,R,R') \tfrac{1}{R'} Y^*_{JM}(\vec{R}\,') \qquad (2.54)$$

the Lippmann-Schwinger equation (2.36) yields

$$\psi^I_J(R) = \varphi^I_J(R) + \int \mathrm{d}R'\mathrm{d}R'' G_{QJ}(E,R,R') f_J(E,R',R'') \psi^I_J(R''). \qquad (2.55)$$

We introduced the wave number $K = \sqrt{2\mu E}$ in the equations (2.52), (2.53) and the normalization coefficient $N = 4\pi\sqrt{\mu K}(2\pi)^{-3/2}$ ensures the energy normalization

$$\langle \vec{E}^{\,(+)}|\vec{E}^{\,\prime(+)}\rangle = \delta(\vec{E} - \vec{E}\,'). \qquad (2.56)$$

Employing the partial wave expansions in the formula (2.38) for the associative detachment T-matrix and writing the wave functions $|\nu\rangle$ for bound states of AB in the usual separated form

$$\langle \vec{R}\,|\nu\rangle = \tfrac{1}{R}\chi_{n_\mathrm{f}J_\mathrm{f}}(R)Y_{J_\mathrm{f}M_\mathrm{f}}(\hat{R}) \tag{2.57}$$

we obtain

$$\begin{aligned}
T_\mathrm{AD}(\vec{\epsilon}_\mathrm{f},\vec{E}\,) &= \langle \nu_\mathrm{f}|V^*_{\mathrm{d}\vec{\epsilon}_\mathrm{f}}|\psi_I^{(+)}\rangle = \\
&= \int R^2\mathrm{d}R\mathrm{d}\hat{R}\sum_{lm}\sum_{JM}\tfrac{1}{R}\chi_{n_\mathrm{f}J_\mathrm{f}}(R)Y^*_{J_\mathrm{f}M_\mathrm{f}}(\hat{R})\times \\
&\qquad\times\sqrt{\frac{4\pi}{2l+1}}Y^*_{lm}(\hat{R})Y_{lm}(\hat{\epsilon})V^*_{\mathrm{d}\epsilon_\mathrm{f}l}(R)\times \\
&\qquad\times\, N i^J\tfrac{1}{KR}\psi^I_J(R)Y^*_{JM}(\hat{E})Y_{JM}(\hat{R}) = \\
&= \tfrac{N}{K}\sum_{lmJM} t^\mathrm{AD}_{Jl}(\nu_\mathrm{f},J_\mathrm{f},E)Y_{lm}(\hat{\epsilon})Y^*_{JM}(\hat{E})\times \\
&\qquad\times\, i^J\sqrt{(2J_\mathrm{f}+1)(2J+1)}\begin{pmatrix} J_\mathrm{f} & l & J \\ M_\mathrm{f} & m & M\end{pmatrix}\begin{pmatrix} J_\mathrm{f} & l & J \\ 0 & 0 & 0\end{pmatrix},
\end{aligned} \tag{2.58}$$

where

$$t^\mathrm{AD}_{Jl}(\nu_\mathrm{f},J_\mathrm{f},E) = \int \mathrm{d}R\chi_{n_\mathrm{f}J_\mathrm{f}}(R)V^*_{\mathrm{d}\epsilon_\mathrm{f}l}(R)\psi^I_J(R). \tag{2.59}$$

The integration formula (A.4) has been used again. The differential cross section for the associative detachment reads

$$\frac{\mathrm{d}\sigma_\mathrm{AD}}{\mathrm{d}\Omega}(\vec{\epsilon}_\mathrm{f},\vec{E}\,) = (2\pi)^4\tfrac{g_\mathrm{i}}{K^2}|T_\mathrm{AD}(\vec{\epsilon}_\mathrm{f},\vec{E}\,)|, \tag{2.60}$$

where g_i is the statistical factor for the discrete state potential. This factor applies only in the case that more potentials are connected to the same asymptote. The number g_i then gives the statistical probability for particles to move along the potential curve V_d. This is for example the case of H+H$^-$ (see Chapter 4). The formula (2.60) can further be simplified using the orthogonality relations (A.5) if we want to know only the integral cross section (integrated over $\hat{\epsilon}_\mathrm{f}$ and averaged over $\hat{E}$)

$$\sigma_{AD}(\epsilon_\mathrm{f},E) = \frac{2\pi g_\mathrm{i}}{KE}\sum_{lJ}(2J+1)\begin{pmatrix} J_\mathrm{f} & l & J \\ 0 & 0 & 0\end{pmatrix}^2 |t^\mathrm{AD}_{Jl}(\nu_\mathrm{f},J_\mathrm{f},E)|^2. \tag{2.61}$$

The total AD cross section is obtained via summation over all accessible final states ($E_{\nu_\mathrm{f}J_\mathrm{f}} < E$) or using the formula

$$\sigma_\mathrm{tot}(E) = \frac{2\mu g_\mathrm{i}}{KE}\sum_J(2J+1)\int\mathrm{d}R\mathrm{d}R'\,\psi^I_J(R)^*[f_J(E,R,R') - f^*_J(E,R',R)]\psi^I_J(R') \tag{2.62}$$

which can be derived from the total flux lost from the discrete state channel due to non-hermitian part of nonlocal potential F. Comparison of the two expressions for σ_tot was used as test for numerical solution of the resonant scattering problem by Bieniek [5] and proved failure of local complex approximation for associative detachment in H^-+H collisions. It is possible to show using expansion of $G_{0J}(E)$ in the sum over bound states $\chi_{nJ}(R)$ in the definition (2.50) that the two expressions for $\sigma_{\rm tot}$ are equivalent if no further approximation in imposed on $F(E)$.

The T-matrix and the cross section for dissociative attachment can be obtained from the principle of detailed balance since the processes AD and DA are mutually reverse. It is

$$T_{DA}(\hat{E},\hat{\epsilon}) = T^*_{AD}(\hat{\epsilon},\hat{E}) \tag{2.63}$$

and the integral cross section is

$$\sigma_{\rm DA}(E,\epsilon_{\rm i}) = (2\pi)^4 \tfrac{g_{\rm i}}{2\epsilon_{\rm i}} |T_{\rm DA}(\hat{E},\hat{\epsilon}_{\rm i})|^2. \tag{2.64}$$

Let us now investigate the vibrational excitation process. Employing the relation

$$G^{(+)}(E) = G^{(+)}_Q(E) + G^{(+)}_Q(E)F(E)G^{(+)}(E) \tag{2.65}$$

for the complete Green function $G^{(+)}(E) \equiv (E - H_{\rm eff} + i\varepsilon)^{-1}$ the equation (2.37) yields

$$|\psi^{(+)}_{II}\rangle = G^{(+)}(E) V_{{\rm d}\vec{\epsilon}_{\rm i}} |\nu_{\rm i}\rangle \tag{2.66}$$

and (2.39) implies

$$T_{\rm VE} = \langle \nu_{\rm f} | V^*_{{\rm d}\vec{\epsilon}_{\rm f}} G^{(+)}(E) V_{{\rm d}\vec{\epsilon}_{\rm i}} |\nu_{\rm i}\rangle. \tag{2.67}$$

Since F is spherically symmetric it is

$$\langle \vec{R}|G^{(+)}(E)|\vec{R}'\rangle = \sum_{JM} Y_{JM}(\hat{R})\tfrac{1}{R} G_J(E,R,R')\tfrac{1}{R'} Y^*_{JM}(\vec{R}') \tag{2.68}$$

We can thus use a similar procedure as for $T_{\rm AD}$ to obtain

$$\begin{aligned} T_{\rm VE} = & \sum_{l_1 m_1}\sum_{l_2 m_2}\sum_{JM} \int {\rm d}\, R {\rm d}R' \chi_{n_{\rm f}J_{\rm f}}(R) V^*_{{\rm d}\epsilon_{\rm f} l_1}(R) G_J(E,R,R') V_{{\rm d}\epsilon_{\rm i} l_2}(R') \chi_{n_{\rm i}J_{\rm i}}(R') \\ & \times (-1)^{M_{\rm f}+m_1+M} Y^*_{l_1 m_1}(\hat{\epsilon}_{\rm f}) Y_{l_2 m_2}(\hat{\epsilon}_{\rm i}) (2J+1)\sqrt{(2J_{\rm f}+1)(2J_{\rm i}+1)} \times \\ & \times \begin{pmatrix} J_{\rm f} & l_1 & J \\ 0 & 0 & 0 \end{pmatrix} \begin{pmatrix} J_{\rm f} & l_1 & J \\ -M_{\rm f} & -m_1 & M \end{pmatrix} \begin{pmatrix} J & l_2 & J_{\rm i} \\ -M & m_2 & M_{\rm i} \end{pmatrix} \begin{pmatrix} J & l_2 & J_{\rm i} \\ 0 & 0 & 0 \end{pmatrix}. \end{aligned} \tag{2.69}$$

The formula for the vibrational excitation process is more complicated than (2.58) for associative detachment since the angular momentum is transferred twice between the electron and the molecule—once during the resonant capture of electron into discrete state and for the second time in the autoionization. Even if we start with the molecule AB in a state $\nu_{\rm i}$ with defined angular momentum several partial waves are populated in $|\psi^{(+)}_{II}\rangle$ if $\Gamma_l \neq 0$ for $l > 0$. The state $|\psi^{(+)}_{II}\rangle$ can subsequently decay in many states $\nu_{\rm f}$ (with many different $J_{\rm f}$). Before going further we introduce one frequently used approximation.

2.4 Neglection of electron angular momentum

Since electron is a light particle it feels strongly the repulsive barrier $\frac{l(l+1)}{2r^2}$ ($m_e = 1$ in atomic units). For large r we can neglect the other forces and assume the potential is spherically symmetric[4], i. e. expansion (2.43) reduces to

$$|\phi_\epsilon^{(+)}) = \sum_{lm} \phi_{lm}(\epsilon, r) Y_{lm}(\hat{r}) Y^*_{lm}(\hat{\epsilon}). \tag{2.70}$$

If the electron energy ϵ is small (near threshold energies) it is reasonable to assume, that the electron can not penetrate the repulsive barrier and $\phi_{lm}(\epsilon, r) = 0$ for r small and $l > 0$, i. e.

$$V_{\mathrm{d}\epsilon l} = 0 \qquad \text{for } l > 0 \tag{2.71}$$

and

$$V_{\mathrm{d}\vec{\epsilon}} = \sqrt{4\pi} Y_{00}(\hat{R}) Y_{00}(\hat{\epsilon}) V_{\mathrm{d}\epsilon}(R), \tag{2.72}$$

where with $V_{\mathrm{d}\epsilon}(R)$ we denoted $V_{\mathrm{d}\epsilon l=0}(R)$. As a consequence the sums over l can be dropped out in all previous formulas for near threshold processes, which simplifies the problem significantly. Thus using eq. (A.6) the formula (2.50) yields

$$f_J(E, R, R') = \int \mathrm{d}\epsilon V_{\mathrm{d}\epsilon}(R) G_{0J}(E - \epsilon, R, R') V^*_{\mathrm{d}\epsilon}(R'). \tag{2.73}$$

Similarly employing (A.6) and (A.7) the associative detachment T-matrix is found to be

$$T_{\mathrm{AD}}(\vec{\epsilon}_{\mathrm{f}}, \vec{E}\,) = \frac{N}{K} \frac{i^{J_{\mathrm{f}}}}{\sqrt{4\pi}} Y^*_{J_{\mathrm{f}} M_{\mathrm{f}}}(\hat{E}) \int \mathrm{d}R \chi_{n_{\mathrm{f}} J_{\mathrm{f}}}(R) V^*_{\mathrm{d}\epsilon_{\mathrm{f}}}(R) \psi^I_{J_{\mathrm{f}}}(R) \tag{2.74}$$

and the cross section

$$\sigma_{\mathrm{AD}}(\epsilon_{\mathrm{f}}, E) = \frac{2\pi g_{\mathrm{i}}}{KE} \left| \int \mathrm{d}R \chi_{n_{\mathrm{f}} J_{\mathrm{f}}}(R) V^*_{\mathrm{d}\epsilon_{\mathrm{f}}}(R) \psi^I_{J_{\mathrm{f}}}(R) \right|^2. \tag{2.75}$$

The description of vibrational excitation also considerably simplifies if we neglect the angular momentum of electron. The T_{VE} thus reduces to

$$T_{\mathrm{VE}}(\vec{\epsilon}_{\mathrm{f}}, \vec{\epsilon}_{\mathrm{i}}) = \tfrac{1}{4\pi} \delta_{J_{\mathrm{f}} J_{\mathrm{i}}} \delta_{M_{\mathrm{f}} M_{\mathrm{i}}} t^{\mathrm{VE}}_J(n_{\mathrm{f}}, \epsilon_{\mathrm{f}}, n_{\mathrm{i}}, \epsilon_{\mathrm{i}}), \tag{2.76}$$

where

$$t^{\mathrm{VE}}_J(n_{\mathrm{f}}, \epsilon_{\mathrm{f}}, n_{\mathrm{i}}, \epsilon_{\mathrm{i}}) = \int \mathrm{d}R \mathrm{d}R' \chi_{n_{\mathrm{f}} J_{\mathrm{f}}}(R) V^*_{\mathrm{d}\epsilon_{\mathrm{f}}}(R) G_{J_{\mathrm{f}}}(E, R, R') V_{\mathrm{d}\epsilon_{\mathrm{i}}}(R') \chi_{n_{\mathrm{i}} J_{\mathrm{i}}}(R'). \tag{2.77}$$

The presence of Kronecker delta $\delta_{J_{\mathrm{f}} J_{\mathrm{i}}}$ and $\delta_{M_{\mathrm{f}} M_{\mathrm{i}}}$ is the consequence of angular momentum conservation for the molecule AB, when angular momentum of electron has been neglected. We thus do not have the possibility to describe rotational

[4] This is not true in the case the molecule AB posses an electric dipole. Influence of the approximation (2.71) to the cross sections then needs further investigation.

excitation unless the assumption (2.71) is rejected. The formula for partial contribution to T_{VE} can easily be transformed into the form

$$t_J^{\mathrm{VE}}(n_{\mathrm{f}}, \epsilon_{\mathrm{f}}, n_{\mathrm{i}}, \epsilon_{\mathrm{i}}) = \int \mathrm{d}R \chi_{n_{\mathrm{f}}J}(R) V^*_{\mathrm{d}\epsilon_{\mathrm{f}}}(R) \psi_J^{II}(R), \tag{2.78}$$

where $\psi_J^{II}(R)$ is the unique solution of

$$\psi_J^{II}(R) = \varphi_J^{II}(R) + \int \mathrm{d}R' \mathrm{d}R'' G_{QJ}(E, R, R') f_J(E, R', R'') \psi_J^{II}(R'') \tag{2.79}$$

and we have introduced abbreviation

$$\varphi_J^{II}(R) = \int \mathrm{d}R' G_{QJ}(E, R, R') V_{\mathrm{d}\epsilon_{\mathrm{i}}}(R') \chi_{n_{\mathrm{i}}J}(R'). \tag{2.80}$$

The equation (2.79) is the partial wave expansion of eq. (2.37) under the assumption (2.71). Finally angle integrated VE cross section reads

$$\sigma_{\mathrm{VE}}(n_{\mathrm{f}}, \epsilon_{\mathrm{f}}, n_{\mathrm{i}}, \epsilon_{\mathrm{i}}) = \frac{(2\pi)^3}{4\epsilon_{\mathrm{i}}} |t_J^{\mathrm{VE}}(n_{\mathrm{f}}, \epsilon_{\mathrm{f}}, n_{\mathrm{i}}, \epsilon_{\mathrm{i}})|^2, \tag{2.81}$$

with J being the angular momentum of initial state $|\nu_{\mathrm{i}}\rangle$.

2.5 Nonlocal resonance model

It is clear on the basis of the previous discussion of the theory of resonant collisions that the resonant dynamics and the cross sections are fully determined if the functions

$$V_0(R),\ V_{\mathrm{d}}(R) \text{ and } V_{\mathrm{d}\epsilon l}(R)$$

are known. As was shown in the last section $V_{\mathrm{d}\epsilon l}(R)$ with $l > 0$ do not contribute significantly for small energies ϵ and only the function $V_{\mathrm{d}\epsilon}(R)$ is important for the dynamics. Further simplification can be achieved thanks to the extraction of all fast dependencies on ϵ and R from the background scattering due to the extraction of resonance part of the wave function. It follows that the discrete-continuum coupling $V_{\mathrm{d}\epsilon}(R)$ is slowly varying function of ϵ and R. The coupling $V_{\mathrm{d}\epsilon}(R)$ is a complex quantity, but the overall phase is not important, since $V_{\mathrm{d}\epsilon}(R)$ is present together with $V^*_{\mathrm{d}\epsilon}(R')$ in nonlocal potential and only absolute value of its matrix elements is needed for cross sections. What is important is the relative phase between $V_{\mathrm{d}\epsilon}(R)$ and $V_{\mathrm{d}\epsilon}(R')$ in two different points R and R' but since the nonlocal resonant dynamics is restricted to a small region near equilibrium distance R_0 of the molecule AB and since the coupling is slowly varying with R it is reasonable to assume that this relative phase can be neglected and $V_{\mathrm{d}\epsilon}(R)$ can be regarded as being real number. This assumption is unnecessary simplification if the quantities $V_{\mathrm{d}\epsilon}(R)$ are constructed directly from electron-molecule scattering calculation, but it is very helpful, when $V_{\mathrm{d}\epsilon}(R)$ is constructed from incomplete information about the electron dynamics.

Expansion of the discrete-continuum coupling into sum of separable terms in energy ϵ and inter-nuclear distance R is often performed

$$V_{\mathrm{d}\epsilon}(R) = \sum_i f_i(\epsilon) g_i(R). \tag{2.82}$$

As will be discussed later the separation of energy and distance is crucial for time demands of actual numerical calculation. It has been shown that even one term in the expansion often gives qualitatively correct results for the description of the resonant dynamics.

The nonlocal resonant dynamics described by the four functions $V_0(R)$, $V_d(R)$, $f_i(\epsilon)$ and $g_i(R)$ will be further referred to as the nonlocal resonance model of the dynamics in this work. The calculation of the function $V_0(R)$ for the particular molecule AB is a routine task of quantum chemistry and a large variety of the methods have been developed in the last few decades to treat this problem. The direct determination of $V_{\rm d}(R)$ and $V_{{\rm d}\epsilon}(R)$ is still far from routine. The calculations for range of both ϵ and R are available only for the most fundamental systems like H_2+e^- [16] and HeH+e^- [22]. It is necessary to use as much a-priory information about behavior of the model functions as possible in attempts to construct the models from incomplete information.

The threshold behavior of the discrete-continuum coupling $V_{{\rm d}\epsilon l}(R)$ for the small energies ϵ is determined by the long range electron-molecule forces in accordance with the threshold law of Wigner [23]. If the molecule AB does not posses an electric dipole, the long range electron-molecule interaction vanishes faster then r^{-2} and the threshold behavior of the coupling is [4]

$$\Gamma_l(\epsilon) \equiv 2\pi |V_{{\rm d}\epsilon l}(R)|^2 \sim \epsilon^{(2l+1)/2}. \tag{2.83}$$

As discussed before only the lowest l allowed by symmetry is really important, which usually is $l = 0$. In the case of polar molecules the threshold behavior depends on the dipole moment D of the molecule. For $D < D_{\rm crit} = 1.625$ it is [4]

$$\Gamma(\epsilon) \sim E^\alpha \tag{2.84}$$

where

$$\alpha = \sqrt{d + \frac{1}{4}} \tag{2.85}$$

and d is a dimension-less reduced dipole moment given by the lowest eigenvalue of an infinite-dimensional tridiagonal matrix [24]. If the molecule possesses a supercritical dipole $D > D_{\rm crit}$ bound states exist in electron-molecule channel and the threshold behavior is more complicated. Similar situation is faced in the case of Penning ionization or dissociative recombination, where the electron is subjected to Coulomb force in the $e^- + AB^+$ channel. Nonlocal dynamics for these cases will not be investigated in this work.

The threshold law (2.83) or (2.84) fixes the form of $f_i(\epsilon)$ near the origin $\epsilon = 0$ and both $f_i(\epsilon)$ and $g_i(R)$ must vanish at infinity. The value of $V_{\rm d}(R)$ at infinity is fixed since $E_{\rm d} = V_{\rm d} - V_0$ evaluated in $R = \infty$ equals to the electron affinity at the atom A (or B).

Methods for construction of $V_{\rm d}(R)$, $V_{{\rm d}\epsilon}$ from *ab initio* fixed-R electron-molecule scattering data and other *ab initio* information will be given in the following chapters.

Chapter 3

Computational procedures

The problem of resonant electron-molecule or ion-atom scattering has been transformed into solution of the one-dimensional Lippmann-Schwinger equation in the previous chapter. The equation contains a rather complicated quantity—the non-local potential, resulting from a coupling of the discrete resonant state with continuum, which has to be calculated first. As soon as the solution of the equation is known the cross sections are easily found evaluating the matrix elements of discrete-state to continuum coupling $V_{\mathrm{d}\vec{\epsilon}}$. General scheme for the solution of the problem can be summarized as follows:

1. To find the scattering solution $\varphi_J^I(R)$ and the Green function $G_{QJ}(E)$ for the local potential V_d.

2. To calculate the nonlocal potential $f_J(E)$. As shown later this is closely related to calculation of bound states $|\nu\rangle$ in the potential V_0.

3. To solve the Lippmann-Schwinger equation for the wave functions $\psi_J^I(R)$ or $\psi_J^{II}(R)$ respectively.

4. To calculate the T-matrix elements and cross-sections (or other quantities of interest) from $\psi_J(R)$.

The step 4 is trivial application of the formulas derived above. Computational procedures to perform the other three steps are outlined below. The methods proposed are tested for efficiency on the example of dissociative attachment of an electron to H_2 molecule.

3.1 Solution of the local problem

There have been developed large variety of methods to solve the Lippmann-Schwinger equation for local potential in the past few decades and it is nowadays a routine task. First of all the Lippmann-Schwinger equation

$$\varphi_J(R) = u_J(R) - \frac{2\mu}{K}\int \mathrm{d}R u_J(R_<)v_J(R_>)V_\mathrm{d}(R')\varphi_J(R'), \tag{3.1}$$

where $R_> = \max(R, R')$, $R_< = \min(R, R')$) and the functions u_J and v_J are given in terms of spherical Bessel functions j_J and h_J

$$\begin{aligned} u_j(R) &= KRj_J(KR), & (3.2)\\ v_j(R) &= iKRh_J(KR) & (3.3)\end{aligned}$$

is equivalent to the Schrödinger equation

$$\left(-\frac{1}{2\mu}\frac{\mathrm{d}^2}{\mathrm{d}R^2} + \frac{J(J+1)}{2\mu R^2} + V_\mathrm{d}(R)\right)\varphi_J(R) = E\varphi_J(R). \tag{3.4}$$

Standard finite difference methods like algorithms of Numerov or Runge-Kuta can be used to solve this equation. Special methods for the case when $\varphi_J(R)$ is fast oscillating function have also been developed [25, 26]. We preferred to solve the integral equation (3.1) directly in this work. The solution of (3.1) gives the correct normalization automatically, whereas the normalization has to be find afterwards when solving the differential Schrödinger equation. As we will see later solving the Lippmann-Schwinger equation we obtain also the T-matrix for the local problem as a byproduct. Other advantage of the integral equation formulation is the possibility of increasing the numerical precision by means of Romberg quadrature [27]. Long range rotational energy term $J(J+1)/2\mu R^2$ is treated exactly in the Lippmann-Schwinger equation method. The prize for this is the occurrence of the Bessel functions in the equation, which must be calculated in many points. Nevertheless this does not slow the calculation considerably if the solution is required for a large number of J since very efficient method for calculation of large number of Bessel functions by means of stable recurrence relations has been developed [28].

The method we used for solving the equation (3.1) is described in detail in the article of Horáček [27]. Here we only outline the principles and generalize the method for finding the irregular solution and the Green function.

Regular solution

We will omit the subscripts J and d in this section. The equation (3.1) can easily be rewritten in the form

$$\varphi(R) = Au(R) - \frac{2\mu}{K}\int_0^R \mathrm{d}R'[v(R)u(R') - u(R)v(R')]V(R')\varphi(R'), \tag{3.5}$$

where

$$A = 1 - \frac{2\mu}{K}\int_0^\infty v(R')V(R')\varphi(R')dR'. \tag{3.6}$$

In other words, if we introduce the function $f(R) = \varphi(R)/A$ it is

$$f(R) = [1 - \beta(R)]u(R) + \alpha(R)v(R), \tag{3.7}$$

where

$$\alpha(R) = -\frac{2\mu}{K}\int_0^R \mathrm{d}R' u(R')V(R')f(R'), \tag{3.8}$$
$$\beta(R) = -\frac{2\mu}{K}\int_0^R \mathrm{d}R' v(R')V(R')f(R'). \tag{3.9}$$

The constant A can be found from

$$A = (1 - \beta(\infty))^{-1} \tag{3.10}$$

and the T-matrix for elastic scattering is given by formula

$$t \equiv -\frac{2\mu}{K}\int_0^\infty \mathrm{d}R u(R)V(R)\varphi(R) = \alpha(\infty)[1 - \beta(\infty)]^{-1}. \tag{3.11}$$

Numerical solution of the integral equation (3.1) on a grid $R = x_1, \ldots, x_n$ is based on equation (3.7). The trapezoidal rule is used for the integrals (3.8) and (3.9). Observe that the terms with $f(R' = R)$ vanish in the formula (3.7) and it can be used to calculate $f(x_{i+1})$ if $f(x_1), \ldots, f(x_i)$ are known.

Irregular solution and Green function

The regular solution of the Schrödinger equation (3.4) is the solution obeying the boundary condition $\varphi_{(\mathrm{r})}(R = 0) = 0$. Since $u(R = 0) = 0$ we can see from (3.5) that the solution of (3.1) is indeed the regular solution. The irregular solution on the other hand is the solution obeying the condition $\varphi_{(\mathrm{i})}(R \to \infty) \sim v(R)$. The Green function $G_{QJ}(E, R, R')$ can be written in terms of these two solutions

$$\begin{aligned} G_{QJ}(E,R,R') &\equiv \langle R|\left(E + \frac{1}{2\mu}\frac{\mathrm{d}^2}{\mathrm{d}R^2} - \frac{J(J+1)}{2\mu R^2} - V_{\mathrm{d}}(R) + i\varepsilon\right)^{-1}|R'\rangle = \\ &= -\frac{2\mu}{K}\varphi_{(\mathrm{r})}(R_<)\varphi_{(\mathrm{i})}(R_>). \end{aligned} \tag{3.12}$$

It is easy to show that $\varphi_{(\mathrm{i})}(R)$ is the solution of

$$\varphi_{(\mathrm{i})}(R) = v(R) - \frac{2\mu}{K}\int_0^\infty \mathrm{d}R u(R_<)v(R_>)V_{\mathrm{d}}(R')\varphi_{(\mathrm{i})}(R'), \tag{3.13}$$

which can be rearranged into the form

$$\varphi(R) = Av(R) - \frac{2\mu}{K}\int_R^\infty \mathrm{d}R'[v(R')u(R) - u(R')v(R)]V(R')\varphi(R'), \tag{3.14}$$

analogous to (3.5) and it yields for $f(R) = \varphi(R)/A$

$$f(R) = [1 - \alpha(R)]v(R) + \beta(R)u(R) \tag{3.15}$$

with

$$\alpha(R) = -\frac{2\mu}{K}\int_R^\infty \mathrm{d}R' u(R')V(R')f(R'), \quad (3.16)$$

$$\beta(R) = -\frac{2\mu}{K}\int_R^\infty \mathrm{d}R' v(R')V(R')f(R'). \quad (3.17)$$

The constant A can be written in terms of α

$$A = 1 - \frac{2\mu}{K}\int_0^\infty \mathrm{d}R u(R)V(R)\varphi(R) = 1 + A\alpha(0), \quad (3.18)$$

i. e. $A = (1-\alpha(\infty))^{-1}$. Equation (3.15) can be used for numerical calculation of $f(R)$ on a grid in the same way as equation (3.7) in the case of regular solution. The only difference is that now the function $f(R)$ has to be calculated in decreasing sequence of grid points starting from sufficiently large x_n, so that $f(x_n) = v(x_n)$ can be assumed. Irregular solution $\varphi_{\mathrm{i}}(R)$ is then obtained by multiplication of $f(R)$ with A.

The procedure for the calculation of regular and irregular solutions and the Green function outlined above can be generalized for the coupled channel problem. The generalization is presented in the appendix C together with hints for the solution of additional numerical problems occurring in that case.

3.2 Evaluation of the nonlocal potential

The key element of evaluation of the nonlocal potential

$$F(E) = \int \mathrm{d}\epsilon \mathrm{d}\hat{\epsilon} V_{\mathrm{d}\vec{\epsilon}} G_0(E-\epsilon) V^*_{\mathrm{d}\vec{\epsilon}}$$

is the knowledge of the Green function $G_0(E) \equiv (E - T_N - V_0 + i\varepsilon)^{-1}$ for the neutral molecule AB. The formula similar to (3.12) is of little use here, because the regular and irregular solutions depend on energy and the integration over ϵ can not easily be performed. It is better idea to expand the $G_0(E)$ in terms of bound states of molecule AB

$$\langle \vec{R}\,|\nu\rangle = \frac{1}{R}\chi_{nJ}(R)Y_{JM}(\hat{R}) \quad (3.19)$$

to obtain

$$\begin{aligned} G_0(E,\vec{R},\vec{R}') &= \sum\!\!\!\!\!\!\int_\nu \frac{\langle \vec{R}\,|\nu\rangle\langle\nu|\vec{R}\,'\rangle}{E - E_\nu + i\varepsilon} = \\ &= \sum_{JM} Y_{JM}(\hat{R})\frac{1}{R}\sum\!\!\!\!\!\!\int_n \frac{\chi_{nJ}(R)\chi_{nJ}(R')}{E - E_n^J + i\varepsilon}\frac{1}{R'}Y_{JM}(\hat{R}'). \end{aligned} \quad (3.20)$$

Comparison of this expansion with (2.47) yields

$$G_{0J}(E,R,R') \equiv \left(E + \frac{1}{2\mu}\frac{\mathrm{d}^2}{\mathrm{d}R^2} - \frac{J(J+1)}{2\mu R^2} - V_0(R) + i\varepsilon\right)^{-1} = \sum\!\!\!\!\!\!\int_n \frac{\chi_{nJ}(R)\chi_{nJ}(R')}{E - E_n^J + i\varepsilon}. \quad (3.21)$$

This expression is convenient for evaluation of $F(E)$ since the integration over $\mathrm{d}\epsilon$ can be performed analytically (see (2.34) and (2.35))

$$F(E,\vec{R},\vec{R}\,') = \sum_n\!\!\!\!\!\!\int \langle\vec{R}|\nu\rangle[\Delta(E-E_\nu,\vec{R},\vec{R}\,') - \frac{i}{2}\Gamma(E-E_\nu,\vec{R},\vec{R}\,')]\langle\nu|\vec{R}\,'\rangle \quad (3.22)$$

or after partial wave expansion (see the formula (2.50))

$$\begin{aligned} f_J(E,R,R') = \sum_{lJ'}(2J'+1)\begin{pmatrix} l & J' & J \\ 0 & 0 & 0 \end{pmatrix}^2 \times \\ \times\sum_n\!\!\!\!\!\!\int \chi_{nJ'}(R)[\Delta_l(E-E_n^{J'},R,R') - \frac{i}{2}\Gamma_l(E-E_n^{J'},R,R')]\chi_{nJ'}(R') \end{aligned} \quad (3.23)$$

where

$$\Gamma_l(\epsilon,R,R') = 2\pi V_{\mathrm{d}\epsilon l}(R)V^*_{\mathrm{d}\epsilon l}(R'), \quad (3.24)$$

$$\Delta_l(\epsilon,R,R') = \frac{1}{2\pi}\wp\int \mathrm{d}\epsilon'\Gamma_l(\epsilon',R,R')/(\epsilon-\epsilon'). \quad (3.25)$$

If we neglect the angular momentum of the released/captured electron (see the section 2.4) we get

$$f_J(E,R,R') = \sum_n\!\!\!\!\!\!\int \chi_{nJ}(R)[\Delta_0(E-E_n^J,R,R') - \frac{i}{2}\Gamma_0(E-E_n^J,R,R')]\chi_{nJ}(R') \quad (3.26)$$

Minor difficulty for application of this expansion to actual numerical calculation is the presence of continuum functions in the sum over n, which becomes important near dissociation limit for the neutral molecule AB. This problem has been overcome by appropriate discretization of continuum spectrum by Horáček et al [29]. We used Fourier DVR method for the discretization as suggested in [29], which is equivalent to putting the molecule AB into box, i. e. imposing the boundary condition $\chi_{nJ}(R_\mathrm{c}) = 0$ at certain cut-off radius R_c. The sum over n is then cut at certain $n = n_\mathrm{max}$.

Local approximations

A local approximation of the nonlocal dynamics is based on the replacement of the nonlocal potential $f_j(E,R,R')$ with certain local quantity. The possibility of such a replacement is based on different time-scales for electronic and nuclear dynamics. The nuclei are moving in the presence of electron captured in discrete resonant state $|\phi_\mathrm{d})$. The resonant state $|\phi_\mathrm{d})$ can decay at any point R and the electron can again be captured into $|\phi_\mathrm{d})$ at a different point R'. If the electron released in the decay is fast the difference between R and R' can not be large, because otherwise the electron would be gone before nuclei succeed to travel the distance $|R-R'|$ and could not be captured again. The non-locality of the interaction is therefore pronounced only if resonance energy $E_\mathrm{d} = V_\mathrm{d} - V_0$ is small, i. e. if potential curves $V_\mathrm{d}(R)$ and $V_0(R)$ come close together or even cross each other. If they are well separated (as is often the case for the Penning ionization) it is possible to replace $V_\mathrm{d} + f_j$ with [10, 4, 30]

$$V_\mathrm{loc}(R) - \tfrac{i}{2}\Gamma_\mathrm{loc}(R), \quad (3.27)$$

where

$$\begin{aligned} V_{\mathrm{loc}}(R) &= V_0(R) + E_{\mathrm{res}}(R), & (3.28)\\ \Gamma_{\mathrm{loc}}(R) &= \Gamma(E_{\mathrm{res}}(R), R, R), & (3.29)\end{aligned}$$

and

$$E_{\mathrm{res}}(R) = V_{\mathrm{d}}(R) - V_0(R) + \Delta_j(E_{\mathrm{res}}(R), R, R). \tag{3.30}$$

A transparent derivation of this approximation including the possibility of first order corrections[1] has been done in the time-dependent formalism [4]. It is also possible to show that if $E_{\mathrm{res}}(R) < 0$ then $V_{\mathrm{loc}}(R)$ is the bound state of H_{el} (see eq. (2.23)).

The local approximation (3.28) can not give good results for the systems where the curves $V_0(R)$ and $V_{\mathrm{d}}(R)$ come close together. Nevertheless local approximations are still useful to accelerate the convergence of iteration methods for solving nonlocal Lippmann-Schwinger equation

$$|\psi\rangle = |\varphi\rangle + G_{Qj} f_j |\varphi\rangle, \tag{3.31}$$

which corresponds to the partitioning of the potential $V_{\mathrm{eff}} = V_{\mathrm{d}} + f_j$ into V_{d} and f_j. We can use the different partitioning $V_{\mathrm{eff}} = V_{\mathrm{loc}} + f'_j$ instead, with $f'_j = f_j + V_{\mathrm{d}} - V_{\mathrm{loc}}$ being "smaller" operator than original f_j and having a chance for faster convergence of methods for solving the corresponding Lippmann-Schwinger equation (see the next section).

Use of the approximation (3.28) is limited also by the fact that the equation (3.30) often does not have a unique solution. Different local approximation has been proposed [29] to accelerate the convergence (in the way suggested above). This approximation is convenient in the cases where the wave function $\psi_J(R)$ is not strongly oscillating. The first term in the Taylor expansion

$$\int f_J(E, R, R')\psi_J(R')\mathrm{d}R' = \int f_J(E, R, R')[\psi_J(R) + (R' - R)\psi'_J(R) + \cdots]\mathrm{d}R' \tag{3.32}$$

yields the approximation

$$f_{\mathrm{loc}}(E, R) = \int f_J(E, R, R')\mathrm{d}R'. \tag{3.33}$$

3.3 Solution of Lippmann-Schwinger equation with nonlocal potential

A very efficient method for computing the T-matrix elements in the presence of nonlocal interactions, the Schwinger-Lanczos algorithm, was proposed recently [31]. This method has been successfully used in several realistic applications [32, 29, 33] to calculate cross sections for vibrational excitation, associative detachment and dissociative attachment based on the use of the nonlocal resonance

[1] In the time-dependent picture the effective potential (after projecting out the continuum) is not only nonlocal but contains also the memory effects. The first order corrections depend only on the first derivative of the wave function with respect to time and R.

model. Originally, the method was designed for calculation of the diagonal T-matrix elements. In principle, it can also be used for calculation of non-diagonal T-matrix elements resulting from multichannel collisions, but the calculation is rather cumbersome and the incoming and outgoing states are not treated symmetrically. It is the purpose of this section to present a generalization of the Schwinger-Lanczos algorithm for the multichannel case and to establish its relation to other methods.

As is well known the T-matrix can be represented in the form of the Born series, which however often converges very slowly or does not converge at al [14]. Several methods have been developed to sum such a divergent series. In this section one of these methods called the Wynn's epsilon algorithm is discussed and proved to be equivalent to our generalization of the Schwinger-Lanczos algorithm. This mathematical equivalence does not mean any equivalence of the numerical properties. To show this we compare the numerical performance of all three methods on example of the dissociative attachment of an electron to H_2 molecule in the section 3.4. The section contains also some general remarks about application of the methods to associative detachment and vibrational excitation. This system represents a typical example of a resonance process with the strong nonlocal part of the nuclear dynamics. The need of a very efficient procedure for the calculation of the T-matrix elements is vigorous in the case of the process of associative detachment, where many partial waves contribute to cross section (see following two chapters for associative detachment $H+H^-$ and $H+Cl^-$ calculations, with inclusion of nonlocal effects).

Short review of the Schwinger-Lanczos approach

According to the Schwinger variational principle [34] the T-matrix element

$$T_{\mathrm{fi}} \equiv \langle\phi_{\mathrm{f}}|T|\phi_{\mathrm{i}}\rangle = \langle\phi_{\mathrm{f}}|V(V - VG_0V)^{-1}V|\phi_{\mathrm{i}}\rangle \tag{3.34}$$

is given by the stationary value of the functional

$$T[\psi_-, \psi_+] = \langle\phi_{\mathrm{f}}|V|\psi_+\rangle + \langle\psi_-|V|\phi_{\mathrm{i}}\rangle - \langle\psi_-|V - VG_0V|\psi_+\rangle, \tag{3.35}$$

where V is an interaction potential and G_0 the free particle Greens function. This stationary value is achieved for $|\psi_\pm\rangle$ being solutions of the corresponding Lippmann-Schwinger equations. Considering $|\psi_\pm\rangle$ in the form

$$|\psi_\pm\rangle = \sum_{k=1}^{N} c_k^{(\pm)}|g_k\rangle, \tag{3.36}$$

with variational parameters $c_k^{(\pm)}$ we obtain an approximation to the T-matrix

$$T_{\mathrm{fi}}^N = \sum_{k,l=1}^{N} \langle\phi_{\mathrm{f}}|V|g_k\rangle(M^{-1})_{kl}\langle g_l|V|\phi_{\mathrm{i}}\rangle, \tag{3.37}$$

where the matrix M is given by $M_{kl} = \langle g_k|V - VG_0V|g_l\rangle$. The set of vectors $\{|g_k\rangle\}_{k=1}^N$ can be chosen arbitrarily (not necessarily orthogonal) provided that

M_{kl} is a regular matrix. The Schwinger-Lanczos method (SLM) was proposed for calculation of the diagonal T-matrix elements [31], i. e. $|\phi_{\rm f}\rangle = |\phi_{\rm i}\rangle = |\phi\rangle$, needed for evaluation of elastic cross sections. In this method $T^N_{\rm fi}$ is calculated according to (3.37), with $|g_1\rangle = |\phi\rangle\langle\phi|V|\phi\rangle^{-1/2}$ and the set $\{|g_k\rangle\}^N_{k=1}$ is taken as V-orthogonal

$$\langle g_k|V|g_l\rangle = \delta_{kl} \tag{3.38}$$

and such that matrix VG_0V is tridiagonal

$$\begin{aligned}
\langle g_{k-1}|VG_0V|g_k\rangle = \langle g_k|VG_0V|g_{k-1}\rangle &= \beta_{k-1}, && (3.39)\\
\langle g_k|VG_0V|g_k\rangle &= \alpha_k, && (3.40)\\
\langle g_k|VG_0V|g_l\rangle &= 0 \qquad \text{for} \quad |k-l| \geq 2. && (3.41)
\end{aligned}$$

Let us note that the complex-symmetric scalar product (i.e. without complex conjugation) is used throughout this section and not the usual (hermitian) one, since G_0 is a symmetric but non-hermitian operator. Only the matrix element $(M^{-1})_{11}$ is needed in (3.37) and this element is for a tridiagonal matrix M easily expressible in the form of a continued fraction. The T-matrix then reads

$$T^N = \langle\phi|V|g_1\rangle(M^{-1})_{11}\langle g_1|V|\phi\rangle = \frac{\langle\phi|V|\phi\rangle}{1-\alpha_1-}\frac{\beta_1^2}{1-\alpha_2-}\frac{\beta_2^2}{1-\alpha_3-}\cdots\frac{\beta_{N-1}^2}{1-\alpha_N}. \tag{3.42}$$

The numbers α_k, β_k and the vectors $|g_k\rangle$ with properties (3.38)-(3.41) are constructed according to the recurrence (see [31] and the refs. therein for more details about the Lanczos algorithm)

$$\begin{aligned}
|r_k\rangle &= G_0V|g_k\rangle - \beta_{k-1}|g_{k-1}\rangle, && (3.43)\\
\alpha_k &= \langle g_k|V|r_k\rangle, && (3.44)\\
|s_k\rangle &= |r_k\rangle - \alpha_k|g_k\rangle, && (3.45)\\
\beta_k &= \langle g_k|V|g_k\rangle^{1/2}, && (3.46)\\
|g_{k+1}\rangle &= \beta_k^{-1}|s_k\rangle, && (3.47)
\end{aligned}$$

with $|g_1\rangle = |\phi\rangle\langle\phi|V|\phi\rangle^{-1/2}$ and $\beta_0 = 0$.

The off-diagonal matrix elements of the $T-$matrix are needed for the calculation of resonant electron-molecule and ion-atom collisions. The same Lanczos basis with the properties (3.38)-(3.41) generated by the algorithm (3.43)-(3.47) and with the starting vector $|g_1\rangle = |\phi_{\rm i}\rangle\langle\phi_{\rm i}|V|\phi_{\rm i}\rangle^{-1/2}$ can be used in such a case. The formula for the T-matrix element resulting from (3.37) will be slightly more complicated than in the previous case

$$T^N_{\rm fi} = \sum_{k=1}^{N}\langle\phi_{\rm f}|V|g_k\rangle(M^{-1})_{k1}\langle g_1|V|\phi_{\rm i}\rangle. \tag{3.48}$$

Note that now the first column of M^{-1} is needed instead of the single element M^{-1}_{11}. Using elementary algebra it turns out that

$$(M^{-1})_{k1} = \frac{\beta_1}{f_1}\frac{\beta_2}{f_2}\cdots\frac{\beta_{k-1}}{f_{k-1}}\frac{1}{f_k}, \tag{3.49}$$

where the quantities

$$f_k = 1 - \alpha_k - \beta_k^2 / f_{k+1}, \qquad f_N = 1 - \alpha_N \tag{3.50}$$

are involved also in the calculation of the continued fraction (3.42). As pointed out in the reference [31] this approach does not treat in and out states in a symmetrical manner. For this reason the so called band Lanczos algorithm [35] was proposed [31] which leads to a banded instead of a tridiagonal matrix. Another approach preserving tridiagonality of the matrix, but using different basis sets for in- and outgoing states will be presented below. This approach represents a generalization of the SLM and we will refer to it as GSLM.

Generalization of SLM for off-diagonal T-matrix elements

A generalization of the SLM is obtained assuming the functions $|\psi_\pm\rangle$ in the Schwinger variational principle (3.35) to be of the form

$$|\psi_\pm\rangle = \sum_{k=1}^{N} c_k^{(\pm)} |g_k^{(\pm)}\rangle, \tag{3.51}$$

where we have introduced two different basis sets $\{|g_k^{(+)}\rangle\}_{k=1}^N$ and $\{|g_k^{(-)}\rangle\}_{k=1}^N$. The value of the functional (3.35) stationary with respect to variations of the coefficients $c_k^{(\pm)}$ is

$$T_{\mathrm{fi}}^N = \sum_{k,l=1}^{N} \langle \phi_{\mathrm{f}} | V | g_k^{(+)} \rangle (M^{-1})_{kl} \langle g_l^{(-)} | V | \phi_{\mathrm{i}} \rangle, \tag{3.52}$$

with

$$M_{kl} = \langle g_k^{(-)} | V - V G_0 V | g_l^{(+)} \rangle.$$

If we define $|g_k^{(\pm)}\rangle$ in such a way, that

$$\begin{aligned}
\langle g_k^{(-)} | V | g_l^{(+)} \rangle &= \delta_{kl}, && (3.53)\\
\langle g_{k-1}^{(-)} | V G_0 V | g_k^{(+)} \rangle = \langle g_k^{(-)} | V G_0 V | g_{k-1}^{(+)} \rangle &= \beta_{k-1}, && (3.54)\\
\langle g_k^{(-)} | V G_0 V | g_k^{(+)} \rangle &= \alpha_k, && (3.55)\\
\langle g_k^{(-)} | V G_0 V | g_l^{(+)} \rangle &= 0 \qquad \text{for} \quad |k-l| \geq 2 && (3.56)
\end{aligned}$$

and $|g_1^{(+)}\rangle = |\phi_{\mathrm{i}}\rangle \langle \phi_{\mathrm{f}} | V | \phi_{\mathrm{i}} \rangle^{-1/2}$, $\langle g_1^{(-)}| = \langle \phi_{\mathrm{f}} | V | \phi_{\mathrm{i}} \rangle^{-1/2} \langle \phi_{\mathrm{f}}|$ then in analogy with formula (3.42)

$$T_{\mathrm{fi}}^N = \langle \phi_{\mathrm{f}} | V | g_1^{(+)} \rangle (M^{-1})_{11} \langle g_1^{(-)} | V | \phi_{\mathrm{i}} \rangle = \frac{\langle \phi_{\mathrm{f}} | V | \phi_{\mathrm{i}} \rangle}{1-\alpha_1 -} \frac{\beta_1^2}{1-\alpha_2 -} \frac{\beta_2^2}{1-\alpha_3 -} \cdots \frac{\beta_{N-1}^2}{1-\alpha_N}. \tag{3.57}$$

It is simple to show by mathematical induction that vectors $|g_i^{(\pm)}\rangle$ with the properties (3.53)-(3.56) can be constructed from $|g_1^{(\pm)}\rangle$ according to the recurrence relations

$$
\begin{aligned}
\langle r_k^{(-)}| &= \langle g_k^{(-)}|VG_0 - \beta_{k-1}\langle g_{k-1}^{(-)}|, & (3.58)\\
|r_k^{(+)}\rangle &= G_0V|g_k^{(+)}\rangle - \beta_{k-1}|g_{k-1}^{(+)}\rangle, & (3.59)\\
\alpha_k &= \langle g_k^{(-)}|V|r_k^{(+)}\rangle = \langle r_k^{(-)}|V|g_k^{(+)}\rangle, & (3.60)\\
\langle s_k^{(-)}| &= \langle r_k^{(-)}| - \alpha_k\langle g_k^{(-)}|, & (3.61)\\
|s_k^{(+)}\rangle &= |r_k^{(+)}\rangle - \alpha_k|g_k^{(+)}\rangle, & (3.62)\\
\beta_k &= \langle s_k^{(-)}|V|s_k^{(+)}\rangle^{1/2}, & (3.63)\\
\langle g_{k+1}^{(-)}| &= \beta_k^{-1}\langle s_k^{(-)}|, & (3.64)\\
|g_{k+1}^{(+)}\rangle &= \beta_k^{-1}|s_k^{(+)}\rangle. & (3.65)
\end{aligned}
$$

It is shown in the reference [31] that SLM is equivalent to the method of continuous fractions (MCF) of J. Horáček and T. Sasakawa [36, 37]. It is simple to show in the same way that GSLM is equivalent with the generalization of MCF for off-diagonal T-matrix elements developed also by J. Horáček and T. Sasakawa [38].

Equivalence of GSLM and Wynn's epsilon algorithm

In this paragraph we prove that our generalization of the Schwinger-Lanczos method is mathematically equivalent to the Wynn's epsilon algorithm. This equivalence does not mean, however, that both methods are equally efficient when used as tools for numerical calculations.

It is obvious from (3.58) - (3.65) that the numbers α_j, β_j needed for calculation of T_{fi}^N can be expressed in terms of the quantities $\langle\phi_{\mathrm{f}}|V(G_0V)^k|\phi_{\mathrm{i}}\rangle$, which constitute of the Born series for T_{fi} (for the determination of the T_{fi}^N only the quantities with $k < 2N$ are needed). The algorithm (3.58) - (3.65) together with the equation (3.57) can thus be understood as means of re-summation of the Born series. It is therefore interesting to compare this algorithm with another algorithms for acceleration of convergence of power series.

Let us write the T-matrix in terms of the Born series

$$T_{\mathrm{fi}} = \langle\phi_{\mathrm{f}}|V|\phi_{\mathrm{i}}\rangle + \langle\phi_{\mathrm{f}}|VG_0V|\phi_{\mathrm{i}}\rangle + \langle\phi_{\mathrm{f}}|VG_0VG_0V|\phi_{\mathrm{i}}\rangle + \ldots \tag{3.66}$$

Introducing a coupling constant $V \to \lambda V$ this becomes a power series

$$T(\lambda) = \sum_{k=0}^{\infty} a_k\lambda^k = \lim_{n\to\infty} s_n, \tag{3.67}$$

with $a_0 = 0$ and $a_k = \langle\phi_{\mathrm{f}}|V(G_0V)^{k-1}|\phi_{\mathrm{i}}\rangle$ for $k > 0$. Formally, the sum of this series is defined as the limit of the sequence $s_0, s_1, s_2, \ldots$ $\left(s_n = \sum_{k=1}^{n} a_k\lambda^k\right)$. In reality, however, this limit often does not exist or the series converges very slowly. Several methods how to accelerate the convergence can be found in the literature (Padé approximation, Shanks transformation, etc.). The Shanks transformation [39] of the sequence $\{s_n\}_{n=0}^{\infty}$ of an order k is the sequence $\{e_k(s_n)\}_{n=0}^{\infty}$ defined by the following ratio of determinants

$$e_k(s_n) = \begin{vmatrix} s_n & \dots & s_{n+k} \\ b_{n+1} & \dots & b_{n+k+1} \\ \vdots & \ddots & \vdots \\ b_{n+k} & \dots & b_{n+2k} \end{vmatrix} \Bigg/ \begin{vmatrix} 1 & \dots & 1 \\ b_{n+1} & \dots & b_{n+k+1} \\ \vdots & \ddots & \vdots \\ b_{n+k} & \dots & b_{n+2k} \end{vmatrix}, \tag{3.68}$$

where the abbreviation $b_j = s_j - s_{j-1} = a_j\lambda^j$ was used. Shanks showed that this transformation is equivalent to the Padé approximant $[n+k,k]_T(\lambda)$. The expression (3.68) is not convenient for numerical calculations due to occurrence of determinants. However, as shown by Wynn, the quantities $e_k(s_n)$ can be expressed in terms of another quantities $\epsilon_i^{(j)}$ obtained from the following nonlinear recurrence scheme (Wynn's epsilon algorithm - see [40])

$$\epsilon_{-1}^{(n)} = 0 \qquad \epsilon_0^{(n)} = s_n \tag{3.69}$$

$$\epsilon_{k+1}^{(n)} = \epsilon_{k-1}^{(n+1)} + 1/[\epsilon_k^{(n+1)} - \epsilon_k^{(n)}]. \tag{3.70}$$

Both quantities are related as follows

$$\epsilon_{2k}^{(n)} = e_k(s_n) \text{ and } \epsilon_{2k+1}^{(n)} = 1/e_k(a_n\lambda^n). \tag{3.71}$$

To accelerate the convergence of the sequence $\{s_n\}_{n=0}^{\infty}$ by means of the Shank's transformation means to replace the sequence $\{s_n\}_{n=0}^{\infty}$ by $\{e_n(s_0)\}_{n=0}^{\infty}$. In what follows we prove that the numbers $T_{\text{fi}}^{(N)}$ obtained from GSLM coincide with $e_N(s_0)$.

According to the recurrence relations (3.58) - (3.65), the vectors $\{|g_k^{(+)}\rangle\}_{k=1}^{N}$ span the same space (the Krylov space) as the vectors

$$\{|p_k\rangle\}_{k=1}^{N} = \{|\phi_{\text{i}}\rangle, G_0V|\phi_{\text{i}}\rangle, ..., (G_0V)^{N-1}|\phi_{\text{i}}\rangle\} \tag{3.72}$$

and vectors $\{\langle g_k^{(-)}|\}_{k=1}^{N}$ the same as

$$\{\langle q_k|\}_{k=1}^{N} = \{\langle\phi_{\text{f}}|, \langle\phi_{\text{f}}VG_0, ..., \langle\phi_{\text{f}}|(VG_0)^{N-1}\}. \tag{3.73}$$

Thus from the equation (3.52), $T_{\text{fi}}^{(N)}$ can be written as

$$T_{\text{fi}}^{N} = \sum_{k,l=1}^{N} \langle\phi_{\text{f}}|V|p_k\rangle(M^{-1})_{kl}\langle q_l|V|\phi_{\text{i}}\rangle = \sum_{k,l=1}^{N} b_k(M^{-1})_{kl}b_l, \tag{3.74}$$

where

$$M_{kl} = \langle q_k|V - VG_0V|p_l\rangle = b_{k+l-1} - b_{k+l}. \tag{3.75}$$

Using the Cramer's rule $(M^{-1})_{kl} = (-1)^{k+l}m_{kl}/|M|$ (where m_{kl} are the minors of the matrix M), the T-matrix is converted into the form $T_{\text{fi}}^{(N)} = t/|M|$ with

$$t = \sum_{k,l} b_k b_l m_{kl}(-1)^{k+l} = \sum_k b_k B_k. \tag{3.76}$$

Here B_k are obtained from the matrix M by replacing the k^{th} column of M by the vector $(b_1, b_2, ..., b_N)$

$$B_k \equiv \begin{vmatrix} b_1 - b_2 & b_2 - b_3 & \dots & b_1 & \dots & b_N - b_{N+1} \\ b_2 - b_3 & b_3 - b_4 & \dots & b_2 & \dots & b_{N+1} - b_{N+2} \\ \vdots & \vdots & & \vdots & & \vdots \\ b_N - b_{N+1} & b_{N+1} - b_{N+2} & \dots & b_N & \dots & b_{2N-1} - b_{2N} \end{vmatrix}. \tag{3.77}$$

If we interchange the first and the k-th column and subsequently subtract the new first column from the second, then second from the third, ..., $(k-1)$-th from the k-th we obtain

$$B_k = \begin{vmatrix} b_1 & \dots & b_k & b_{k+1} - b_{k+2} & \dots & b_N - b_{N+1} \\ b_2 & \dots & b_{k+1} & b_{k+2} - b_{k+3} & \dots & b_{N+1} - b_{N+2} \\ \vdots & & \vdots & \vdots & & \vdots \\ b_N & \dots & b_{N+k-1} & b_{N+k} - b_{N+k+1} & \dots & b_{2N-1} - b_{2N} \end{vmatrix}. \tag{3.78}$$

Repeated use of the formula

$$\begin{vmatrix} a_1 + b_1 & A_{12} & \dots & A_{1N} \\ \vdots & \vdots & & \vdots \\ a_N + b_N & A_{N2} & \dots & A_{NN} \end{vmatrix} = \begin{vmatrix} a_1 & A_{12} & \dots & A_{1N} \\ \vdots & \vdots & & \vdots \\ a_N & A_{N2} & \dots & A_{NN} \end{vmatrix} + \begin{vmatrix} b_1 & A_{12} & \dots & A_{1N} \\ \vdots & \vdots & & \vdots \\ b_N & A_{N2} & \dots & A_{NN} \end{vmatrix} \tag{3.79}$$

yields

$$t = \sum_{k=1}^{N} b_k \sum_{l=k}^{N} (-1)^{N+l} C_{l+1} \tag{3.80}$$

with

$$C_{l+1} = \begin{vmatrix} b_1 & \dots & b_l & b_{l+2} & \dots & b_{N+1} \\ b_2 & \dots & b_{l+1} & b_{l+3} & \dots & b_{N+2} \\ \vdots & & \vdots & \vdots & & \vdots \\ b_N & \dots & b_{N+l-1} & b_{N+l+1} & \dots & b_{2N} \end{vmatrix}. \tag{3.81}$$

Changing the order of the sums we obtain

$$t = \sum_{l=1}^{N} \sum_{k=1}^{l} (-1)^{N+l} b_k C_{l+1} = \sum_{l=1}^{N} (-1)^{N+l} s_l C_{l+1}, \tag{3.82}$$

which is the first row expansion of

$$t = (-1)^N \begin{vmatrix} s_0 & s_1 & \dots & s_N \\ b_1 & b_2 & \dots & b_{N+1} \\ \vdots & \vdots & \ddots & \vdots \\ b_N & b_{N+1} & \dots & b_{2N} \end{vmatrix}. \tag{3.83}$$

Furthermore

$$|M| = \begin{vmatrix} b_1 - b_2 & \dots & b_N - b_{N+1} \\ \vdots & \ddots & \vdots \\ b_N - b_{N+1} & \dots & b_{2N-1} - b_{2N} \end{vmatrix} = \sum_k (-1)^{N+k+1} C_k, \tag{3.84}$$

which is the first row expansion of the determinant

$$(-1)^N \begin{vmatrix} 1 & 1 & \dots & 1 \\ b_1 & b_2 & \dots & b_{N+1} \\ \vdots & \vdots & \ddots & \vdots \\ b_N & b_{N+1} & \dots & b_{2N} \end{vmatrix}. \tag{3.85}$$

Comparing $t/|M|$ with the definition (3.68) we clearly see that $T_{\rm fi}^{(N)} = e_N(s_0) = [N/N]_T(\lambda)$. This completes the proof.

3.4 Application and comparison of the methods

As it was shown in the previous section the GSLM and WEA are fully equivalent and should therefore yield same results. In fact the two methods are quite different from the numerical point of view. Especially in the case of strongly divergent Born series we expect the performance of WEA to be rather poor, because relevant information about the dynamic is lost by storing large terms of the divergent series in computer memory with a limited accuracy.

In the derivation of GSLM we have seen that a more flexible basis was used in GSLM than that for SLM and therefore GSLM is expected to converge more rapidly. On the other hand more calculations is needed for one iteration of GSLM.

To compare the performance of SLM, GSLM and WEA on the physically relevant calculation we have chosen the nonlocal resonance model of Gertitschke and Domcke [41] for the dissociative attachment of an electron to H_2 molecule. The importance of the nonlocal effects for this system has been emphasized [41, 5] and usual methods for solving the Schrödinger equation can not be applied. The construction of the model is described in detail elsewhere [16, 6, 41] but there are misprints in [41]. The correct model functions are [42]

$$V_0(R) = 0.1742[e^{-2.053(R-R_0)} - 2e^{-1.027(R-R_0)}] + 0.0279, \tag{3.86}$$
$$V_{\rm d}(R) = 0.0639[e^{-2.371(R-R_0)} - 0.0358e^{-1.185(R-R_0)}], \tag{3.87}$$
$$V_{{\rm d}\epsilon}(R) = \sqrt{\frac{1}{2\pi}\sum_{i=1}^{3} A_i(\epsilon/B_i)^{3/2}e^{-\epsilon/B_i}}[1+0.126(R+1.606)^2]^{-1}, \tag{3.88}$$

where $R_0 = 1.398$ is the equilibrium distance of nuclei in H_2 molecule and the values of constants A_i, B_i are

$$\begin{array}{lll} A_1 = 0.6711 & A_2 = 0.2246 & A_3 = 0.0942 \\ B_1 = 0.1837 & B_2 = 0.0919 & B_3 = 0.0246. \end{array}$$

Before we compare the numerical performance of SLM, GSLM and WEA for the model (3.86)–(3.88) we present some general remarks about the application of the methods to AD, DA and VE processes. First of all we have to show that the T-matrixes derived for the processes in previous chapter are of the form (3.34) which was the starting point of the derivation of the methods. Observe that (skipping the unnecessary subscripts) both the $T_{\rm AD}$ and $T_{\rm VE}$, equations (2.74) and (2.78) are of the form

$$T = \langle\chi_{\rm f}|V^*_{{\rm d}\epsilon}|\psi\rangle, \qquad (3.89)$$

where

$$|\psi\rangle = |\phi\rangle + G_Q f|\psi\rangle. \qquad (3.90)$$

The vector $|\phi\rangle$ is the scattering solution in the potential $V_{\rm d}$ for the case of AD and $|\phi\rangle = G_Q V_{{\rm d}\epsilon}|\chi_{\rm i}\rangle$ for VE. Formal solution of (3.90) is

$$|\psi\rangle = (1 - G_Q f)^{-1}|\phi\rangle = (f - fG_Q f)^{-1} f|\phi\rangle. \qquad (3.91)$$

Substitution of this expression to (3.89) yields

$$T = \langle\chi_{\rm f}|V^*_{{\rm d}\epsilon} f^{-1} f(f - fG_Q f)^{-1} f|\phi\rangle, \qquad (3.92)$$

which is exactly of the form (3.34) and the variational approach (3.51) - (3.57) can be applied with $\langle\phi_f| \to \langle\chi_{\rm f}|V^*_{{\rm d}\epsilon} f^{-1}$, $V \to f$, $G_0 \to G_Q$ and $|\phi_i\rangle \to |\phi\rangle$ and with the vectors $|g_k^{(\pm)}\rangle$ and the numbers α_k, β_k given by the recurrence (3.58) - (3.65). There are two ways how to avoid the occurrence of f^{-1}. First is to rewrite T as

$$T = \langle\chi_{\rm f}|V^*_{{\rm d}\epsilon}|\phi\rangle + \langle\chi_{\rm f}|V^*_{{\rm d}\epsilon} G_Q f(f + fG_Q f)^{-1} f|\phi\rangle, \qquad (3.93)$$

and to calculate $\langle\chi_{\rm f}|V^*_{{\rm d}\epsilon} G_Q f(f+fG_Q f)^{-1} f|\phi\rangle$ with $\langle\phi_f| = \langle\chi_{\rm f}|V^*_{{\rm d}\epsilon} G_Q$ instead. We did our calculations in the second way, starting directly from (3.92), but rewriting the algorithm (3.58)-(3.65) for vectors $\langle g_k^{;(-)}| = \langle g_k^{(-)}|V$. This only changes the order of operators V and G_0 in (3.65) and V is not present in (3.60) and (3.63). The starting vector is $\langle g_1^{;(-)}| = \langle\chi_{\rm f}|V^*_{{\rm d}\epsilon}|\phi\rangle^{-1/2}\langle\chi_{\rm f}|V^*_{{\rm d}\epsilon}$.

The accurate calculation of the DA cross section in the threshold region is known to be a difficult task. It turns out that GSLM for DA converges rather slowly for energies near the threshold. As was shown in [29] and also discussed in section 3.2 the convergence can be accelerated if a certain local approximation $f_{\rm loc}$ is subtracted from f and added to $V_{\rm d}$. The formula (3.92) and the following discussion remains valid for this partitioning of the interaction only with f replaced by $f' = f - f_{\rm loc}$ and G_Q replaced by $G_{\rm loc}$ which is the Green function for the potential $V_d + f_{\rm loc}$. In the following we will call this method "the calculation with subtraction of local approximation". The local approximation $f_{\rm loc}$ used for the calculation will be that of equation (3.33).

We present a numerical comparison of the above mentioned methods as applied to the calculation of DA cross section of electrons to hydrogen atoms in the rest of this section. The process is described here by the nonlocal resonance model (3.86)–(3.88). All the calculations were done in the REAL*8 fortran77 arithmetics and the wave functions were calculated for $R < 8$ on the grid using 1000 mesh-points. The wave functions and the Green function were first found using the methods of section 3.1. Expansion (3.26) was used for evaluation of the nonlocal potential f. 24 expansion functions guarantee convergence for all the calculations discussed in this section.

Let us first discuss the original SL method. To calculate the T-matrix $T_D^N A$, using N iterations of the method N basis functions $\{|g_i\rangle\}_{i=1}^N$ are needed. We denote as σ_N the cross section obtained from (2.64) with $T_{\rm DA} = T_{\rm DA}^N$.

To evaluate the T-matrix using GSLM to the same order N, $2N$ basis functions $\{|g_i^{\pm}\rangle\}_{i=1}^{N}$ are required. To account for this we denote as σ_{2N} the cross section derived from T_{DA}^{N} in this case. The most time-consuming step in the calculation is the application of the nonlocal potential f to a wave function $|\psi\rangle$ (calculation of an element $\langle\psi'|f|\psi\rangle$ is much faster). In the SLM and GSLM this needs to be done N and $2N$ times respectively. The calculation of $e_N(S_0)$ with WEA requires knowledge of the matrix elements

$$\langle\phi_{\mathrm{f}}|V|\phi_{\mathrm{i}}\rangle, \langle\phi_{\mathrm{f}}|VG_0V|\phi_{\mathrm{i}}\rangle, ..., \langle\phi_{\mathrm{f}}|V(G_0V)^{2N-1}|\phi_{\mathrm{i}}\rangle,$$

which means $2N$ applications of f. We denote as σ_{2N} the cross section obtained from $T_{\mathrm{DA}}^{N} = e_N(s_0)$ in this case. Thus N measures to a large extent the time of the calculation of σ_N in all three methods.

As is well known the DA cross section changes dramatically when energy of the incident electron increases above the threshold. For this reason we found it necessary to test all methods for two energies; one just above the threshold and one sufficiently high above the threshold.

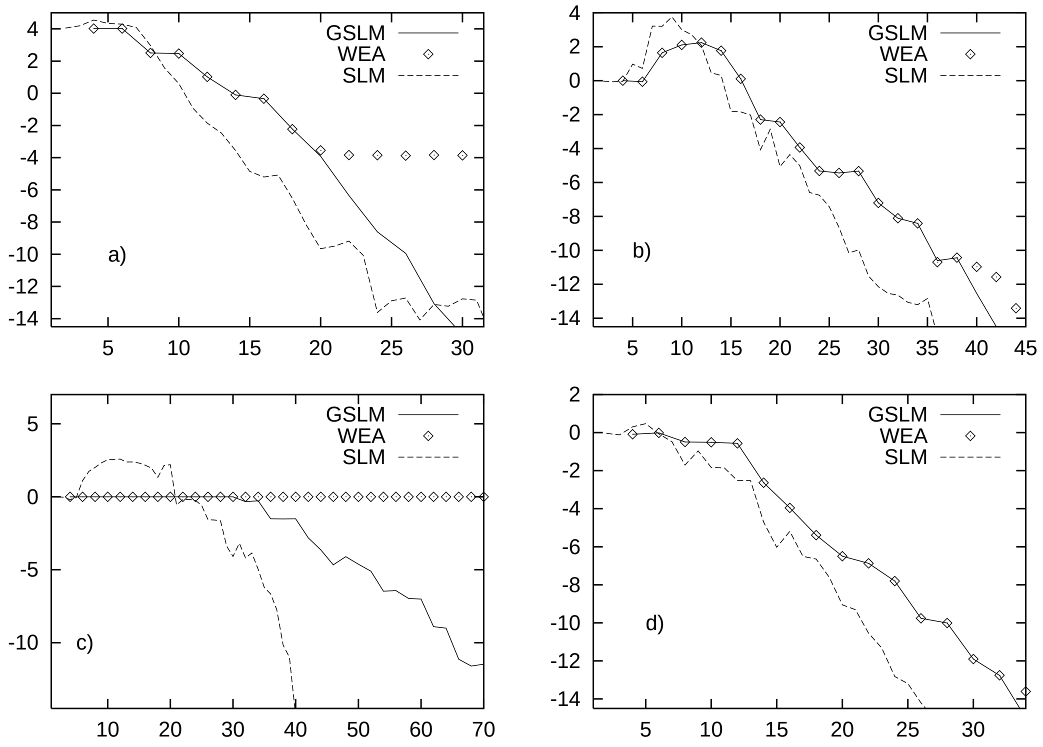

Figure 3.1: Convergence rates for the calculation of the e^-+H_2 dissociative attachment cross section using SLM, GSLM and WEA respectively. Logarithm (base 10) of the relative error is plotted against the number of calculation steps (see the text). The first two graphs (a and b) contain the data for the electron energy $E_{\mathrm{el}} = 8$ eV and the last two (c and d) for $E_{\mathrm{el}} = 3.72$ eV (just above the threshold). Local approximation (see the text) was subtracted from the nonlocal potential f in the case of b and d.

Numerical performance of all the methods is shown in Figure 3.1. Logarithm (base 10) of the relative error $|\sigma_N - \sigma_\infty|/\sigma_\infty$ is plotted against the number of iterations N. The value σ_N with N sufficiently large (so that computer representation of σ_N does not change with increasing N) is taken as σ_∞. Since WEA did not always fully converge it was necessary to take σ_∞ from other methods. Full line represents GSLM, dashed line SLM with T_{DA} computed according to (3.48)-(3.50) and diamonds represent the results of WEA.

Part (*a,b*) of the figure shows the rate of convergence of all three methods for the energy of the incoming electron E_{el} =8 eV (*a,b*) which is which is far from the DA threshold 3.7119 eV. Results for an energy close to DA threshold, $E_{\mathrm{el}} = 3.72$, are plotted in parts (*c,d*) of the Figure 3.1.

For the higher energy, E_{el} =8 eV, the results of WEA and GSLM are indistinguishable for the first 8-9 steps (graph *a*). Than after giving roughly four significant figures of σ, WEA fails to converge due to the accumulation of numerical errors. Iterations of GSLM remain stable and converge fast. SLM remains stable too and with the same computer effort we obtain slightly better results than with GSLM. The performance of the WEA can be improved with the subtraction of the local approximation (see graph *b*).

If the energy of the incident electrons is very close to the threshold, 3.72 eV, the Born series diverges strongly and also the WEA fails to yield convergent results. The method is thus completely useless in this energy range (graph *c*). On the other hand, GSLM and SLM converge even in this case (though slowly). Subtraction of the local potential (graph *d*) improves the convergence and WEA and GSLM give practically identical results.

We can conclude that SLM converges almost half as fast as GSLM in all given examples, but GSLM requires two times more computer time. As the result SLM is a little bit faster if the same precision is required. Original SLM method which proved so successful in all previous calculations represents thus the most reliable of the discussed methods. It is numerically stable, converges even without modifications of the nonlocal potential for all energies. The generalized method GSLM yields results very similar to that of SLM. The WEA as well as the Born series cannot be generally used without significant modifications of the underlying interactions.

Chapter 4

Dynamics of H_2^- collision complex

An improved nonlocal resonance model for the description of the nuclear dynamics of the H_2^- collision complex is developed in this section. The model is based on the *ab initio* electron-H_2 scattering data of Berman et al. at short internuclear distances, the *ab initio* data of Senekowitsch et al. for the bound $^2\Sigma_u^+$ state of H_2^- at intermediate distances, and exhibits the correct polarization interaction at large internuclear distances. Cross sections for associative detachment and dissociative attachment to rotationally and vibrationally excited molecules were calculated for a wide range of energies and angular momenta with full inclusion of nonlocal effects. The calculated associative-detachment rate constant at 300 K is $3.8 \times 10^{-9}\,\mathrm{cm^3s^{-1}}$, which is significantly larger than the experimental value reported by Schmeltekopf et al. A series of narrow low-energy orbiting resonances was found in the associative-detachment cross section. Our results compare well with previous calculations of dissociative attachment cross sections within the nonlocal resonance model. The dissociative attachment cross section for vibrationally and rotationally hot H_2 (T = 1400 K) has been calculated and compared with the experimental data of Allan and Wong. It is demonstrated that the local-complex-potential approximation is an excellent approximation for the associative detachment process, whereas it fails severely for the dissociative attachment process in H_2.

4.1 Introduction

The system H_2^- is the most fundamental molecular anion. It is unstable, with a very short lifetime ($\tau \sim 10^{-15}\,\mathrm{s}$). The dynamics of this complex is still not well understood, but it is important in a number of collisional processes. As examples of the most studied ones we mention dissociative attachment (DA)

$$\mathrm{e^-} + \mathrm{H_2} \rightarrow \mathrm{H} + \mathrm{H^-}, \tag{4.1}$$

vibrational excitation (VE)

$$\mathrm{e^-} + \mathrm{H_2}(\nu_i) \rightarrow \mathrm{e^-} + \mathrm{H_2}(\nu_f), \tag{4.2}$$

associative detachment (AD)

$$H + H^- \to H_2 + e^- \tag{4.3}$$

and, for scattering energies higher than the electron affinity of H, also collisional detachment (CD)

$$H + H^- \to H + H + e^-. \tag{4.4}$$

Understanding of these processes is important for a number of practical applications. AD and DA determine the thermal equilibrium densities of H^- ions and H_2 molecules in many astrophysical plasmas. Neutral molecules produced in AD are vibrationally excited and the emission spectra of such molecules are quite different from those of molecules excited by ultraviolet pumping or shock excitation [43]. DA of electrons to molecular hydrogen is thought to be the primary source of the H^- ions produced in hydrogen plasmas. These ions may serve for the generation of neutral particle beams, the injection of ions into controlled thermonuclear devices, or for electromagnetic propulsion of space vehicles.

In the early models of the H_2^- dynamics the interaction between the nuclei was described in the local-complex-potential approximation [44, 45, 46, 47, 48, 49], with empirically adjustable parameters and later with *ab initio* potentials [50], [5]. The importance of nonlocal effects was pointed out in [5]. Recently, the dynamics of nonlocal models has been studied [6], [41], [51], [52] for DA and VE in H_2.

In the present work we extend the nonlocal calculation also to the AD reaction as well as DA to rotationally excited molecules. The existing nonlocal resonance model for the H_2^- dynamics [6], [41] is modified to account for the long-range behaviour of the H_2^- potential-energy function, which is of relevance for the AD reaction. VE, DA and AD processes can thus be treated within a single model with no adjustable parameters. To our knowledge, this is the first calculation of AD cross sections as well as DA cross sections including rotational motion within the nonlocal resonance model. It should be mentioned that rotational effects on DA dynamics have been included in the effective-range model of Gauyacq [53], which also accounts for the nonlocal resonance effects in simplified manner. Rotational motion is also routinely included in multi-channel quantum-defect treatments of dissociative recombination, see, e. g., [54].

4.2 Theoretical description

We use the projection operator formalism, as described in the Chapter 2 for the description of the dynamics of H_2^- formed during the collision process. The resonant state important for low energy collisions is the ${}^2\Sigma_u^+$ state. There is another state of ${}^2\Sigma_g^+$ symmetry connected to H+H$^-$ asymptote, which is repulsive and does not contribute to the dynamics in the low energy region [50]. The lowest electronic state of H_2 molecule has ${}^1\Sigma_g^+$ symmetry so that the emitted electron must have an odd angular momentum l in order to preserve the overall ungerade symmetry [50]. We will further assume, that only the lowest angular momentum $l = 1$ (i. e. there are only terms with odd l in the expansion 2.44) contributes to $V_{d\vec{\epsilon}}$ so that $V_{d\epsilon l} = 0$ for $l > 1$ (see the equation (2.44)). This assumption is supported by *ab initio* calculations [16]. Using the formula (A.8) for the Wigner 3j symbols we find that the nonlocal potential (2.50) under these assumptions reads

$$f_J(E,R,R') = \int \mathrm{d}\epsilon V_{\mathrm{d}\epsilon}(R) \frac{(J+1)G_{0\,J+1}(E-\epsilon,R,R') + JG_{0\,J-1}(E-\epsilon,R,R')}{2J+1} V^*_{\mathrm{d}\epsilon}(R'), \tag{4.5}$$

where we used the notation $V_{\mathrm{d}\epsilon} \equiv V_{\mathrm{d}\epsilon 1}$, for simplicity. The wave function $\psi^I_J(R)$ for the associative detachment is found as solution of the integral equation (2.55). Note that the methods of Chapter 3 can still be used for the numerical solution of this equation. The two Green functions in the nonlocal potential f_J have to be expanded into two different basis sets formed by the states of neutral molecule H_2 with the angular momentum $J' = J+1$ and $J' = J-1$ respectively. Associative detachment cross section (2.61) reads [50]

$$\sigma_{AD}(\epsilon_{\mathrm{f}}, E) = \frac{2\pi g_{\mathrm{i}}}{KE} \cdot \frac{J_{\mathrm{f}}|t_{J=J_{\mathrm{f}}-1}(\nu_{\mathrm{f}}, J_{\mathrm{f}}, E)|^2 + (J_{\mathrm{f}}+1)|t_{J=J_{\mathrm{f}}+1}(\nu_{\mathrm{f}}, J_{\mathrm{f}}, E)|^2}{2J_{\mathrm{f}}+1}, \tag{4.6}$$

where we used the formula (A.8) again. Let us remind that (see 2.59)

$$t_J(\nu_{\mathrm{f}}, J_{\mathrm{f}}, E) = \int \mathrm{d}R \chi_{n_{\mathrm{f}}J_{\mathrm{f}}}(R) V^*_{\mathrm{d}\epsilon_{\mathrm{f}}}(R) \psi^I_J(R). \tag{4.7}$$

Dissociative attachment is calculated from the same T-matrix element and it is

$$\sigma_{DA}(\epsilon_{\mathrm{f}}, E) = \frac{8\pi^2\mu}{K^2(2J_{\mathrm{i}}+1)} \left[(J_{\mathrm{i}}+1)|t_{J=J_{\mathrm{i}}+1}(\nu_{\mathrm{i}}, J_{\mathrm{i}}, E)|^2 + J_{\mathrm{i}}|t_{J=J_{\mathrm{i}}-1}(\nu_{\mathrm{i}}, J_{\mathrm{i}}, E)|^2 \right]. \tag{4.8}$$

4.3 Construction of the model

We constructed a new nonlocal resonance model for the description of the nuclear dynamics of the H_2^- collision complex by modifying the long-range part of the model of Mündel, Berman, Domcke [6] (this model will be further referred to as MBD) to account for the proper long-range behaviour of the H_2^- potential-energy function.

Analytical form of the functions $V_d(R)$ and $V_{dk}(R)$ for the MBD model is given in the appendix B. The function $V_0(R)$ is constructed *via* a spline interpolation of the data given by Kołos and Wolniewicz [55]. The values of the free parameters in the model functions $V_d(R)$ and $V_{dk}(R)$ were chosen to reproduce *ab initio* fixed-nuclei electron-scattering data for internuclear distances ranging from 1 a. u. to 3 a. u. [16]. The R-dependence of the model potential functions of MDB for $R > 3$ a.u. represents therefore a somewhat arbitrary extrapolation. This was justified by the expectation of a small sensitivity of the DA cross section to the long-range part of interaction [6]. The AD cross section, on the other hand, should be rather sensitive to the long-range behaviour of the H_2^- potential. For large internuclear distances the ${}^2\Sigma_u^+$ state of H_2^- is (electronically) bound and the long-range behaviour of its energy is dominated by the polarization potential (Dalgarno and Kingston [56]). The potential energy of the H_2^- ion for the internuclear distances 3−20 a.u. was calculated by Senekowitsch et. al. using *ab initio* multiconfiguration-interaction methods [57].

The energy of the H_2^- bound state in the MBD model is given by (compare with the eq. (3.28))

$$V_1(R) = V_d(R) + \Delta(R), \tag{4.9}$$

where $\Delta(R)$ is the level shift of the discrete state potential V_d due to interaction with the continuum which is completely determined by the functions $V_0(R)$ and $V_{dk}(R)$ (see (3.24),(3.25),(3.28),(3.30)). It is clear that by adjusting $V_d(R)$ we can make $V_1(R)$ to be consistent with the *ab initio* results for intermediate [57] and the long [56] internuclear distances. Fortunately, we can do it in such a way that the new $V_d(R)$ joins smoothly with the original potential $V_d(R)$ from the MBD model for $R < 3$ a.u. Thus the new model is consistent also with the fixed-nuclei electron-H_2 scattering data of Berman, Mündel, Domcke [16].

The potential $V_1(R)$ for the new model together with the old $V_1(R)$ and $V_0(R)$ of MBD are shown in Figure 4.1. The analytic form of the new discrete state potential $V_d(R)$ is given in the appendix B. The discrete-continuum coupling element $V_{dk}(R)$ of the new model is the same as in the MBD model, see eq (23).

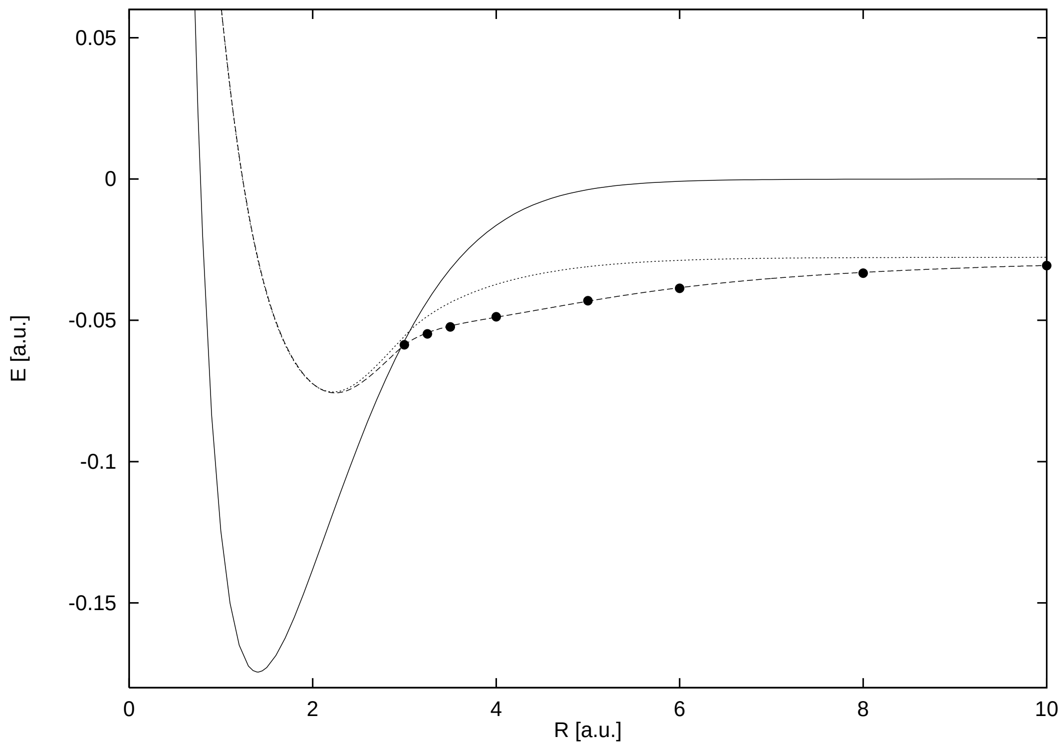

Figure 4.1: Potential function $V_0(R)$ of H_2 in its ground electronic state (full line) and potential function $V_1(R)$ of the ${}^2\Sigma_u^+$ state of H_2^- in the MBD model (dotted line) and in the new model (dashed line). *Ab initio* data of Senekowitsch et al. for H_2^- are plotted as full circles.

It should be mentioned that similar combinations of short-range, intermediate-range and long-range potentials have previously been adopted within the local-complex-potential approximation by Sakimoto [58] and Launay et al. [59]. In the intermediate range ($3 < R < 20\,\mathrm{a.u.}$) the *ab initio* ${}^2\Sigma_u^+$ potential-energy function is considerably more attractive than the polarization potential, which is of relevance for the AD cross section (see below).

4.4 Computational details

The cross sections for AD and DA were calculated using the methods described in the Chapter 3. The SLM has been employed to solve the integral equation (2.55) for a give J. Nonlocal potential has been expanded according to (3.23), i. e.

$$f_J(E,R,R') = \frac{J+1}{2J+1}\sum_{n=0}^{N}\chi_{n\,J+1}(R)F(E-E_n^{J+1},R,R')\chi_{n\,J+1}(R') + \\ + \frac{J}{2J+1}\sum_{n=0}^{N}\chi_{n\,J-1}(R)F(E-E_n^{J-1},R,R')\chi_{n\,J-1}(R'), \tag{4.10}$$

where

$$F(\epsilon,R,R') = \Delta(\epsilon,R,R') - \tfrac{i}{2}\Gamma(\epsilon,R,R'). \tag{4.11}$$

The functions $|\chi_{nJ}\rangle$ were obtained with a discrete variational representation (DVR) method using the Fourier basis on the interval $(0,10)$. This method also provides a discretization of the continuous spectrum [29]. Converged results were obtained with 100 Fourier functions for the DVR and with $N = 40$ functions in Eq. (4.10) for F_l. All the functions ψ_J^I, $\varphi_J^I(R)$, $\chi_{nJ}(R)$ and the Green's function G_{QJ} were calculated in the interval (0,10 a. u.) on a grid of typically M=2000 meshpoints. For the proper normalization of the scattering solution $\varphi_J^I(R)$ and for the calculation of the Green's function G_{QJ} the Schrödinger equation with the local potential $V_d(R) + W_l(R)$ was solved up to $R = 100\,\mathrm{a.u.}$ Convergence of the partial-wave sum for the total $\mathrm{H} + \mathrm{H}^-$ AD cross section, for a collision energy of 1eV requires the inclusion of angular momenta up to $J_\mathrm{f} = J_\mathrm{max} = 30$.

Separability of the ϵ- and the R-dependence in the coupling $V_{\mathrm{d}\epsilon}(R)$ is important for the numerical evaluation of the potential $f_J(E,R,R')$. Let us calculate how many steps are needed to calculate $\int \mathrm{d}R\, f_J(E,R,R')\psi(R')$ on the grid of M points and with N terms in the sum (4.10). In general we need $M \times N \times M = 16\cdot 10^7$ operations since result for each R is calculated as sum of N terms and integration over R'(M operations for trapezoidal rule). If the dependence on ϵ and R is separated in $V_{\mathrm{d}\epsilon}(R) = g(R)f(\epsilon)$, it is $F(\epsilon,R,R') = g(R)\tilde{F}(\epsilon)g(R')$ and integration over R' can be performed before the summation. As the result we need only $M\times N + M\times N = 16\cdot 10^4$ operations i. e. for separable potentials the calculation is expected to be $M/2 = 1000$ times faster. In our model (as in MBD) $V_{\mathrm{d}\epsilon}(R)$ is the sum of the three separable terms (B.6). Generalization of previous discussion for this case is straightforward.

4.5 Results and discussion

The calculated total AD cross section for $H + H^-$ and its partial-wave components are shown in Figure 4.2 on a doubly logarithmic scale. The results of the nonlocal model (full line) are compared with the results obtained in the local approximation (dashed line). The local approximation has been constructed as described in reference [6], i. e. $V_1(R)$ of eq. (4.9) is the real part of the local approximation. It is seen that the local AD cross section is in excellent agreement with the nonlocal result. The reason of this is the following. Only the nuclear dynamics in the region of large internuclear distances R is essential for the AD process in the low-energy region, and the nonlocal effects for such values of R are weak. The only important feature of the nuclear dynamics for small R (R less then crossing point of the potentials V_1 and V_0, *i. e.* 3 a. u.) is that the probability of the $H_2^- \to H_2 + e^-$ decay is large, and this is the feature contained in both local and nonlocal models (sufficiently large Γ).

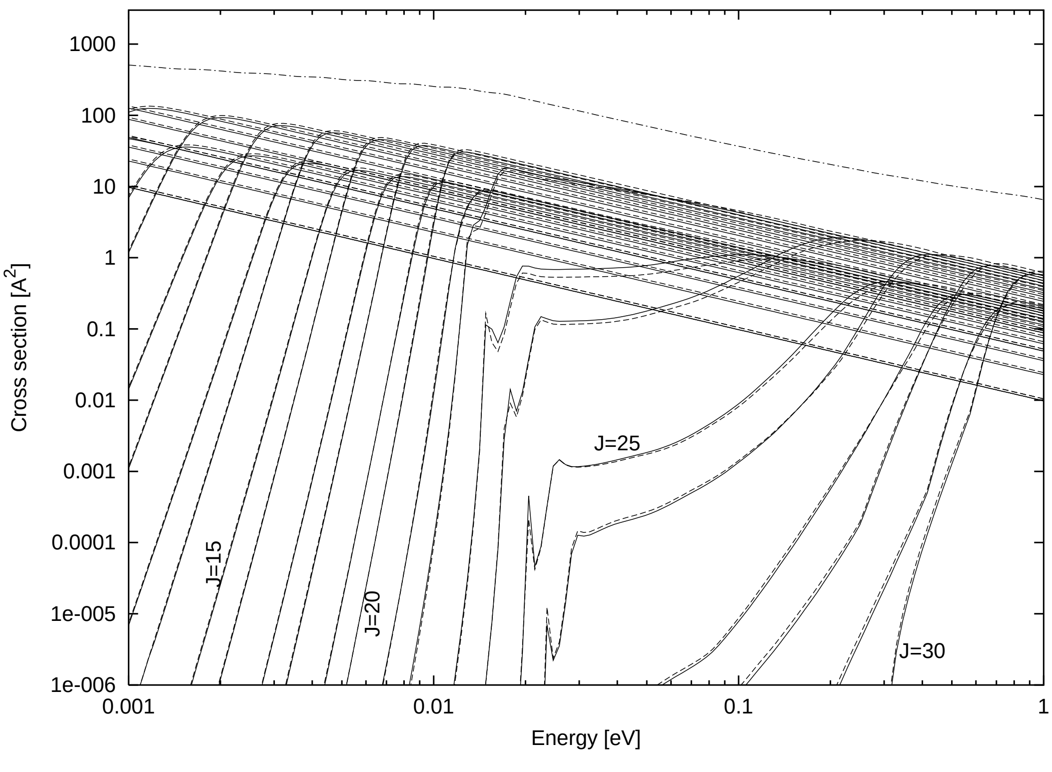

Figure 4.2: The total H+H$^-$ associative-detachment cross section (dotted-dashed line) and its partial-wave components (full lines) $J = 30, 29, ...$ (from the right). Results of the local approximation are given by dashed lines.

The local effective potential $V_1(R) + \frac{J(J+1)}{2\mu R^2}$ depicted in Figure 4.3 is an important tool for the interpretation of the AD process. Each partial component of the AD cross section is very small for energies below the centrifugal barrier (located in the region $R > 5$ a. u. in Figure 4.3) and increases with energy according to the threshold law $\sigma_J \sim E^{J-\frac{1}{2}}$. The cross section decreases above the centrifugal barrier, $\sigma_J \sim \frac{J+1}{E}$. Irregularities in the region E =0.02–0.2 eV and the change of slope of the total AD cross section near $E = 0.02$ eV are associated with the sudden switching of the inner repulsive barrier from $R \simeq 2$ a.u. to $R \simeq 4$ a. u. as J increases from $J = 22$ to $J = 23$.

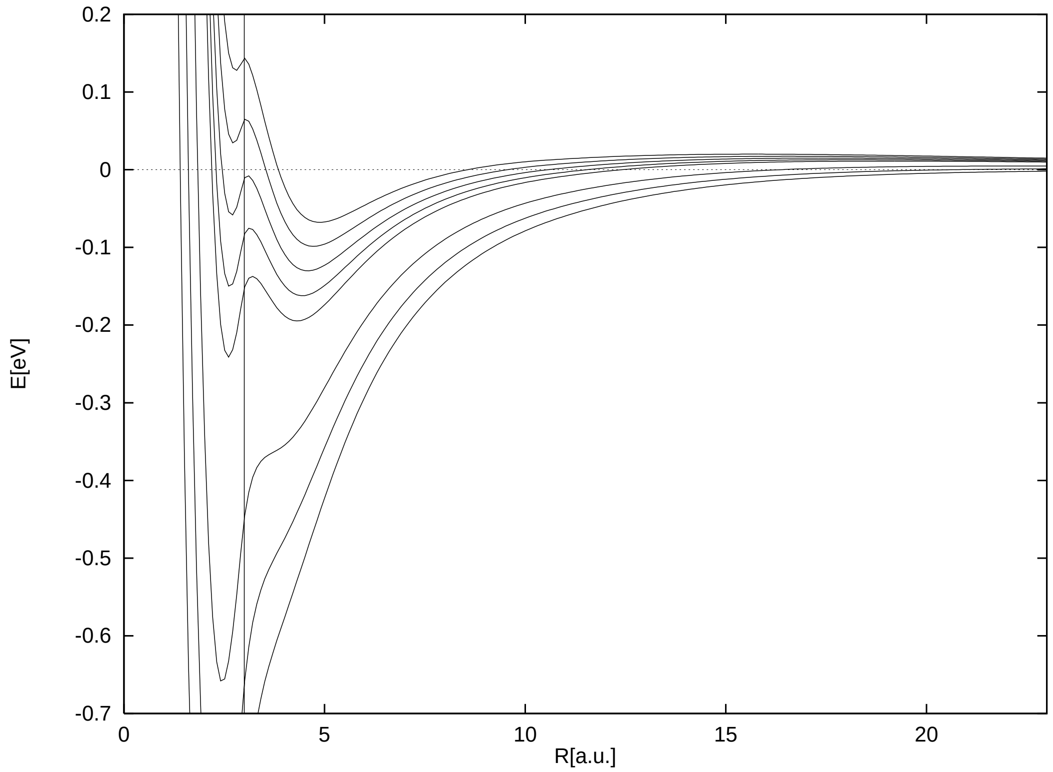

Figure 4.3: Effective potential $V_1(R) + \frac{J(J+1)}{2\mu R^2}$ for $J = 0, 10, 15, 20, 21, 22, 23, 24$ (from bottom to top). The vertical line at $R = 3$ gives the position where the potential $V_1(R)$ crosses the potential $V_0(R)$.

Upon closer inspection, the AD cross section exhibits weak and narrow resonance structures. These are clearly seen in the partial wave components $J = 23$–26 in the energy region 0.01–0.03 eV in Figure 4.2. These resonances are typical examples of orbiting resonances, which are a consequence of the particles being trapped in the region $R \simeq 4$–8 a. u. behind the centrifugal barrier. This phenomenon increases the AD probability, since the particle trapped in the resonance state has a better chance for the tunneling into the detachment region, $R < 3$ a. u. The shape (including the resonance structures) of the partial component $\sigma_J(E)$ depends essentially only on the parameter $\beta = \frac{J(J+1)}{2\mu}$ in the effective potential. The same is true for the $D^- + D$ AD, with a higher value of μ in the expression for β. This means that in the case of $D^- + D$ the distribution of the values β is more dense and there is thus a better chance to find a resonance near the maximum of $\sigma_J(E)$ for some J. Such a resonance is more clearly discernible in the total AD cross section. This is the case for the resonance in $\sigma_{32}(E)$ for $D^- + D$ collisions. A detailed view of such a resonance structure in the total $D + D^-$ AD cross section is given in Fig. 4.4. The width of this resonance is of the order of 1 meV. Such a structure presumably cannot be resolved in present-day collision experiments. The measurement of these structures would be a sensitive test of the long-range part of the H_2^- potential.

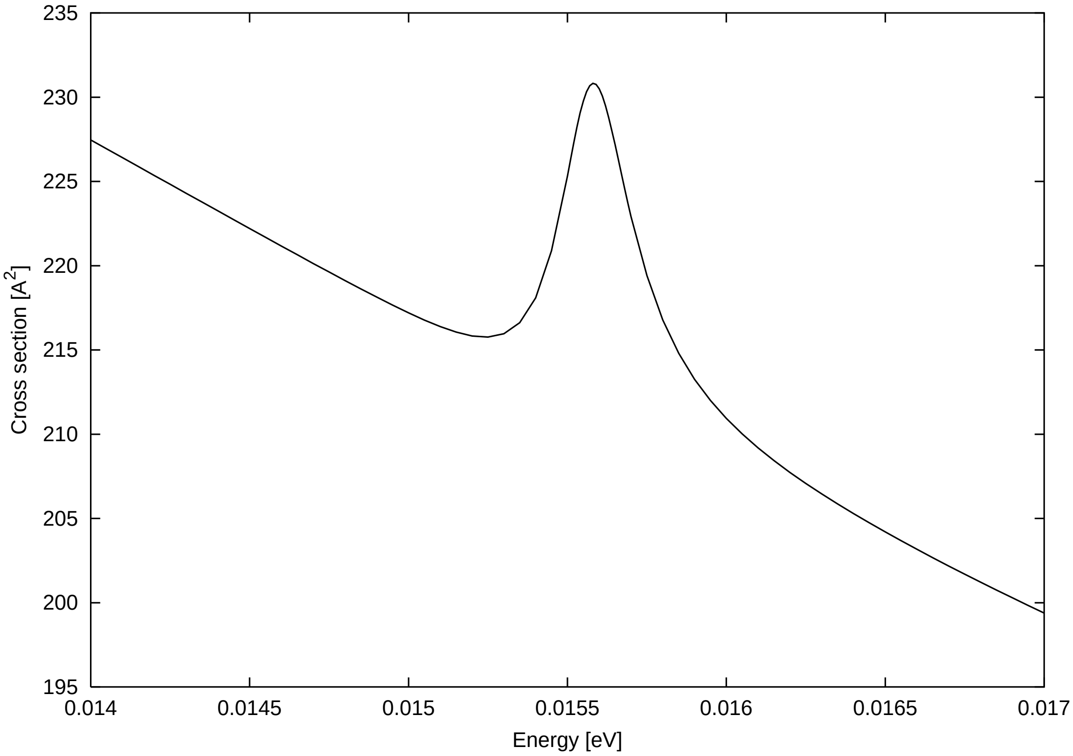

Figure 4.4: Detailed view of a resonance in the total cross section for the associative detachment of D^- in the collision with D. The partial wave $J = 32$ is responsible for this resonance.

Resonance structures in the $H + H^-$ AD cross section have previously been discussed by Sakimoto [58] within the local-complex-potential approximation. In Sakimoto's calculation the resonances only became visible when the imaginary part of the Bardsley-Wadehra complex potential [47, 48, 49] was reduced by at least a factor of 10 [58]. The imaginary part of the *ab initio* complex potential [6] is smaller than the imaginary part of the Bardsley-Wadehra potential (see Fig. 1 of [6]) and the presence of the barrier in the effective potential (Fig 4. 3.) for $J > 22$ also reduces the autodetachment probability. Therefore the resonance structures are apparent in the present calculation without artificial suppression of the imaginary part.

It has been known for some time that the local approximation performs very poorly for the DA and VE processes in H_2 [6], [41], [51], [52]. Considering that AD is just the reverse process to DA, the excellent performance of the local approximation for the AD process (cf. Fig. 4.2) is a bit surprising. The solution of this puzzle is given in Figure 4.5. Here the AD cross section $\sigma_{n\,J}$ is plotted for a number of final states χ_{nJ}, for a collision energy of 0.1 eV. It is clear from this figure that only high values of J and n contribute to the AD cross section. For

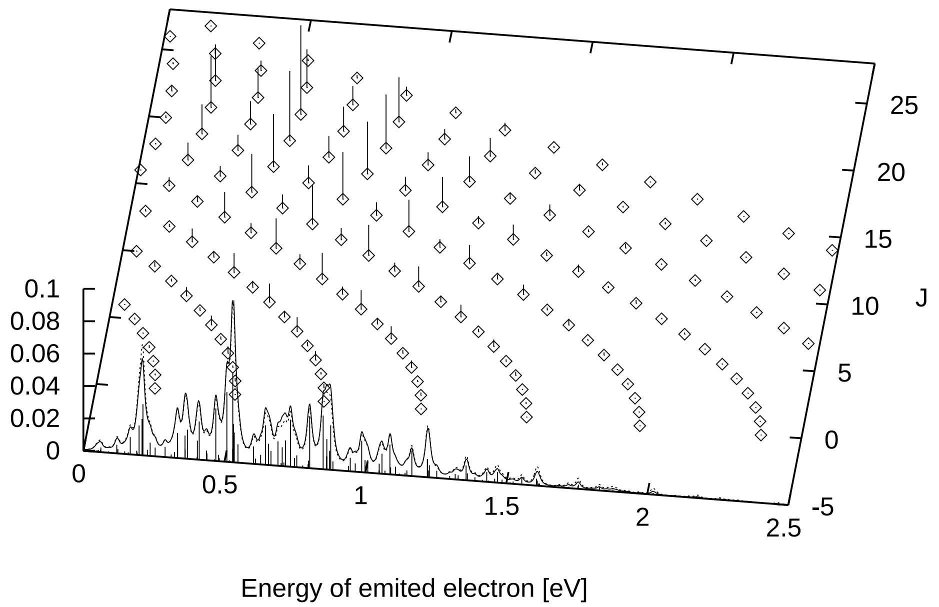

Figure 4.5: Final-state distribution in $H + H^-$ associative detachment at 0.1 eV collision energy. Relative probabilities for the different final states of H_2 and the energy spectrum of the released electron are shown. The energy of the emitted electron is plotted on the x-axis, the angular momentum J of the final H_2 state on the y-axis, and the cross section σ_J^ν (arb. units) on the z-axis. The calculated electron spectrum of the nonlocal model is given by the full curve; the dotted line gives the electron spectrum obtained in the local approximation.

these values the difference between the local and nonlocal calculations is small (at most a few per cent). In [6] and [41], on the other hand, the DA cross sections for small values of n and $J = 0$ were calculated. For these values of n, J the discrepancy between the nonlocal and local calculations for AD are pronounced, but the magnitude of these cross section is so small that they contribute negligibly to the total cross section. The same feature is seen in the electron spectrum in Figure 4.5. The difference between the local and nonlocal calculations is again small, except in the region where the probability of electron emission is small. The physical reason for this behaviour is clear. For the AD into final state χ_{nJ} with low n, J to occur, the particles have to get deep into the decay region (the minimum of the H_2 potential $V_0(R)$ is at $R \simeq 1.4$ a. u.). The probability for this is very small and strongly dependent on the details of the nonlocal dynamics in the region $R < 3$ a. u..

The only measurement on the $H + H^-$ AD process is the reaction rate at 300° K, 1.3×10^{-9}cm^{3}s^{-1}, of Schmeltekopf et al [60], who claim reliability of a factor of two. Our calculation gives 3.8×10^{-9}cm^{3}s^{-1}, which is almost three times larger than the experimental result and the Langevin value of 1.33×10^{-9} cm^{3}s^{-1}. To find out the reason why our value is so large we have compared our result with previous theoretical calculations: 2.0×10^{-9}cm^{3}s^{-1} (Browne and Dalgarno [61]), 1.89×10^{-9}cm^{3}s^{-1} (Bieniek and Dalgarno [50]) and 2.03 and 1.49×10^{-9}cm^{3}s^{-1}

(Launay et al. [59], their potentials V_1 and V_2 respectively). The AD reaction rate at 300° K is determined essentially by the long-range part of the potential ($R > 10$ a. u.). In the case of the models of Browne and Dalgarno [61], Bieniek and Dalgarno [50] and potential V_1 of Launay et al. [59] this part of the potential is approximately given by

$$-0.03887Re^{-0.7441R} - \frac{2.25}{R^4} - \frac{97}{R^6}. \tag{4.12}$$

This potential gives a reaction rate close to $2 \times 10^{-9}\mathrm{cm}^3\mathrm{s}^{-1}$. Our potential also possesses the proper polarization asymptotics $-\frac{2.25}{R^4} - \frac{97}{R^6}$, but it is much more attractive than (4.12) for $R < 20$ a. u.. The potential of Senekowitsch et al. [57] is ten times deeper than (4.12) in the relevant region, which rises the reaction rate by almost a factor of two. The potential V_2 of Launay et al. [59] is, like our potential, adjusted to the *ab initio* data of Senekowitsch et al. [57] for $3 < R < 20$ a. u. and should yield a rate coefficient which is significantly larger than the rate coefficient for potential V_1. The thermal rate coefficient reported by Launay et al. for potential V_2 is obviously incorrect. Sakimoto [58] has reported the rate constants for very low temperatures which appear to be consistent with the present results.

If the DA cross sections for $J = 0$ of the present model are compared with the results obtained with the MBD model, we find that the modification of the long-range part of the H_2^- potential function does not change the DA cross section much. Only the threshold region is affected; the peaking of the cross section at threshold is sharper. The calculated cross section for DA to H_2 in its ground state at threshold is 4.86×10^{-5}Å^2, which is three times larger than the experimental value 1.6×10^{-5}Å^2 of Schulz and Asundi [62].

As a byproduct of the AD calculations, we have extended the calculation of the DA cross section to $J > 0$ and $n > 0$. To compare our results with the measurement of Allan and Wong [7], we have averaged the DA cross sections over the Maxwell-Boltzmann distribution for the temperature $T = 1400$ K. The result is shown in Figure 4.6. To normalize the experimental data, we used the absolute cross-section value of Schulz and Asundi. The experimental curve is thus normalized in such a way that the maximum value is three times less than the maximum value of our calculation. The agreement between calculation and measurement is rather poor for higher energies ($E \sim 3.5$-4eV), which corresponds to attachment to H_2 in its ground vibrational state. The agreement is better for lower energies, i. e., for attachment to vibrationally excited states. It should be noted that the cross section for DA to the ground vibrational state is very sensitive to details of the model, because it is determined by the details of the wave function $\psi_l(R)$ in the vicinity of the equilibrium distance of H_2, where the wave function is very small due to the rapid decay of H_2^- at short internuclear distances.

4.6 Conclusions

We have improved the nonlocal resonance model for H_2^- proposed by Mündel, Berman and Domcke to account properly for the long-range behaviour of the

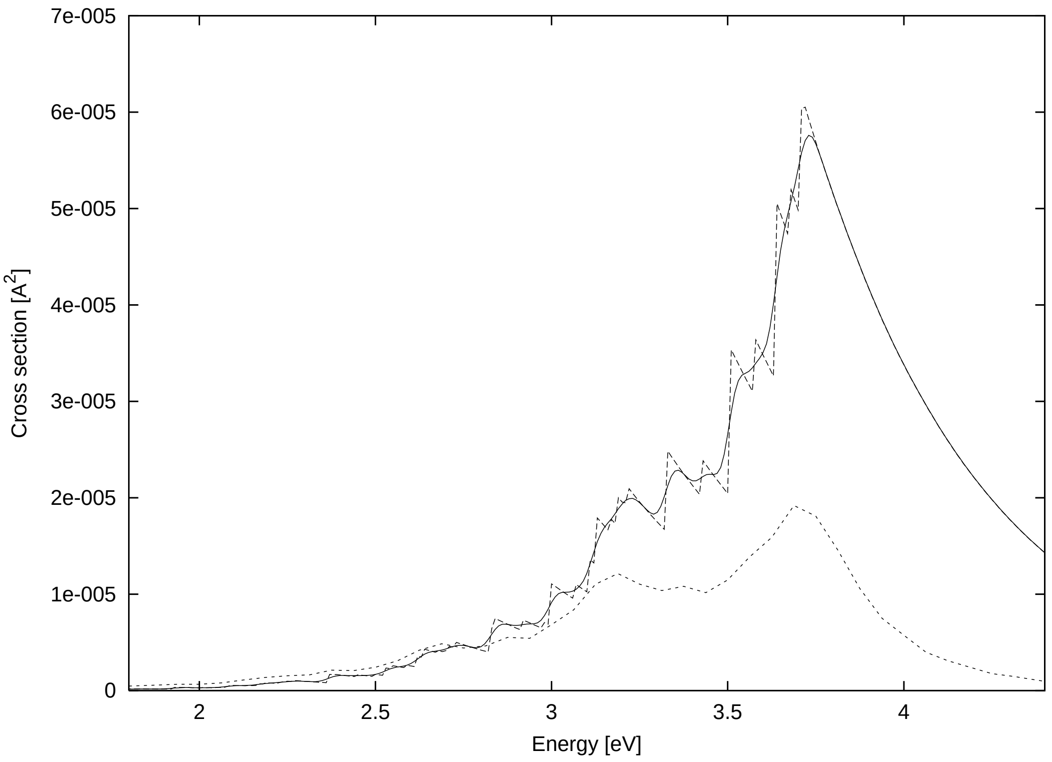

Figure 4.6: Cross section for dissociative attachment to H_2 in thermal equilibrium at 1400 K (long dashes). The full line was obtained by convolution with a Gaussian of the width 50 meV. Short dashes represent the experimental result of Allan and Wong, normalized to the threshold value of Schulz and Asundi.

H_2^- potential-energy function. The potential function of the improved model agrees with the *ab initio* data of Senekowitsch et al. at intermediate internuclear distances and exhibits the correct polarization interaction at large distances.

Using the SLM, we have performed converged quantum calculations of DA and AD cross sections for this improved nonlocal resonance model. It has been found that the measured thermal rate coefficient for $H + H^-$ AD is incompatible with the presumably accurate ${}^2\Sigma_u^+$ potential-energy function of Senekowitsch et al. The theory predicts a value which is about three times larger than the value of $1.3 \times 10^{-9}\,\mathrm{cm^3 s^{-1}}$ reported by Schmeltekopf et al. [60]. It has also been found that the AD cross section exhibits narrow orbiting resonances. These resonances appear for collision energies between 10 and 30 meV and their width is of the order of 1 meV. The location and width of the resonances depends sensitively on the long-range part of the interaction.

The local approximation gives results close to that of the fully nonlocal calculation for the total AD cross section and for the spectra of the released electron for electron energies less than 1.5 eV. The local approximation fails when the target states with small J and n are involved, which is the case in DA. It can be concluded that it is perfectly justified to determine an empirical local H_2^- potential-energy function by fitting experimental AD data. The fitting of experimental DA data within the local-complex-potential model, on the other hand, has no physical basis.

The comparison with experimental data shows that further improvement of the model is necessary. The calculated cross section for DA to H_2 molecules in the ground vibrational state, which is very sensitive to model parameters, is too large, and the increase of the DA cross section with ν appears to be too weak. More accurate *ab initio* calculations of the short-range part of the nonlocal H_2^- potential-energy function are necessary. More extensive and more accurate measurements of cross sections for this fundamental and practically relevant collision system would be very valuable.

Chapter 5

Resonant processes for hydrogen halides

A collision of a low-energy electron with a hydrogen halide represents a typical example of a molecular resonance process. The resonant character of the collision leads to large cross sections for inelastic and reactive processes, i.e., vibrational excitation (VE), dissociative electron attachment(DA) and the inverse process of associative detachment (AD). These processes have been studied by various authors both experimentally and theoretically.

Experimentally observed cross sections for the resonance processes exhibit unusual behaviour. The most interesting feature is the existence of pronounced threshold peaks in the VE cross sections observed first by Rohr and Linder [63, 3] for HCl and HF. The cross sections in the threshold region attain very high values and represent the highest vibrationally inelastic cross sections measured. The step-like structures in the DA cross section (Wigner cusps) first observed by Abouaf and Teillet-Billy [13] represent another striking feature of low-energy electron-HCl collisions. More recently, additional fine structure has been discovered in the $0 \to 1$ and $0 \to 2$ VE functions of HCl, which appears in the form of oscillations converging towards the DA threshold [12, 11].

Several theoretical models have been put forward to provide an explanation of these unusual phenomena. They are based on a variety of theoretical concepts such as the projection-operator formalism [64, 65, 66, 67, 68], the R-matrix formalism [69, 70, 71], or the zero-range potential model [72, 73]. The so-called non-local resonance model developed by Domcke and Mündel [67] has so far provided the most complete description of the resonance and threshold features observed in low-energy electron-HCl collisions [12, 74, 4]. This model describes qualitatively all the observed features: threshold peaks and broad resonances in the VE cross sections, Wigner cusps in the DA cross sections, as well as oscillatory structures in the VE cross sections below the threshold of the DA channel. This type of model has also been used by Horáček et al. for the calculation of VE and DA cross sections in HBr [32] and HI [75].

Associative detachment of halogen anions X^- in collision with hydrogen has been studied recently experimentally by Huels et al. [1]. No threshold structures like in electron-HX scattering are observed in those experiments. This is due to existence of many final states in the process and close vicinity of the respective thresholds. On the other hand the threshold phenomena like Wigner cusps can quite well be resolved in a measurement of the energy spectra of electrons released in the process. This assumption is supported by the results of Gauyacq [76] for the final state distribution of HX after the AD process and we present further evidence in this chapter. Such experiments are under preparation in Kaiserslautern. It is very useful to have a prediction of the electron spectra under different possible experimental condition before building actual experiment in order to optimize electron count rates and the energy resolution in the experimental setup.

In the following section we will present an improved nonlocal resonance model for electron-HCl collisions, which takes account of the dependence of the dipole-modified threshold exponent on the internuclear distance. The long-range part of the HCl^- potential-energy function has also been modified according to the most accurate *ab initio* calculations which are available [77]. Cross section for vibrational excitation and dissociative attachment are in better agreement with experiment than previous calculations. In particular the fine details in VE cross section below DA threshold are in a good agreement with experiment showing the quality of the used HCl^- potential.

AD cross sections for $H+Cl^-$collisions are then calculated in the next section with the same model including the final state distribution and the spectrum of the released electron. The results are discussed in detail and the realistic collision energy distribution expected in experiments is included into calculation. Finally, we add some results for $H+F^-$ collisions and discuss also preliminary results for $H+Br^-$ and $H+I^-$.

Sequence of nonlocal resonance models for HF^-, HCl^-, HBr^- and HI^- is interesting for the study of dependencies of the cross section for the respective resonant processes on the model; the systems are very similar, but the model parameters vary over certain range of values. Experiments for total AD cross sections for all these systems have been done by Huels et al [1] recently. In the table below we give for X =F,Cl,Br and I the depth D_0 of the potential well for the HX molecule, electron affinity E_a to the atom X, internuclear separation R_0 and the threshold exponent α_0 for equilibrium separation.

	X =F	X =Cl	X =Br	X =I
D_0[eV]	6.127	4.61	3.92	3.198
E_a[eV]	3.401	3.605	3.36	3.059
$R_0[a_0]$	1.733	2.409	2.67	3.05
α_0	$-^*$	0.36	0.424	0.48

Dipole moment increases in the sequence HI, HBr, HCl, HF. The molecule HF posses a supercritical dipole, so that the threshold exponent α is not well defined for this molecule and the threshold behavior (2.84) must be modified [78, 52].

5.1 New model for e^-+HCl scattering

The nonlocal resonance model of Domcke and Mündel [67] (henceforth referred to as DM) provided the most complete description of the system. However as applied to the HCl molecule, the DM model has certain shortcomings. The main parameter determining the cross sections at very low energies is the threshold exponent α (see the section 2.5.). This parameter is, in the case of polar molecules, determined by the dipole moment, which in turn depends on the internuclear distance. This means that the threshold exponent α also depends on the internuclear distance. In all previous applications of this model it was assumed that the threshold exponent is a constant equal to the value of α taken at the equilibrium internuclear distance. This approximation greatly simplifies the calculations, but its validity and accuracy has not been tested. In a recent paper by Horáček et al. [79], it was shown that the approximation of constant α is a very good approximation for HBr and HI molecules which possess weak dipole moments, but is not adequate for the calculation of VE cross sections of HCl.

In this section we show how the R-dependent α can be included into calculation and we elaborate a further improvement of the DM model which is necessary for the calculation of the AD cross section. While the overall magnitude of the VE and DA cross sections is not sensitive to the H-Cl^- potential-energy function at large internuclear distances, the magnitude of the AD cross section is largely determined by this part of the HCl^- potential. In the DM model the nonlocal potential-energy function at short and intermediate internuclear distances has been determined by fitting ab initio electron-HCl scattering data of Padial and Norcross [80]; the long-range part of the potential has been constructed by extrapolation [67]. In the meantime accurate ab initio calculations of the long-range part of the HCl^- $^2\Sigma^+$ potential-energy function have been reported by O'Neil at al. [81] and Åstrand and Karlström [77]. In the present work we make use of these data to construct an improved nonlocal resonance model for HCl which is suitable for the calculation of the AD cross section. It will be shown that this improvement of the DM model, together with the variable threshold exponent introduced by Horáček et al. [79], also leads to a significant improvement of the calculated VE and DA cross sections.

R-dependent threshold exponent

In the existing applications of the nonlocal resonance model to electron-HX collisions [67, 68, 32, 75], the discrete-continuum coupling matrix element has been taken to be of the form

$$V_{\mathrm{d}\epsilon}(R) = f(\epsilon)g(R). \tag{5.1}$$

The dependence of $V_{\mathrm{d}\epsilon}$ on energy is thus assumed to be the same for all internuclear distances, which is, of course, a rather restrictive assumption.

In the DM model, the function $f(\epsilon)$ has been represented by the analytic expression

$$f(\epsilon) = (2\pi)^{-\frac{1}{2}} A^{\frac{1}{2}} (\epsilon/B)^{\alpha/2} \mathrm{e}^{-\epsilon/2B}. \tag{5.2}$$

Here α is the threshold exponent evaluated from the dipole moment at the equilibrium distance R_0 of the target molecule. The parameter A determines the overall strength of the discrete-continuum coupling, and B is a high-energy cut-off parameter. For the function $g(R)$, various forms have been chosen [67, 32, 68]. The unknown parameters have been determined by fitting the scattering phaseshift in the fixed-nuclei *ab initio* calculations [67, 32].

In the present work we replace the DM ansatz (5.1,5.2) by the more general form

$$V_{d\epsilon}(R) = f(\epsilon, R)g(R) \tag{5.3}$$

$$f(\epsilon, R) = (2\pi)^{-\frac{1}{2}} A^{\frac{1}{2}} (\epsilon/B)^{\alpha(R)/2} \mathrm{e}^{-\epsilon\beta(R)/2B} \tag{5.4}$$

where $\alpha(R)$ and $\beta(R)$ can be arbitrary functions. The dependence of V_{dE} on energy is now an explicit function of the internuclear distance. The R-dependent threshold exponent $\alpha(R)$ is determined by the dipole moment function of the target molecule, which is well known for the hydrogen halides [82, 83]. The function $\beta(R)$ accounts for a dependence of the high-energy cut-off parameter on the internuclear distance. Since the aim of this work is to reveal the effect of the R-dependence of α, we have put $\beta(R) = 1$ in the calculations. We do not expect a large effect of this assumption on the cross sections near the threshold.

The nonlocal part of the effective potential for the nuclear motion in the resonant state is given by the following expression (compare with eq. 3.26)

$$f_J(E, R, R') = \sum_n \chi_{nJ}(R)g(R)[\delta(E - E_n, R, R') - \tfrac{i}{2}\gamma(E - E_n, R, R')]g(R')\chi_{nJ}(R') \tag{5.5}$$

where

$$\gamma(\epsilon, R, R') = A(\epsilon/B)^{(\alpha(R)+\alpha(R'))/2} \mathrm{e}^{-\epsilon(\beta(R)+\beta(R'))/2B} \tag{5.6}$$

and

$$\delta(\epsilon, R, R') = \tfrac{1}{2\pi}\mathcal{P}\int_0^\infty \mathrm{d}\epsilon' (\epsilon - \epsilon')^{-1} \gamma(\epsilon', R, R'). \tag{5.7}$$

Here $\chi_n(R)$ are the eigenstates of the target molecule and E_n their energies.

With the DM ansatz (5.1), the integral kernels $\delta(\epsilon, R, R')$ and $\gamma(\epsilon, R, R')$ are independent of R and R', which simplifies the calculations considerably. The main complication introduced by the more general ansatz (5.3) is the fact that the kernel $\delta(\epsilon, R, R')$ is not separable in R and R', see Eq. (5.7). We may expect, however, that for reasonably smooth functions $\alpha(R)$ and $\beta(R)$ a sufficiently accurate separable approximation exists. This approximation is the key for an efficient computational algorithm for the solution of the scattering problem with the nonlocal potential operator (5.5) since, as we know from the previous chapter, the nonseparability increases dramatically the time needed for the calculation.

Here we show that the kernel $\delta(\epsilon, R, R')$ can be approximated by the expression

$$\delta(\epsilon, R, R') \sim \sum_{k=1}^{N} B_k(\epsilon, R) B_k(\epsilon, R') \tag{5.8}$$

with a very small number N of separable terms. For the construction of this separable approximation we use the so-called Bateman expansion [84], widely used in nuclear physics.

The idea of the Bateman expansion is as follows: For the kernel $V(X, Y)$ of any nonlocal operator, a new kernel $V_1(X, Y)$ is defined as

$$V_1(X, Y) = V(X, Y) - \frac{V(X, Y_1)V(X_1, Y)}{V(X_1, Y_1)} \tag{5.9}$$

where X_1 and Y_1 are properly chosen points in the range of the potential V. Since for any X and Y

$$V_1(X, Y_1) = 0 \tag{5.10}$$

and

$$V_1(X_1, Y) = 0, \tag{5.11}$$

the first Bateman approximation, $B_1(X, Y)$,

$$V(X, Y) \sim B_1(X, Y) = \frac{V(X, Y_1)V(X_1, Y)}{V(X_1, Y_1)} \tag{5.12}$$

coincides with the exact nonseparable potential at two lines: $X = X_1$ and $Y = Y_1$. The second Bateman approximation is defined similarly as a sum of two terms

$$V(X, Y) \sim B_1(X, Y) + B_2(X, Y) \tag{5.13}$$

where

$$B_2(X, Y) = \frac{V_1(X, Y_2)V_1(X_2, Y)}{V_1(X_2, Y_2)} \tag{5.14}$$

which coincides with the original potential at the lines: $X = X_1, X = X_2, Y = Y_1$ and $Y = Y_2$. This procedure is repeated until the required accuracy is obtained. It should be stressed that the resultant approximation is a sum of terms which are separable in the variables R and R'. The energy dependence, which is crucial for the proper description of threshold effects, is treated exactly.

The Bateman technique requires the specification of the points X_1, X_2, etc. As a natural choice of the points X_1, Y_1 one may set $X_1 = Y_1 = R_0$, where R_0 is the equilibrium distance of the target molecule. It appears that the first Bateman approximation, $N = 1$, yields results correct to four significant figures not only for HI, for which the threshold exponent changes in the limits 0.468-0.5 for the R of interest, but also for HBr, which has a stronger dipole moment and for which the the threshold exponent changes over a broader range of values: 0.386-0.5. For HCl, with the strongest dipole moment, two terms were needed to approximate the potential to three significant digits. The choice of the second Bateman point in the case of HCl was not crucial; the quality of the approximation was found to be nearly independent of the choice of X_2, Y_2.

The Bateman expansion has been implemented into the code for the solution of the nuclear scattering problem with the Schwinger-Lanczos method described in the previous chapters. The amount of numerical work needed for calculations with R-dependent threshold exponent $\alpha(R)$ is somewhat higher than that required for constant α. Nevertheless, the calculations are still very fast and the cross sections can be determined to any desired accuracy. This modified DM model with α replaced with $\alpha(R)$ will henceforth be referred to as DMH model. Details of the model are described in the appendix B.

Long range H+Cl$^-$ interaction

A further improvement of the model is achieved by a modification of the long-range part of the negative-ion potential function. The functions $g(R)$, $f(\epsilon)$ and

$V_d(R)$ were obtained by Domcke and Mündel by fitting fixed-R *ab initio* electron-HCl scattering data for R ranging from 1.8 to 3 a.u. No information on the potential-energy function at larger internuclear distances has been used in this model. Several accurate *ab initio* studies of the bound part of the $^2\Sigma^+$ potential of HCl^- are now available in the literature [81, 77]. This makes it possible to further improve the DMH model.

To do so we define the potential $V_1(R)$ of the $^2\Sigma^+$ resonance and bound state of HCl^- as the eigenvalue[1] of the fixed nuclei Hamiltonian (2.23), which is given by the formula (3.28), i.e.

$$V_{\text{loc}}(R) = V_0(R) + E_{\text{Res}}(R), \tag{5.15}$$

where

$$E_{\text{Res}}(R) = V_d(R) - V_0(R) + \Delta(E_{\text{Res}}(R), R) \tag{5.16}$$

and the level shift $\Delta(E, R)$ is defined as

$$\Delta(E, R) = \tfrac{1}{2\pi}\mathrm{P}\int_0^\infty \frac{|V_{d\epsilon}(R)|^2}{E-\epsilon}d\epsilon. \tag{5.17}$$

If $E_{\text{Res}} < 0$, then $V_{\text{loc}}(R)$ represents the bound electronic state of HCl^-. This holds for $R > 2.8$ a. u. If $E_{\text{Res}} > 0$, then $V_{\text{loc}}(R)$ represents the $^2\Sigma^+$ shape resonance. The discrete-state potential $V_d(R)$ can now be expressed in terms of $V_1(R)$, $V_0(R)$ and $\Delta(E, R)$

$$V_d(R) = V_1(R) - \Delta(V_1(R) - V_0(R), R). \tag{5.18}$$

An improved model exhibiting the correct long-range behaviour of the HCl^- potential function can thus be constructed by modifying the function $V_d(R)$ while retaining the functions $V_0(R)$ and $V_{d\epsilon}(R)$. We used the *ab initio* data of O'Neil et al. [81] and of Åstrand and Karlström [77]. as an input for this procedure. A spline interpolation has been used to obtain $V_d(R)$ and the potential was smoothly matched to the polarization potential $-2.25/R^4$ (a. u.) at large R. The original form of $V_d(R)$ has been used for $R < 2.8$ a. u. where it has been previously determined from *ab initio* fixed-R electron-molecule scattering data [67].

Finally, for computational convenience, we have replaced the spline interpolation of $V_d(R)$ by a simple analytic formula. To remove the kink in the function $g(R)$ Eq. (B.14) at $R = R_1$, we modified the function $g(R)$ to render it smooth at $R = R_1$. For a detailed description of these technical aspects we refer to the Appendix B.

In the following the models resulting from the long-range *ab initio* data of O'Neil et al. and Åstrand and Karlström will be referred to as DMHC-1 and DMHC-2 models, respectively. The potential function $V_0(R)$ and the functions $V_1(R)$ of the DM, DMHC-1 and DMHC-2 models are shown in the Figure 5.1 together with the ab initio data.

The DMHC-2 model is considered as the definitive model, since the Åstrand and Karlström data are judged to be more accurate than the O'Neil data. In the following we report also the results for the DM, DMH and DMHC-1 models, to indicate the sensitivity of the cross sections to details of the model.

[1] More rigorously the quantity definded below gives the pole of K-matrix which in case of its existence coincides with eigenvalue.

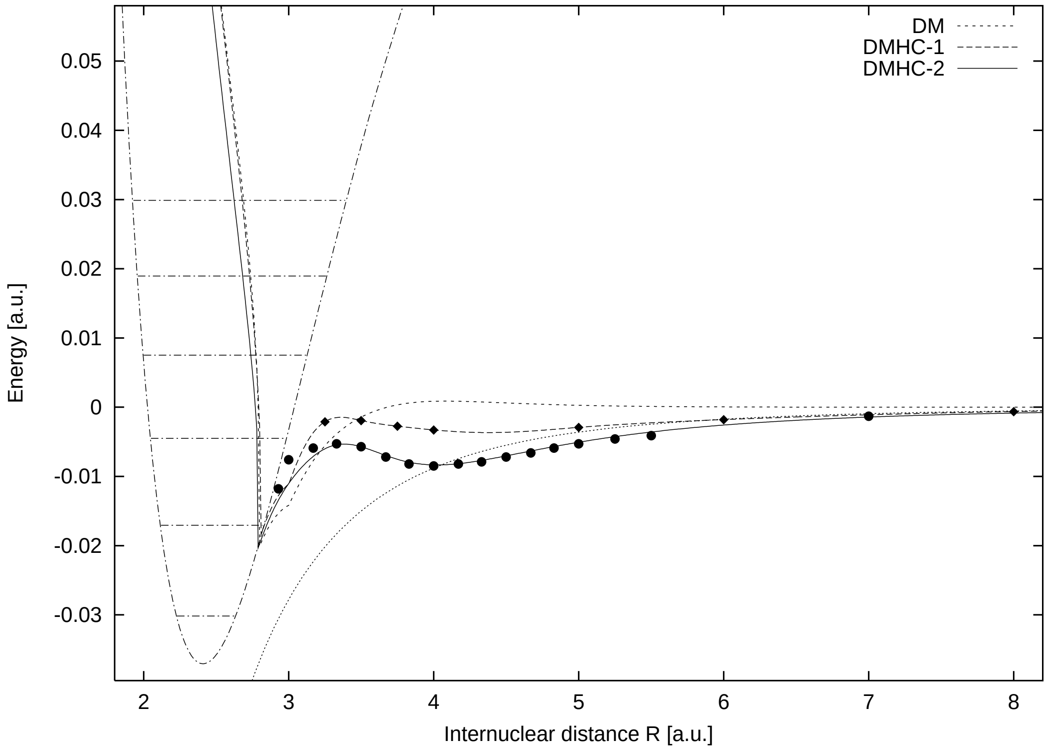

Figure 5.1: Potential-energy function $V_0(R)$ of the $X^1\Sigma$ state of HCl (dashed-dotted curve, bound states indicated), potential-energy function $V_1(R)$ of the $^2\Sigma$ state of HCl^- in the DM (short dashes), DMHC-1 (long dashes) and DMHC-2 (full curve) models. The dotted line shows the long-range polarization potential. Ab initio data of Åstrand and Karlström [77] and O'Neil et al. [81] are indicated by full circles and diamonds, respectively.

Calculation of cross sections

Angular momentum of the released electron has been neglected in our treatment see the section 2.4. This approximation is not necessarily fulfilled in the presence of the dipole potential and we intend to test it in the future. Nevertheless the results for angularly averaged quantities should be reproduced at least in qualitatively good agreement with experiments. Lippmann-Schwinger equations (2.55) and (2.79) with the nonlocal potential (2.73) are solved using the Schwinger-Lanczos method as described in the Chapter 3. For the treatment of the nonseparable coupling matrix element $V_{d\epsilon}(R)$ due to the variable threshold exponent $\alpha(R)$ we use the Bateman technique of the second order.

Dissociative attachment

Calculations of the DA cross section for HCl have been reported by several authors, see, e.g. [64, 73, 67, 69, 70, 71, 68]. The majority of the calculations provides a qualitatively correct description of the observed features, i.e., an essentially vertical onset at threshold, step-like Wigner cusps at the openings of the VE channels, and a rapid increase of the cross section with increasing rovibrational energy of the target. It has been noted that the DA cross section for $n = 0, J = 0$ is generally less sensitive to details of the potential-energy functions than the VE cross sections [67, 69, 68]. The existing calculations taking full account of the nonlocality of the problem have been performed without inclusion of the rotational degrees of freedom ($J = 0$) [67, 71, 68, 85].

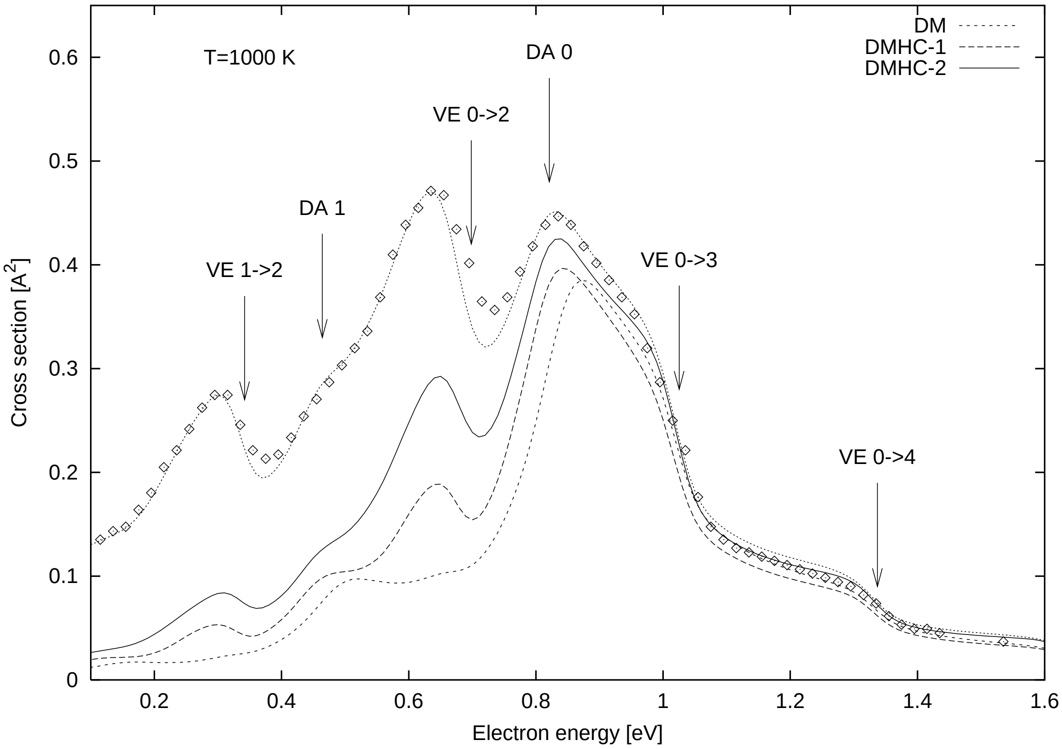

Figure 5.2: Cross section for dissociative attachment in HCl gas with temperature $T = 1000$K. Diamonds are experimental values shifted by +35meV (see text) and normalized to the maximum of the dotted curve. The dots are the results of the DMHC-2 model for a temperature of 1230 K. Theoretical results are convoluted with Gaussian distribution of width $50\,meV$ FWHM. The full, long-dashed, and short-dashed curves are the results of the DMHC-2, DMHC-1 and DM models at $T = 1000$K, respectively. Vibrational excitation thresholds and the thresholds for the dissociative attachment to ground (DA0) and the first vibrationally excited (DA1) states are indicated by arrows.

Since in the real experiments the target gas is at nonzero temperature T, the target molecules may be excited either rotationally or vibrationally. To describe this situation we have calculated the DA cross sections for target molecules in their four lowest vibrational states and for angular momenta $J = 0, \ldots, 30$ and then averaged the results over the Maxwell-Boltzmann distribution of the target states. The averaged cross section for the temperature T=1000 K is shown in Figure 5.2 together with the experimental data of Allan and Wong [8]. To compare our results with the experimental data we convoluted the theoretical data with a

Gaussian distribution with the full width at half maximum (FWHM) equal to the energy spread of the electrons in the experiment (50 meV). Moreover, since Allan and Wong give the uncertainty of their energy scale as ±40 meV, we have also shifted the experimental data to higher energies by 35 meV. In this way the positions of the calculated cross section peaks and cusps agree perfectly with the measured data.

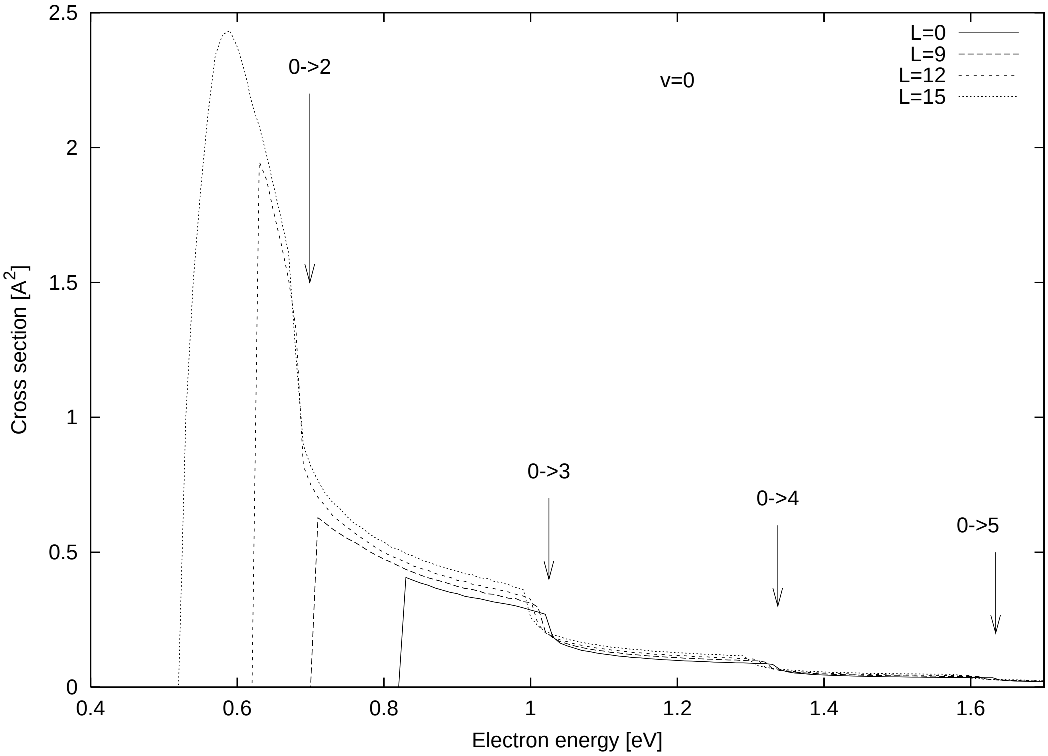

Figure 5.3: Dependence of the $\nu = 0$ dissociative attachment cross section on the initial rotational state of the HCl molecule for the DMHC-2 model. Thresholds for vibrational excitation processes are indicated by arrows.

Let us first discuss the theoretical results for the different models. The influence of the long-range part of the potential is seen in the difference among the DM, DMHC-1 and DMHC-2 models. The more attractive the interaction, the larger the cross section for DA at low-collision energies. The cross section exhibits two dominant features: peaks for electron energy below 1eV and step-like structures above this energy. The steps known as Wigner cusps are related to the opening of the $0 \to 3$ and $0 \to 4$ vibrational excitation channels. The highest peak originates from molecules in their ground vibrational state ($n = 0$) and small angular momentum J; it is situated close to the threshold for dissociative attachment to molecules in the ground state. The second peak is due to HCl molecules in $n = 0$ and $J \sim 15$ states and it appears just below the threshold for $0 \to 2$ vibrational excitation. Its origin is clearly understood if we look at Figure 5.3, where the cross sections for attachment to HCl molecules with $n = 0$ and several J are shown (DMHC-2 model). The cross sections for $J > 10$ exhibit high peaks near the threshold which are suppressed in the thermal average by the Maxwell-Boltzmann factor $(2J+1)\exp(-(E_J^n - E_0^0)/kT)$, which is decreasing with J for $J > 10$. It is also clear from Figure 5.3 how is the peak related to the Wigner cusp at the $0 \to 2$ VE threshold. Contributions from HCl molecules in the $n = 1$ state are also seen in the cross section as a shoulder at the $(n = 1, J \sim 0)$ DA threshold and as a peak below the $1 \to 2$ VE threshold in Figure 5.2.

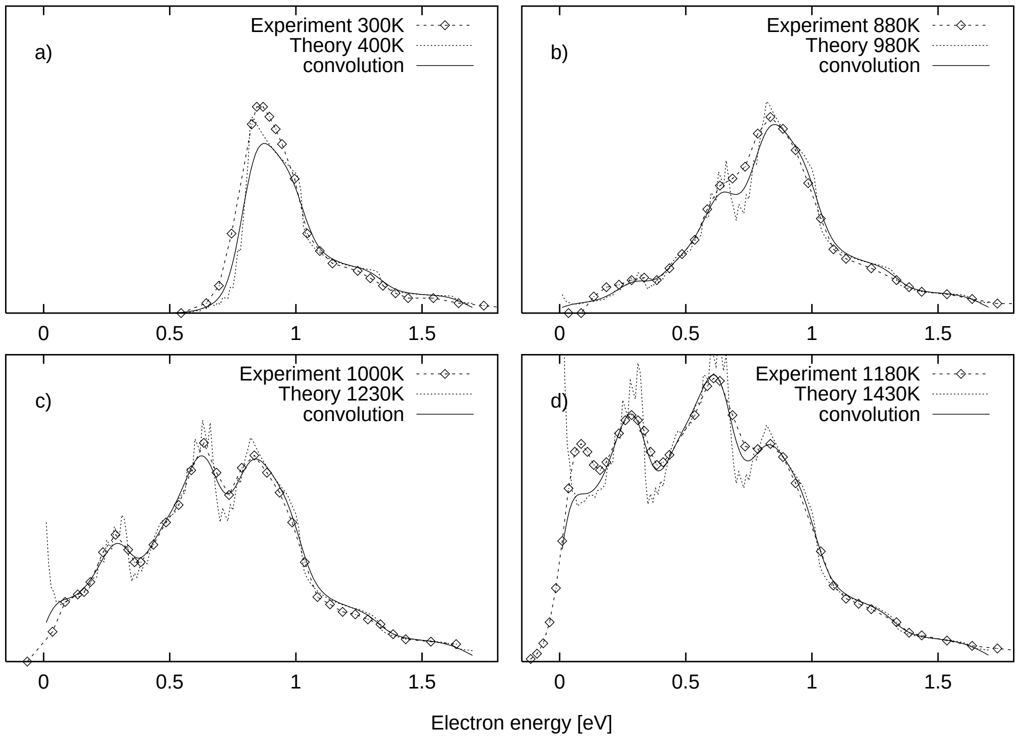

Figure 5.4: Comparison of the theoretical dissociative attachment cross section with the experimental data of Allan and Wong [8]. The theoretical results are convoluted with a Gaussian of 100 meV FWHM. The experimental data are shifted to higher energies by 35 meV. The temperature yielding the closest agreement with experiment is chosen in the calculation (DMHC-2 model).

Comparing the theoretical data with the experiment of Allan and Wong, we see that the position of the structures agrees quite well (accepting the shift, see above) but their relative height differs significantly. It is worth to point out that almost perfect agreement between theory and the measured data may be obtained by assuming a higher temperature of the target gas. This is demonstrated in Figure 5.2. If, for example, the cross section calculated at the temperature T=1230 K is compared with the data measured at T=1000 K we observe perfect agreement. The same holds also for other temperatures as indicated in Figure 5.4. Since very good agreement between theory and experiment can be obtained in all cases, we conjecture that a systematic error in the measurement of the temperature in the experiment of Allan and Wong may be responsible for the discrepancies between theory and experiment. The temperatures given by Allan and Wong appear to be systematically too low by 10-30%.

Vibrational excitation

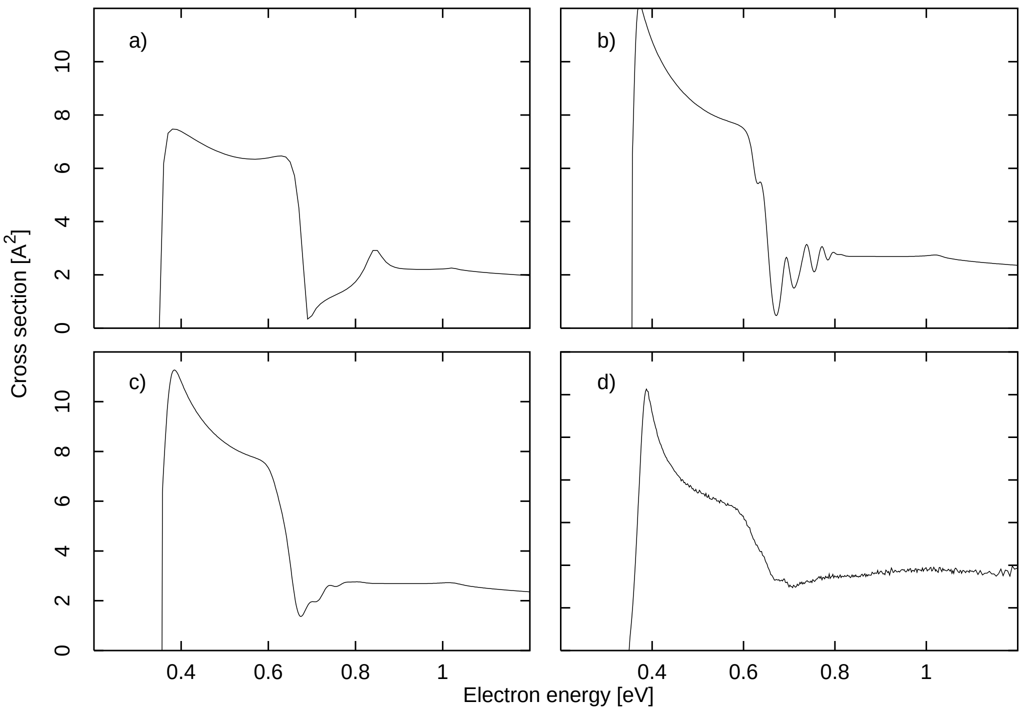

Figure 5.5: a) The $0 \to 1$ VE cross section calculated with the DM model.
b) The $0 \to 1$ VE cross section calculated with the DMHC-2 model, convoluted with a Gaussian of 10 meV.
c) The same as (b), convoluted with 20 meV.
d) The $0 \to 1$ VE cross section as measured by Schafer and Allan [11].

Let us proceed to the discussion of the vibrational excitation process. Previous calculations [67, 71, 68] have described qualitatively the observed features, i.e., the threshold peaks and the broad resonance region, but the detailed shapes of the cross sections were not reproduced correctly. Here we demonstrate that for energies close to the threshold the modifications of the original DM model proposed in this paper improve the agreement between theory and experiment to such an extent that not only the gross features, but also very minute details of the calculated cross sections can be compared with the measured data.

It has been shown in [79] that taking the variation of α with R into account changes the cross section near threshold significantly for molecules with larger dipole moments (HCl), but has only a marginal effect for molecules with small dipole moments (HBr and HI). The agreement between theory and experiment is further improved when the long-range behaviour of the HCl^- potential function is corrected according to *ab initio* calculations. The effect of both modifications

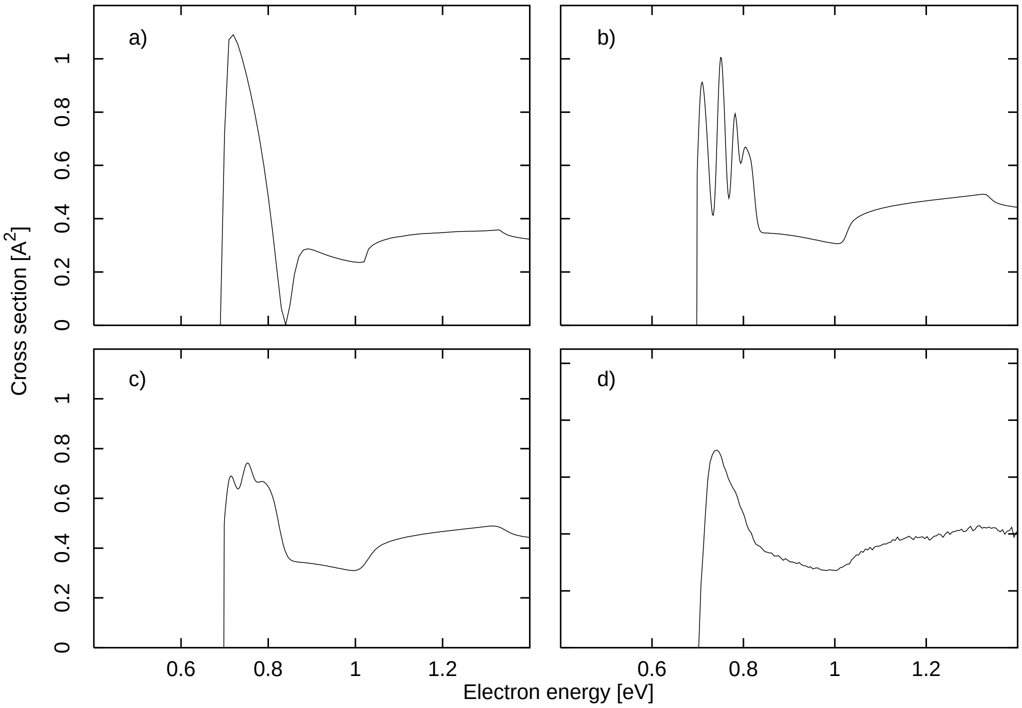

Figure 5.6: a) The $0 \to 2$ VE cross section calculated with the DM model.
b) The $0 \to 2$ VE cross section calculated with the DMHC-2 model, convoluted with a Gaussian of 15 meV.
c) The same as (b), convoluted with 25 meV.
d) The $0 \to 2$ VE cross section as measured by Schafer and Allan [11].

is shown in Figures 5.5a–d, where the $0 \to 1$ VE cross section for HCl is plotted. The cross section obtained with the DM model is shown in Figure 5.5a; the cross section in Figures 5.5b and 5.5c has been obtained with the DMHC-2 model, incorporating the R dependence of the threshold exponent and the long-range ab initio data of Åstrand and Karlström. For better comparison with experiment the data in Figure 5.5b were convoluted with a Gaussian of 10 meV width and the data in Figure 5.5c with a Gaussian of 20 meV width. Finally, in Figure 5.5d, the experimental cross section of Schafer and Allan [11] is plotted. The same cross sections for the $0 \to 2$ transition are shown in Figures 5.6a–d. The results demonstrate the dramatic improvement in the shape and fine structure of the cross sections obtained by incorporation of the R-dependence of α and by correcting the long-range part of the HCl^- potential-energy function.

Let us now discuss in more detail the effect of the long-range part of the H + Cl^- interaction. Plots of non-convoluted $0 \to 1$ and $0 \to 2$ VE cross sections in the threshold region are shown in Figure 5.7a and 5.7b. The effect of the long-range part of the interaction manifests itself most strongly for energies below the threshold of the DA channel. Both models, DMHC-1 and DMHC-2, predict oscillatory structures in an energy range which extends from the bottom of the

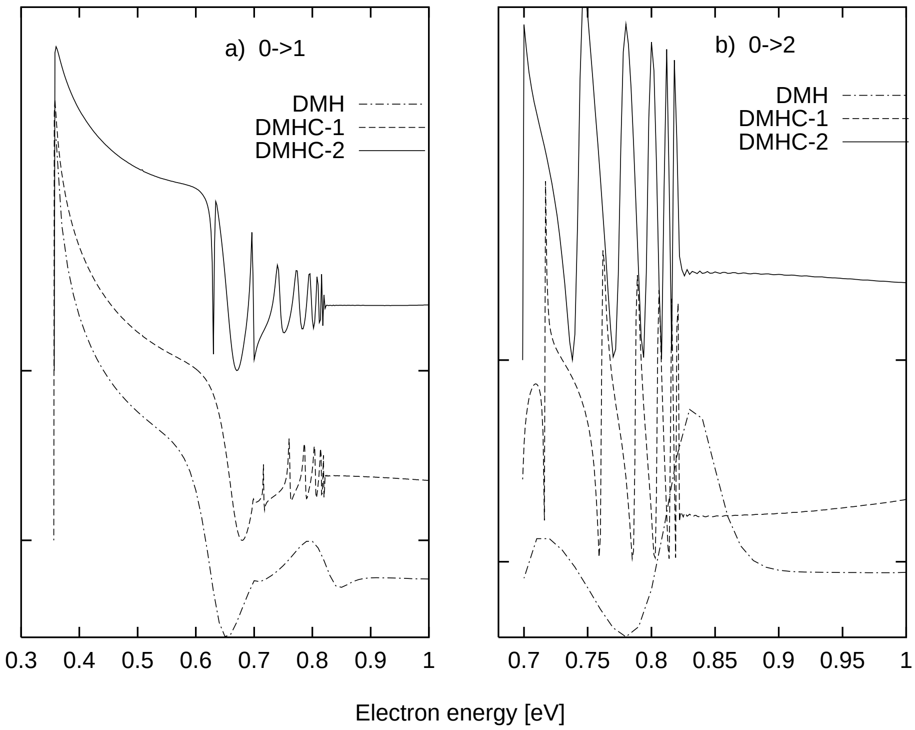

Figure 5.7: $0 \to 1$ and $0 \to 2$ vibrational excitation cross sections near threshold. The results of the DMH, DMHC-1 and DMHC-2 models are shown, reflecting the influence of the long-range part of the HCl^- potential function (the curves are shifted vertically not to overlap too much).

respective potential curve $V_1(R)$ to the DA threshold. The oscillations reflect interference with quasi-bound levels supported by the attractive well at intermediate internuclear distances (cf. Fig. 5.1). Such oscillations have been predicted also by some other HCl models [68] and observed experimentally [12, 11]. The DMHC-2 model constructed from the most sophisticated *ab initio* data predicts oscillations very similar to those seen in the high resolution experiments of Schafer and Allan [11] and Cvejanović [12] which are plotted in the Figure 5.8 together with convoluted DMHC-2 data. The positions of the calculated oscillations are somewhat shifted (10–20 meV) with respect to experiment, but the overall shape is in good agreement when the finite resolution and the contribution from several J (temperature 300K) in the experiment are taken into account.

The $0 \to \nu$ ($\nu = 0, 1, \ldots, 5$) cross sections[1] for electron energies up to 4 eV are shown in the Figure 5.9 together with the (non-normalized) experimental data of Schafer and Allan [11]. Unlike the DA and AD data (at most 10% difference) the VE cross sections for energies above the DA threshold turn out to be strongly dependent on tiny differences of the models. The shape of the experimental cross sections is quite well reproduced and, except of $0 \to 1$ cross section, the difference

[1]Cross sections for $\nu_1 \to \nu_2$, $\nu_1, \nu_2 = 0, 1, \ldots, 4$ transitions can be obtained on request from the authors.

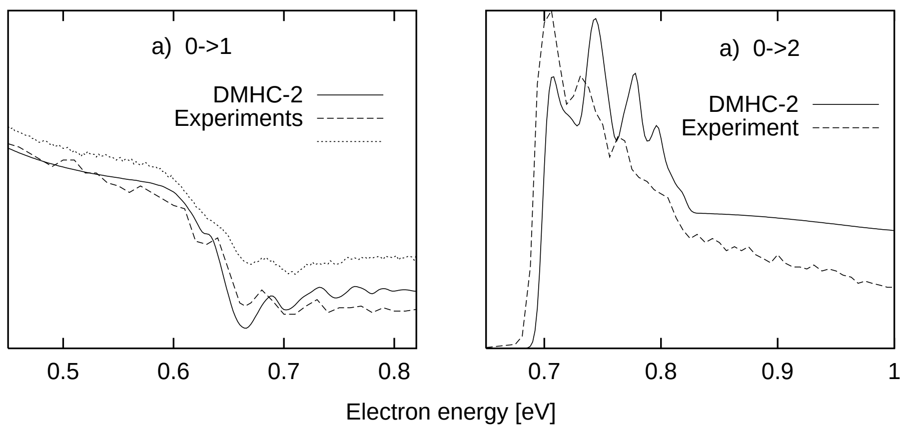

Figure 5.8: Comparison of the calculated near-threshold $0 \rightarrow 1$ and $0 \rightarrow 2$ vibrational excitation cross sections (DMHC-2 model) with the high-resolution measurements of Schafer and Allan [11] (dots) and Cvejanović [12] (dashes). The theoretical data are thermally averaged (T=300 K) and convoluted with a Gaussian of 30 meV FWHM.

between theory and experiment is within the uncertainty given by the difference between the DMHC-1 and DMHC-2 models.

Conclusions

We have constructed an improved nonlocal resonance model for electron-HCl collisions and have performed calculations of VE and DA cross sections. It can be summarized that the cross sections calculated with the new DMHC-2 model are in much better agreement with the experimental data for all processes considered here (DA and VE) than any other calculation published so far. The generalization and improvement of the nonlocal resonance model proposed in this paper leads to a good agreement between theory and experiment in the low-energy range. For VE at higher energies further improvements of the model may be required. New experiments would be valuable in which the dependence of DA cross section on the internal state of HCl is measured directly. These cross sections are closely related to the distribution of HCl states after associative detachment, which can be determined by measuring the energy spectrum of the released electrons (see the next section).

Further improvements of the model within the scope of the resonance formalism are possible:

- We have seen that the VE cross sections are quite sensitive to the precise form of $V_{d\epsilon}(R)$. Direct *ab initio* calculation of $V_d(R)$ and $V_{d\epsilon}(R)$ would be useful.

- Recent measurements of the Kaiserslautern group [86, 87, 88] indicate that higher partial waves may contribute to e^-+HCl scattering. Our treatment

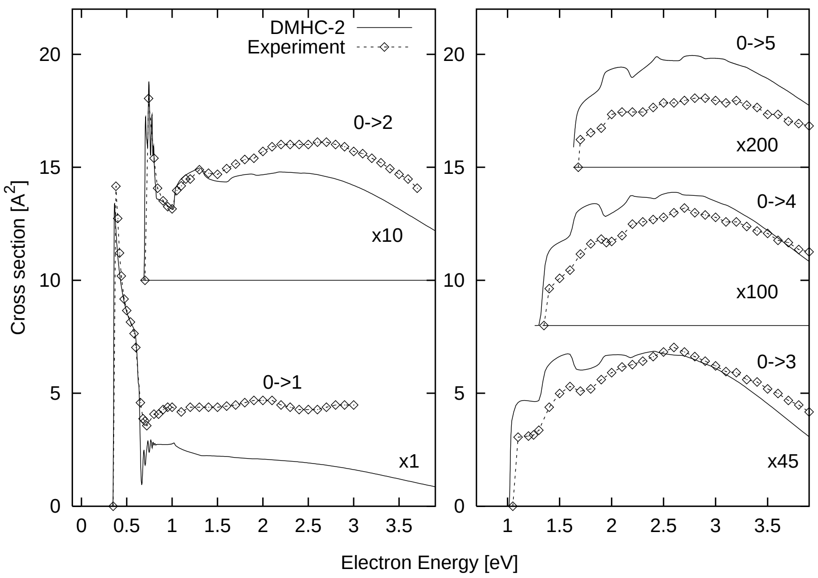

Figure 5.9: Comparison of the calculated vibrational excitation cross sections with the experimental data of Schafer and Allan [11]. The data are scaled (see labels). The overall normalization of the experimental data is chosen to give agreement with theory for the $0 \to 2$ cross section near 1eV.

ignores the angular momentum of the electron, which is equivalent to the assumption that only the s-wave contributes to $|\varphi_\epsilon\rangle$. It is not difficult to incorporate angular momentum transfer into our model (see [89]) but additional information about the partial-wave components of $V_{d\epsilon}(R)$ is necessary [22].

5.2 Associative detachment in Cl^-+H collisions

A calculation of the AD cross section in low-energy H + Cl^- collisions based on a zero-range-potential model has been reported by Gauyacq [76]. The parameters of the model were adjusted to reproduce the available experimental data. The present work represents the first treatment of the H + Cl^- AD process in the nonlocal complex-potential formalism and we perform the calculation with an ab-initio-based model which contains no parameters adjusted to experimental data (except spectroscopic data of the neutral ground state of HCl, which are also available from accurate *ab initio* calculations [82]). We use the model described in the previous section, i. e. we employ one and the same model to calculate the cross sections for all channels (VE, DA and AD). The calculation of AD is computationally considerably more demanding than calculations for the inverse process of DA. While only few partial waves are involved in the process of dissociative attachment of an electron to cold molecules, many partial waves have to be taken into account to obtain a converged cross section for the AD process. Convergence of the partial-wave sum for the AD cross section for a collision energy 1eV requires the inclusion of angular momenta up to $J_{\max} = 38$ (it is less/more for lower/higher energies respectively). It should also be stressed that the local-complex-potential approximation is inapplicable for low-energy H + Cl^- collisions owing to the threshold singularities caused by the dipole potential in the electron-scattering channel [4]. In contrast to the H + H^- collision, where the local-complex-potential approximation is of quantitative accuracy for the AD process [89], a nonlocal treatment is indispensable for the H+ Cl^- AD process.

Total AD cross section

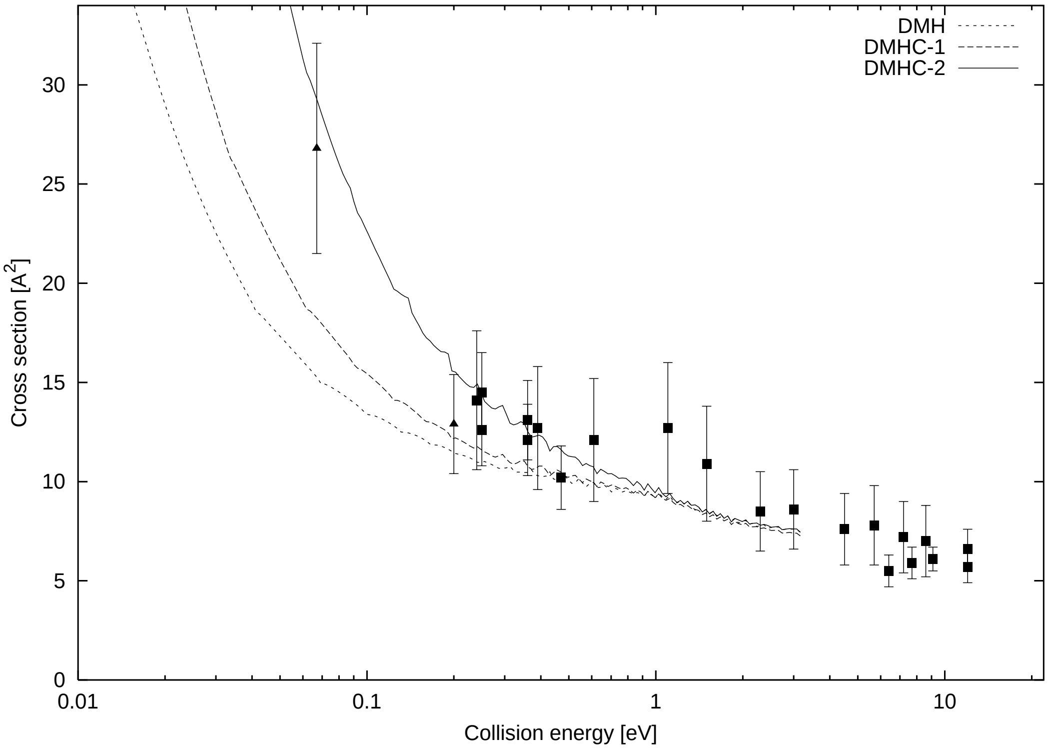

Figure 5.10: The total associative detachment cross section obtained with the DMH (short dashes), DMHC-1 (long dashes) and DMHC-2 models (full curve), respectively. Experimental data (squares) and data derived from experimental rates (triangles) are taken from Huels et al. [1].

The total AD cross sections obtained with the DM, DMHC-1 and DMHC-2 models are shown in the Figure 5.10 together with the experimental data [1]. At collision energies above 1 eV all three models yield the same cross section. At low energies (below 100 meV) only the DMHC-2 model yields an AD cross section which is consistent with the cross section inferred from the rate coefficients of Fehsenfeld et al. [90]. The significant deviation of the DMHC-1 cross section from the DMHC-2 cross section and experiment at low energies reflects the fact that the potential of O'Neil et al. is not sufficiently attractive at large and intermediate distances (cf. Fig. 5.1). It can be concluded that only the HCl^- potential-energy function of Åstrand and Karlström is compatible with the measured low-energy H + Cl^- AD cross section.

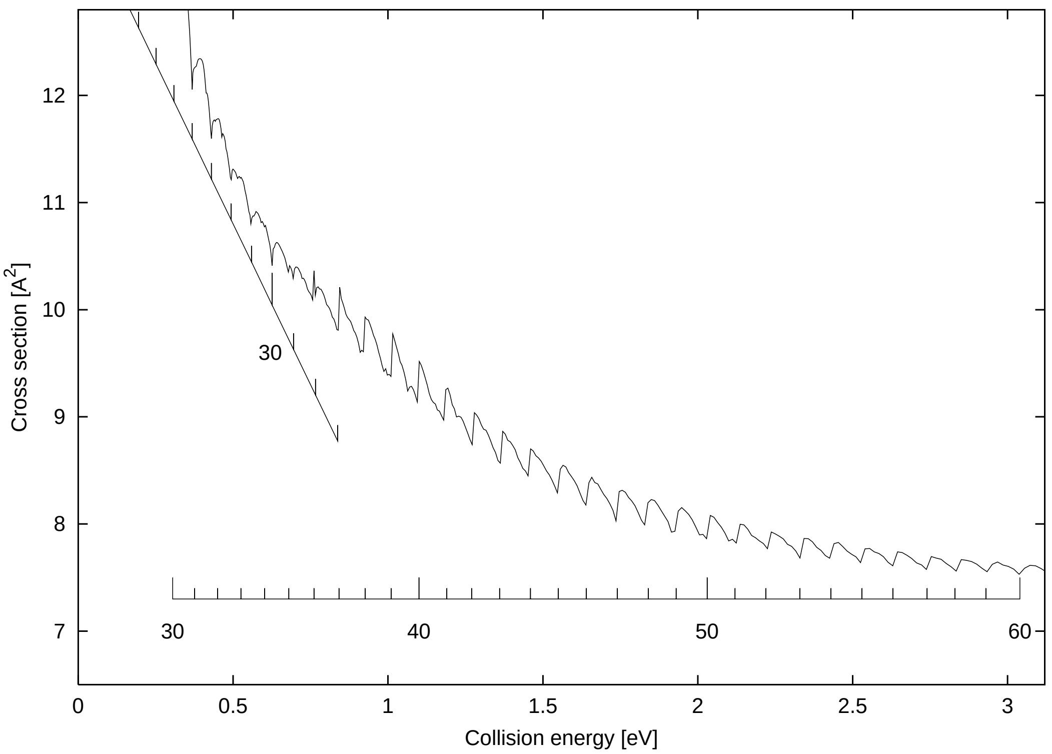

Figure 5.11: The details of the threshold structures in the associative detachment cross section obtained with the DMHC-2 model. Thresholds for the production of HCl in ground (bottom) and first excited vibrational states are indicated. The numbers give the angular momentum of the molecule in the final state.

The AD cross section exhibits an extended series of threshold peaks, each at the opening of a ro-vibrational channel of the HCl molecule. Detailed plots of the threshold peaks in the AD cross section obtained with the DMHC-2 model are shown in Fig. 5.11. For higher E only the thresholds with $\nu = 0$ and $l \sim 50$ are discernible. For $E < 1.3$eV, the structure becomes more complicated because of the appearance of thresholds with $\nu > 0$. More insight into the details of the dynamics and the origin of those structures can be gained from the distribution of the final states and the electron spectra.

State distribution of final HCl molecule

The total AD cross section in the Figure 5.10 is the sum of the individual cross sections with certain final state of the formed HCl molecule. The cross sections for the final HCl formed in the ground vibrational state and with angular momentum $J = 0, 1, \ldots, 32$ are shown in the Figure 5.12. For each J we see a slow decrease of the cross section, which is of purely kinematic origin. For larger J

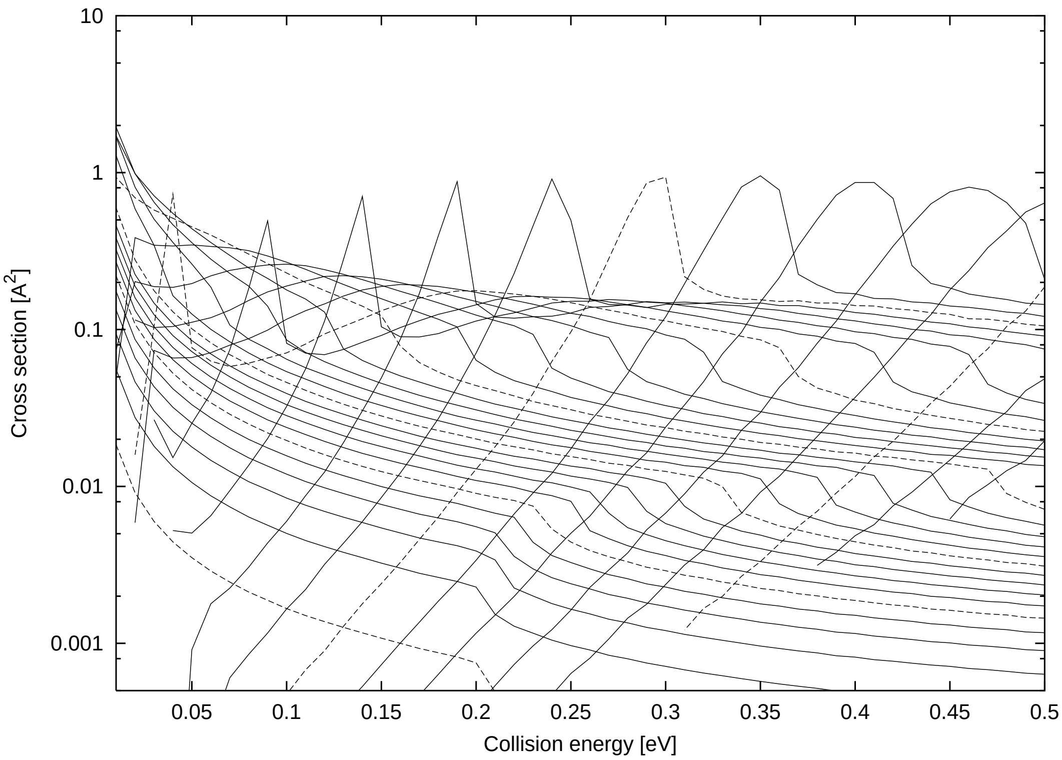

Figure 5.12: AD cross sections for final HCl molecule in ground vibrational state and with $J = 0, 1, ..., 32$. The dashed lines correspond to (from bottom to top) $J = 0, 5, 10, ..., 30$.

cross section first increases which is connected with tunneling through centrifugal barrier (effective potential is shown in the Figure 5.13). Superposed on this behavior are sharp steps (or cusps) which are caused by opening of $n = 1(2, 3)$ channels for given J. These steps are the Wigner cusps in AD cross section and they can not be described correctly within local complex potential model. To demonstrate the step behavior caused by redistribution of the flux into newly open channels we show the Figure 5.14 with cross sections for AD with final HCl in ($n = 0, \ldots, 5, J = 23$) states. This Figure clearly demonstrates that step-like decrease of one channel corresponds to opening of another one.

To get further insight into the physics of the process we define the impact parameter

$$b = J/p = J/\sqrt{2\mu E} \tag{5.19}$$

for each angular momentum J and collisional energy E and the quantities

$$w_{n_f}(b) \equiv \frac{2\mu E}{\pi(2J+1)}\sigma(n_f, J_f) \tag{5.20}$$

$$w(b) \equiv \sum_{n_f} w_{n_f}(b). \tag{5.21}$$

The normalization factor in (5.20) is chosen in such a way, that w corresponds to the classical probability that AD occurs for a given trajectory (determined

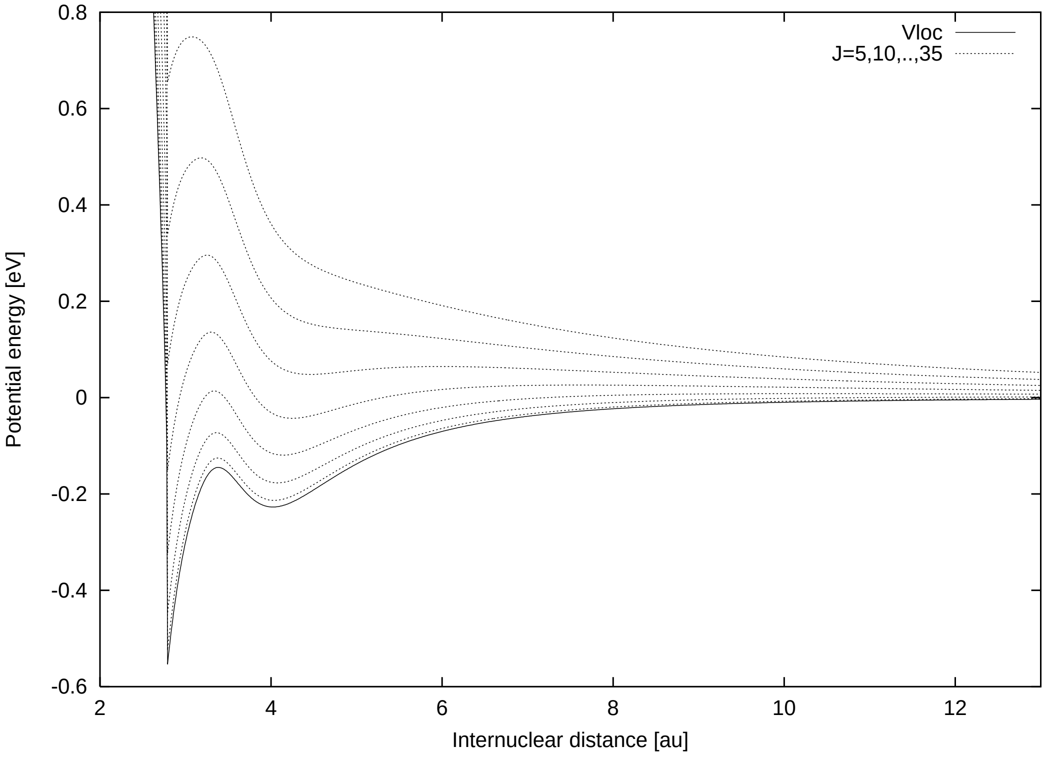

Figure 5.13: Effective local potential $V_{loc} + J(J+1)/2\mu R^2$ for HCl.

by a given b). We can see this if we write classical cross section $\sigma_{\rm class}(J)$ for a given process to occur at impact parameters between $b_1 = J/\sqrt{2\mu E}$ and $b_2 = (J+1)/\sqrt{2\mu E}$

$$\sigma_{\rm class}(J) = \int_{b_1}^{b_2} 2\pi b\, w_{\rm class}(b)\,{\rm d}b \simeq \pi(b_2^2 - b_1^2) w_{\rm class}(b_1) = \frac{\pi(2J+1)}{2\mu E}\, w_{\rm class}(b_1). \tag{5.22}$$

The quantity (5.20) thus gives the possibility to compare the results of fully quantum-mechanical calculation with our classical intuition. The plot of w_{n_f} versus b is shown in the Figure 5.15 for two collision energies $E = 30\,$meV ($\sim$ room temperature collisions) and $E = 300\,$meV. The function $w(b)$ generally follows the behavior which we would expect. The probability for the detachment is almost 1 if the particles come close enough and for large b $w(b) \to 0$ which means that the particles fly too far apart for the detachment to occur (or the centrifugal barrier becomes too large for particles to penetrate it—in radial description). For obvious kinematic reasons the impact parameter, for which the probability vanish decreases with increasing collision energy (typical behavior for an attractive potential). Wigner cusp is seen at each b for which one of the channels closes. Interesting feature is the dip in the total probability $w(b)$ at such energies. We have a following interpretation for such a behavior. If the collision energy is far from any threshold, than the electron which can be released in the collision must be fast and it escapes easily. On the other hand, for the energies close to a threshold, the electron energy can be small and escaping electron can be pushed

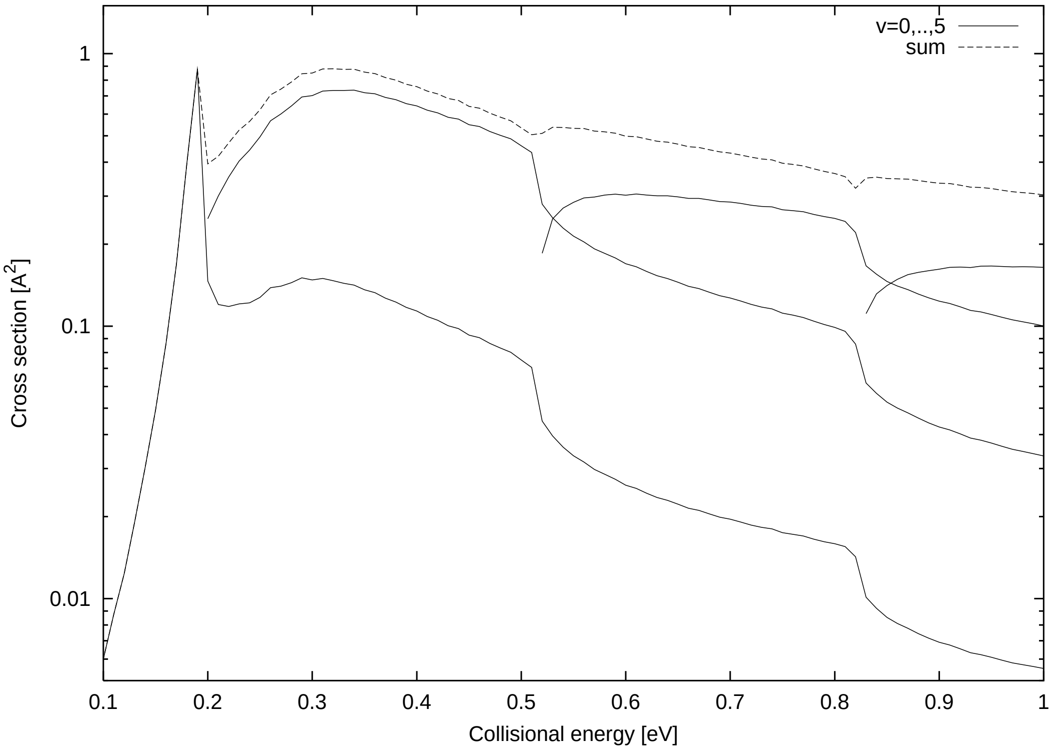

Figure 5.14: AD cross sections for final HCl molecule in several different vibrational states $n = 0, 1, ..., 5$ and J=23.

back towards colliding nuclei species by long range dipole force and reabsorbed again. This process takes some time and the motion of the nuclei moving in the meantime on the potential curve $V_0(R)$ can be reversed. The negative ion thus have a larger chance to escape without detachment. Note that for a more detailed study of such a behavior the time-dependent formulation of the problem must be used. Such calculations have been done for electron scattering on HCl and H_2 before [91, 41, 68] and the time-dependent approach should be applicable also to AD.

Electron spectra

It is useful to look at the Figure 5.16 first before looking at the electron spectra. Energies of all bound states of the HCl molecule are shown there. Asymptotic energy of H+Cl$^-$ is chosen as zero. If we draw the line showing the collision energy into the plot than the difference between the line and each state gives the energy $\epsilon_n^J = E - E_n^J$ of the released electron. The spectrum is given by

$$\frac{\mathrm{d}\sigma}{\mathrm{d}\epsilon}(E, \epsilon) = (2J+1) \sum_{nJ} \sigma_n^J(E) \delta(\epsilon - \epsilon_n^J), \tag{5.23}$$

where $\sigma_n^J(E)$ is the cross section calculated according to (2.75). We show the results of our calculated spectrum schematically for two collision energies $E =$

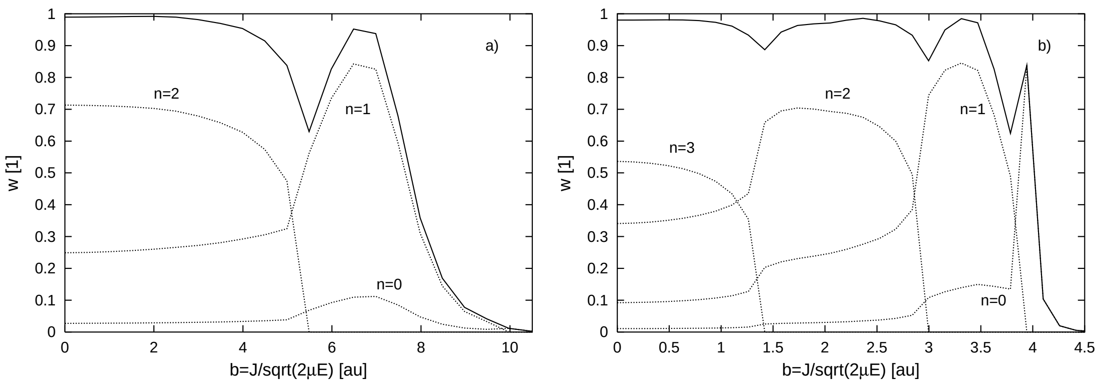

Figure 5.15: Probabilities for the detachment into different final states; dependence on "impact parameter" $b = J/\sqrt{2\mu E}$. The collision energy is 30 meV for the Figure a) and 300 meV for the Figure b).

30 meV and $E = 300$ meV in Figure 5.17. We can see three well separated "bands" in the spectrum for $E = 30$ meV corresponding to $n = 0, 1$ and 2. Wigner cusps for J at which the $n = 2$ channel closes (J=10) are well distinguishable in both $n = 1$ and $n = 2$ bands. Behavior for small J is described with the kinematic factor $(2J + 1)$ and the cut off for large J is given by the penetration through centrifugal barrier (also shown in the Figure 5.16). Features which are sensitive to the nonlocality of the dynamics are the shape of the Wigner cusps and the ratio among the "bands" for different n. The "bands" in the spectrum for $E = 300$ meV strongly overlap, since more J ($J < 30$) contribute to the cross section. Otherwise the structure of the spectrum is very similar to the previous case. We would also like to point out that the cusps occur for approximately the same energies ($\epsilon \sim 0.35$ and $\epsilon \sim 0.7$eV) in all "bands" and for all collision energies. This feature is due to fairly constant separation $\Delta E = E^J_{n+1} - E^J_n$ of neighbouring levels over a large interval of J and it is important for experiments since collision energy is not well determined there and we have a broad distribution of collision energies instead.

Experimental set-up, which is planned in Kaiserslautern consist of atomic-hydrogen-source, ion-source and vacuum chamber, where the collision takes place. Atomic hydrogen is driven by tube to the reaction chamber where the beam is formed by the hydrogen escaping through a small hole. The ion beam accelerated in electrostatic field crosses the hydrogen beam under certain angle α. Electron spectrometer is situated in the collision plane, near the reaction region and its angle relative to both beams can be varied. Collision energy distribution for the ion-atom collisions is determined by the following factors

- the angle α between the beams,
- (angular) divergence of the beams (mainly atom beam),
- temperature of the atom gas,
- laboratory energy distribution of the ion beam.

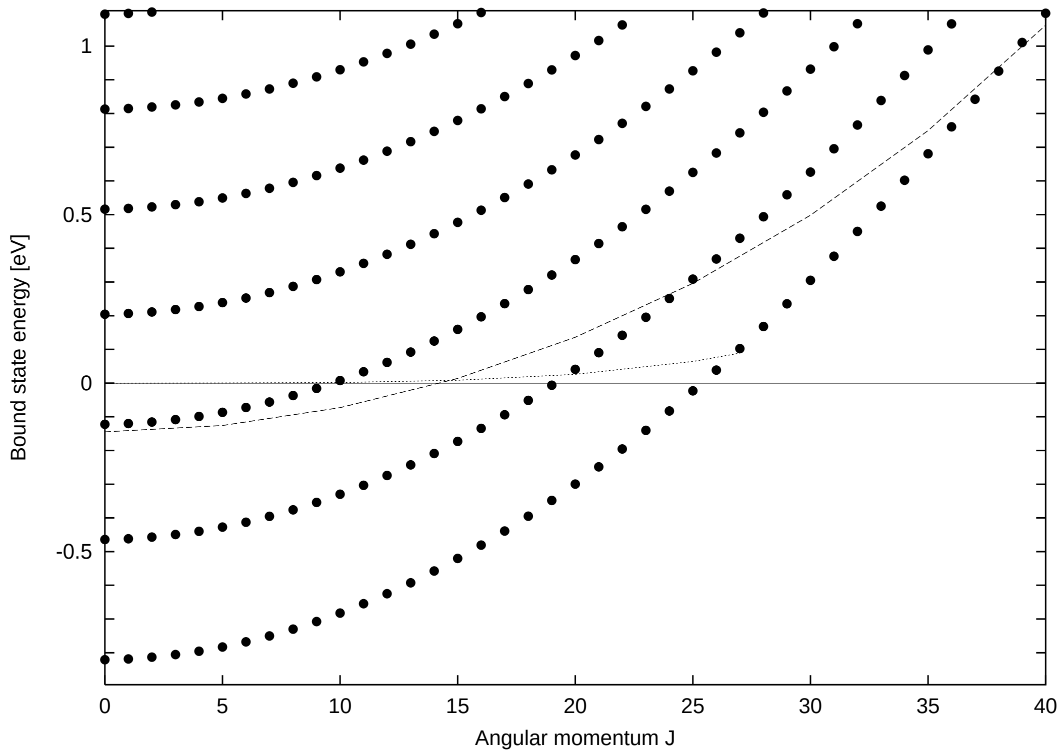

Figure 5.16: Energies of bound states of the HCl molecule versus rotational quantum number J. The dashed line shows the height of the barrier at $R \simeq 3.5$ for different J and the dotted line indicates the height of the barrier due to long range polarization force $\sim R^{-4}$ plus rotational term $\sim R^{-2}$.

The distributions have been simulated in the experimental group [92] for realistic estimates of the factors in possible experiments. We used the simulated collision energy distribution $\phi(E)$ for more realistic prediction of the electron spectra which are to be expected in the planned experiments. The spectrum (5.23) has to be convoluted with the distribution in the following way

$$\left(\frac{\mathrm{d}\sigma}{\mathrm{d}\epsilon}\right)_{\mathrm{exp}} = \int_0^\infty \phi(E)\,\frac{\mathrm{d}\sigma}{\mathrm{d}\epsilon}(E,\epsilon)\,\mathrm{d}E = \sum_{nJ}(2J+1)\phi(\epsilon+E_n^J)\,\sigma_n^J(\epsilon+E_n^J). \quad (5.24)$$

The convoluted spectrum is thus sum of peaks shaped like $\phi(E)$ (if the cross section σ_n^J does not vary too fast within the width of the distribution $\phi(E)$). The convoluted spectra are shown in the Figure 5.18 together with the distribution $\phi(E)$ for two different sets of experimental parameters. The narrower distribution corresponds to $\alpha = 40^0$ and the temperature of atomic hydrogen 300K and the wider to $\alpha = 60^0$ and the temperature 100K. We can see that the peaks are almost lost for the wider distribution, but the cusp structure is still well recognizable and so are the ratios of the electron spectrum among the "bands" corresponding to different n.

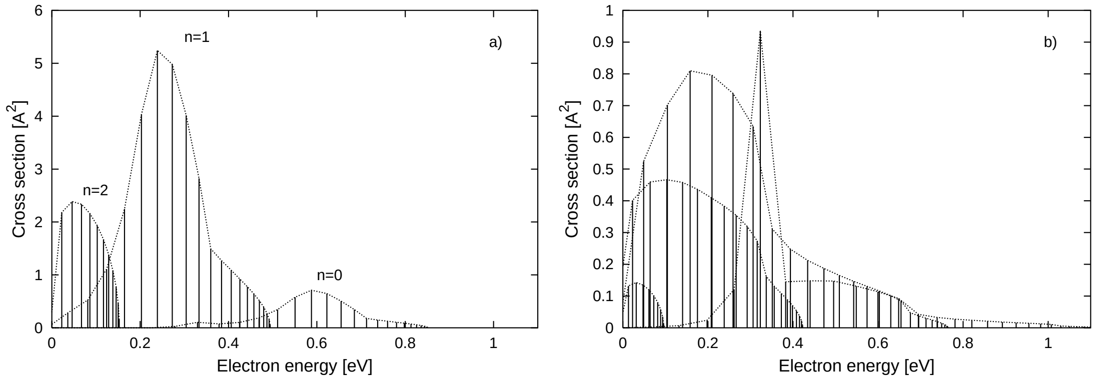

Figure 5.17: The spectrum of energy of the electron released in the AD process. The collision energy is 30 meV for the Figure a) and 300 meV for the Figure b).

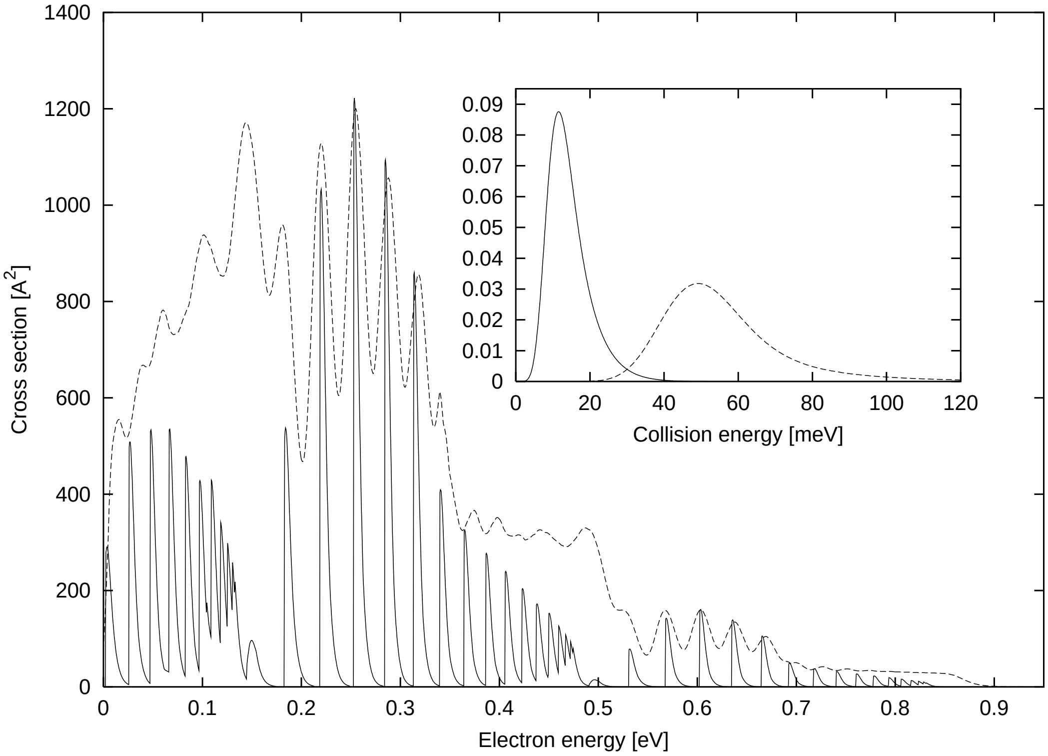

Figure 5.18: The spectrum of electrons released in the AD for HCl. The two collision energy distributions considered are shown at the top-right. The dashed spectrum is multiplied by a factor of 10.

5.3 Collisions of other halogen anions with atomic hydrogen

We present some preliminary also results for collisions of F^- and Br^- with atomic hydrogen in this section. The study of F^- is almost finished. It remains to discuss some fine details of the model in more details and also to discuss origin of discrepancy between our fully quantum calculation and the calculation of Gallup, Xu and Fabrikant [52] employing the nonlocal semiclassical theory, which was very successful in reproducing the results of fully quantum calculation of Domcke and Mündel [67] for e^-+HCl scattering.

We also show the results for Br^-+H collisions calculated within model of Horáček and Domcke [32]. The model has been constructed for e^-+HBr collisions and it does not contain the correct long range H+Br^- interaction important for AD. This results in disagreement with experiment for small collision energies.

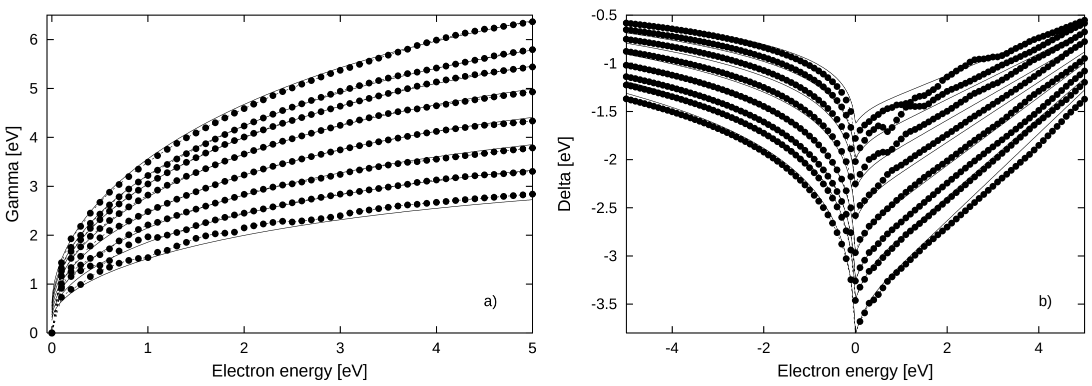

Figure 5.19: The data for the level shift Δ and width Γ calculated by Gallup, Xu and Fabrikant and our fit of these data. The value of the internuclear coordinate R is 1.5, 1.65, R_0, 1.85, 2.0, 2.15, 2.30, 2.489 from top to bottom (bottom to top) in the Figure a (b). Solid line shows the analytic fit to the data.

Model for $F^- + H$

A new nonlocal resonance model for HF^- resonance interacting with HF+e^- continuum has been constructed recently by Gallup, Xu and Fabrikant (GXF) [52]. The authors published also nonlocal semiclassical calculation of DA process. The data of GXF for the quantities $\Gamma(\epsilon, R)$ and $\Delta(\epsilon, R)$ [93] are shown in the Figure 5.19. The molecule HF posses a supercritical dipole, which means that the threshold behavior (2.84) has to be modified [52] and the function $\Gamma(\epsilon, R)$ exhibits infinitely many oscillations for $\epsilon \to 0$. On the other hand these oscillations occur for very small ϵ ($< 1\,\mathrm{meV}$) and they can not produce any observable effect. GXF suggested to smooth the function $\Gamma(\epsilon)$ near the origin and to allow $\Gamma(\epsilon)$ to attain certain nonzero value at $\epsilon = 0$.

As we have stressed above, it is very important for the efficiency of the calculation to separate ϵ and R dependencies in the nonlocal potential $f_J(\epsilon, R, R')$.

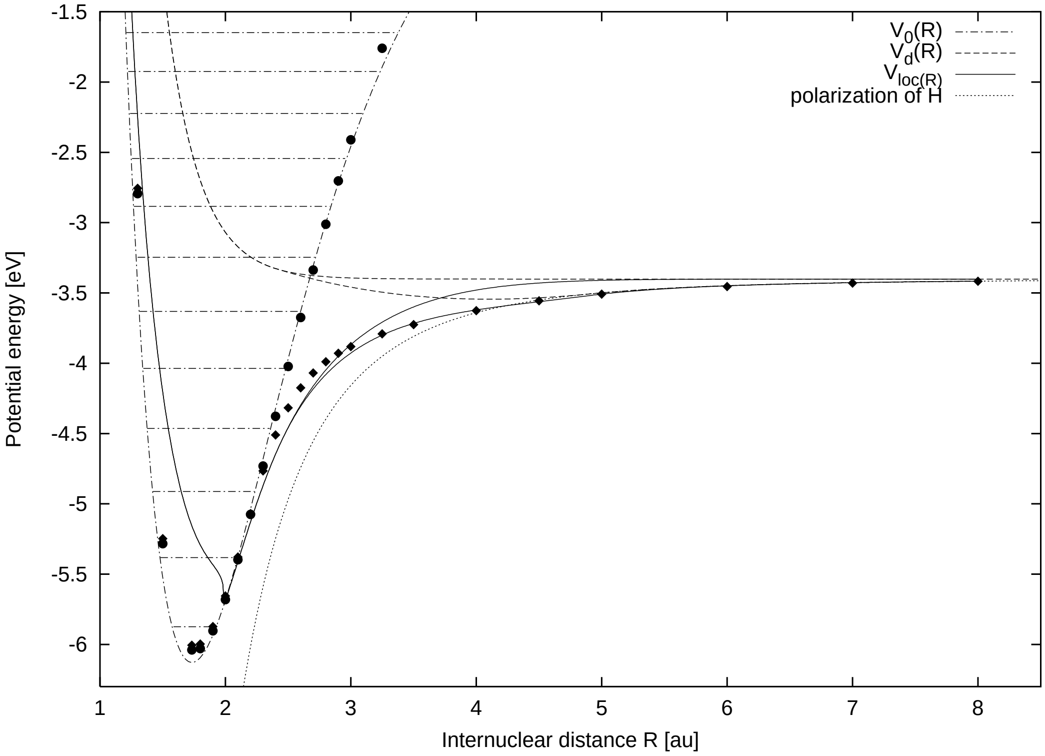

Figure 5.20: The potentials for the resonance model of HF^- collision complex. Ab initio data of Piecuch [94] are shown with diamonds (HF^-) and circles (HF) respectively. Functions $V_0(R)$ and $V_\mathrm{d}(R)$ are shown for both new model and original model of GXF.

In the analogy with the previous treatment we assumed

$$\Gamma(\epsilon, R) = \gamma(\epsilon) g(R)^2, \tag{5.25}$$

$$\Delta(\epsilon, R) = \delta(\epsilon) g(R)^2, \tag{5.26}$$

which is equivalent to the separability of the coupling element $V_{\mathrm{d}\epsilon}(R) = f(\epsilon)g(R)$, and we fitted the data of GXF with certain analytic form of $\gamma(\epsilon)$, $\delta(\epsilon)$ and $g(R)$ (see the appendix B for the resulting functions). Unlike for HCl we did two separate fits for γ and δ because we do not have any information on large-ϵ behavior of γ needed to perform the Hilbert transform (2.19) correctly. The resulting separable expressions for $\Gamma(\epsilon, R)$ and $\Delta(\epsilon, R)$ fit reasonably the data of GXF [93] as can be judged form the Figure 5.19.

To fix the long range interaction for the F^-+H potential we employed the same algorithm as was used above for HCl and accurate *ab initio* data for HF^- potential, resulting from the coupled-cluster calculation of Piecuch [94]. The model functions $V_0(R)$, $V_\mathrm{d}(R)$ and $V_1(R)$ are shown in the Figure 5.20, together with the *ab initio* data.

The behavior of the total AD cross section (Figure 5.21) is very similar to the case of HCl and it is in a very good agreement with the experimental data of Huels et al. [1] which, however, can not resolve the threshold structures. Probability

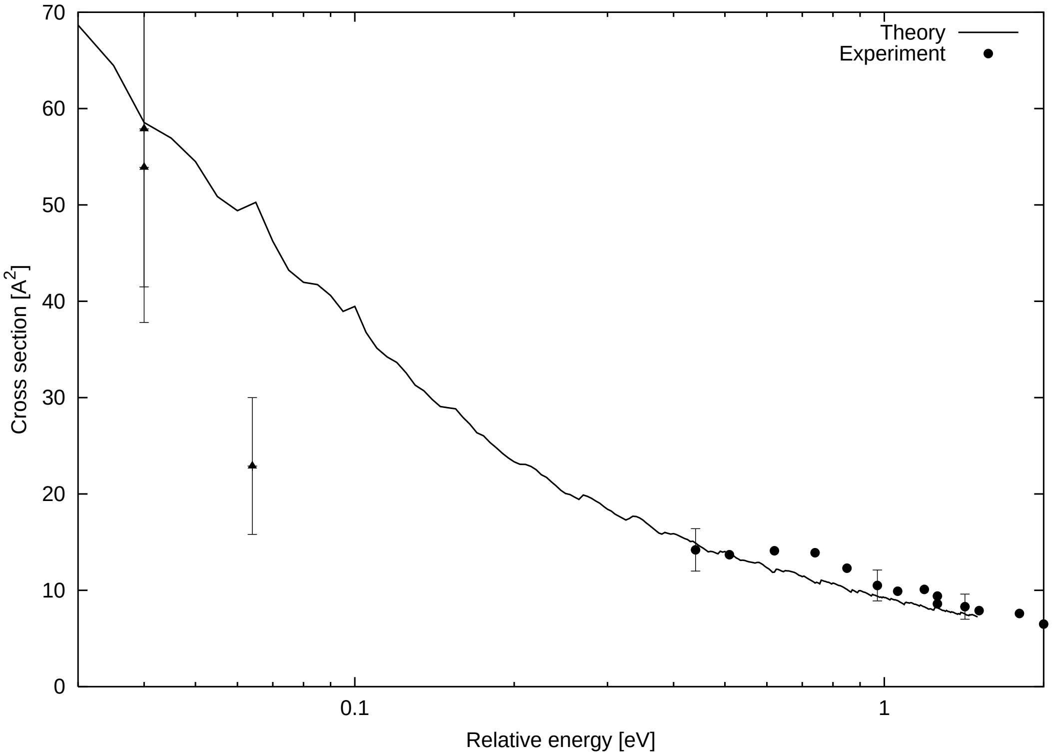

Figure 5.21: Total AD cross section for HF. Comparison of our calculation (solid line) with the experimental data of Huels et al. [1].

of the detachment to the different final states, defined by expression (5.20), is shown in the next Figure. The main difference, as compared to HCl, is that more final states are available. Also the total probability for the AD process to occur is smaller and the cusps are more pronounced. The "bands" corresponding to different vibrational states of the final molecule HF are not well separated in electron spectrum (Fig. 5.23) even for thermal energies $E = 30\,\text{meV}$, which is partly due to stronger attraction of H+F$^-$ (allowing for more partial waves) than for HCl and partly due to larger separation of the rotational levels because of larger equilibrium distance of the nuclei in the HF molecule. Nevertheless, the Wigner cusps are well recognizable in the convoluted spectrum (Fig. 5.24) for the same reasons which were discussed in the HCl case.

Preliminary results for HBr

The total AD cross section calculated within the model of Hráček and Domcke [32] is shown in Figure 5.25 together with the experimental data of Huels et al [1]. The long range part of the model was not properly adjusted which results in the incorrect behavior for small collision energies. We plan to remove this deficiency in future. Too weak attraction of H and Br$^-$ allows only few partial waves to penetrate into the detachment region and this results in well separated "bands" in the electron spectrum (Figure 5.26). Note that only two vibrational

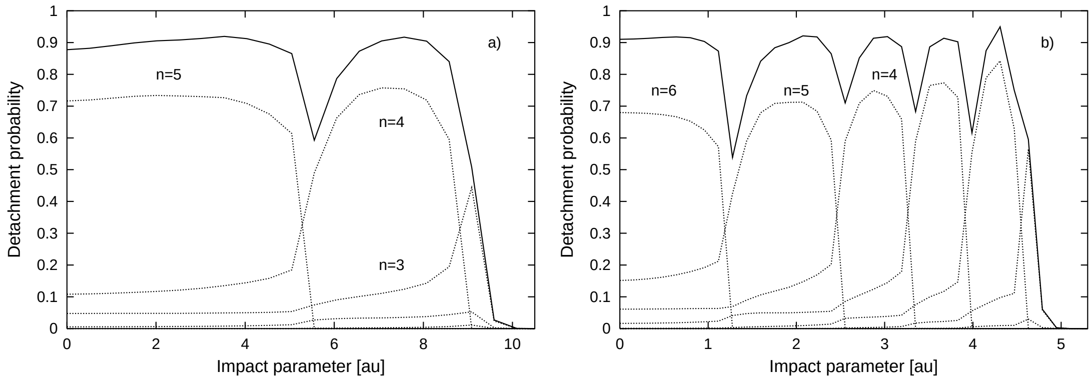

Figure 5.22: Probabilities for detachment of F^- into different final states of HF and the total detachment probability (solid line) as functions of the impact parameter. Collision energy of F^-+H is 30 meV (a) and 300 meV (b) respectively.

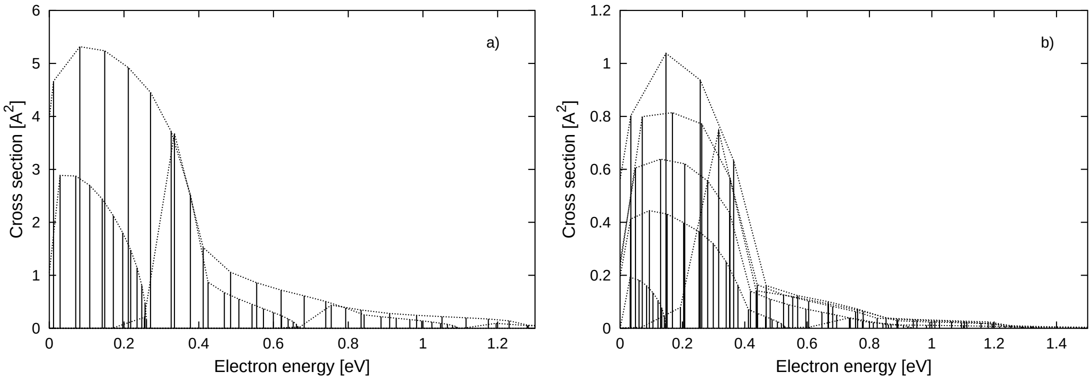

Figure 5.23: Energy spectra for electron released in associative detachment of F^-.

states ($n = 0, 1$) are allowed in this case.

The system H+I^- is also of theoretical interest since the AD reaction is endoenergetic and the total AD cross section is no longer decreasing like for other discussed halogen systems [1]. This behavior has been predicted recently in diploma thesis of Karel Houfek using the semiempirical nonlocal resonance model of Horáček, Domcke and Nakamura [75]. Ab initio construction of the model would be a very difficult task in this case since relativistic effects are important for heavy I^- ion.

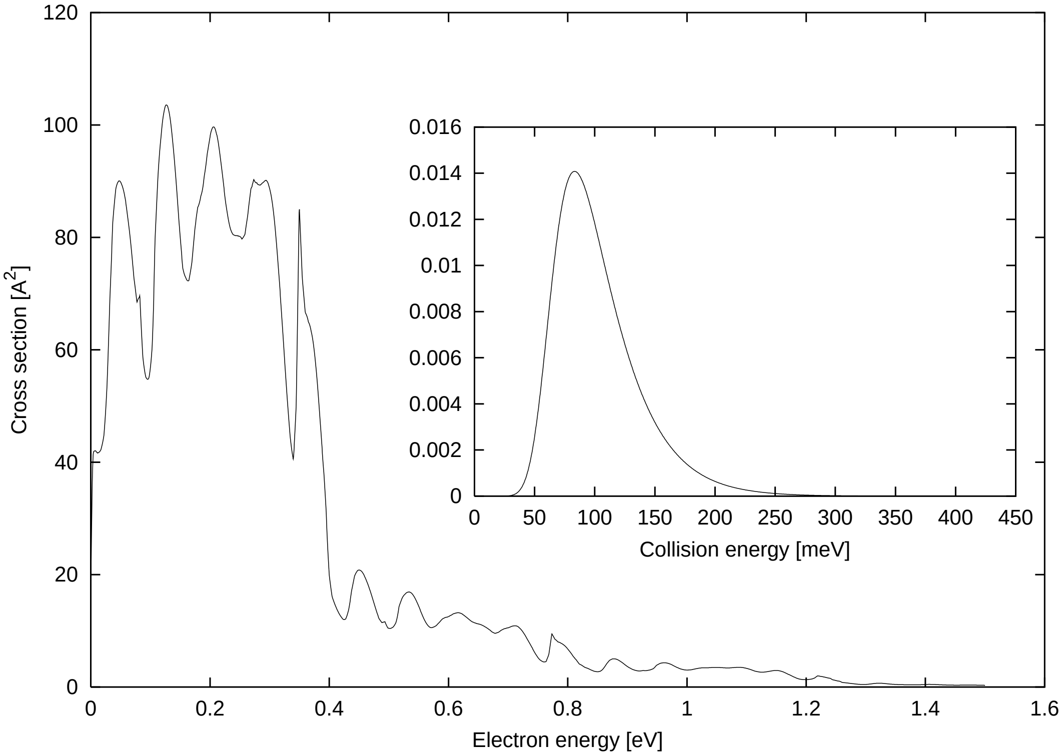

Figure 5.24: Energy spectra for electron released in associative detachment of F^- with realistic collision energy distribution considered.

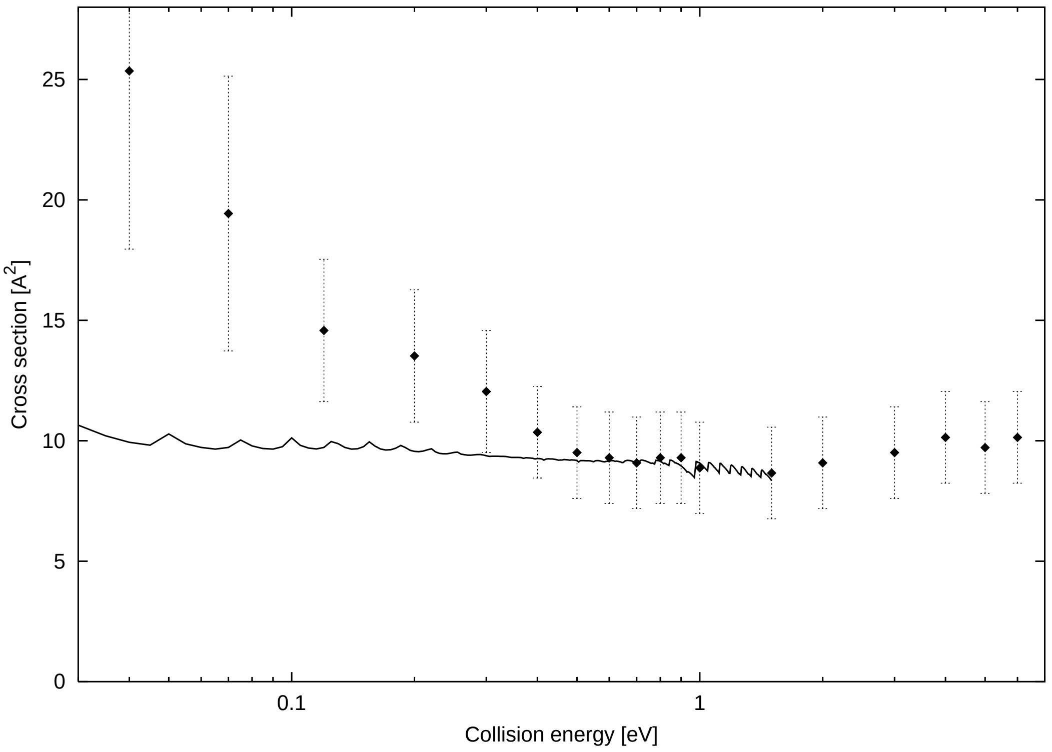

Figure 5.25: The calculated total AD cross section for HBr and the experimental data of Huels et al. [1].

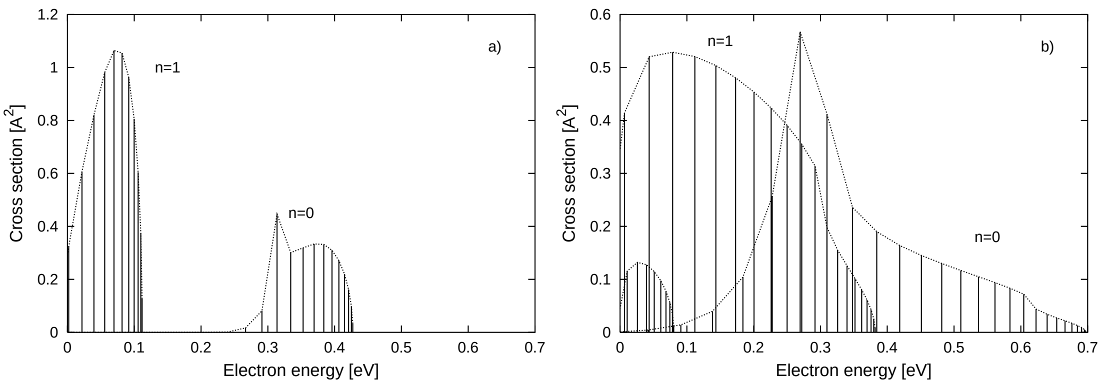

Figure 5.26: The spectrum of electron released in AD for HBr. Prediction based on the model of Horáček and Domcke [32]. The collision energy is 30 meV (a) and 300 meV (b).

Chapter 6

Penning ionization in cold He*+He* collisions

Experimental and theoretical effort in 1980's has led to development of new devises for laser manipulation and cooling of atomic beams and gases. The field has further been rapidly developing after first observation of Bose-Einstein condensation in laser cooled atomic gas [95]. Atomic lasers which have already been demonstrated in several groups producing coherent de Broglie waves of whole atoms may provide tools for a new generation of scattering experiments. New atom optics devices (including holography and guiding of atoms in waveguides) may soon become powerful tools in both research and technology.

Optical manipulation and cooling of atoms is achieved employing the recoil force of a photon with frequency close to certain atomic transition. The force is thus velocity dependent due to Doppler shift of the photon frequency and shifting of the atomic levels in a convenient magnetic or electric field can be used to achieve desired cooling and/or trapping configuration. For more information on optical manipulation, cooling and trapping of atoms see for example the review in [96], [97] or [98] and references therein.

All traps based on optical manipulation of the trapped atoms are designed to trap only the atoms in a limited small set of states. If the atom ends in a different state after any process occurring in the trap it escapes out of the trap. We study an important trap loss process for metastable helium in magnetooptical traps in this chapter. This theoretical work has been done in connection with experiments in group of atomic physics at University of Utrecht. The trap for metastable helium is operated on the transition

$$\mathrm{He}^*(2^3\mathrm{S}) \xleftrightarrow{\mathrm{h}\nu} \mathrm{He}^*(2^3\mathrm{P}).$$

The most important trap loss processes are the Penning ionization (PI) and related associative ionization (AI)

$$\begin{aligned} \mathrm{He}^* + \mathrm{He}^* &\rightarrow \mathrm{He} + \mathrm{He}^+ + \mathrm{e}^-, & (6.1)\\ &\rightarrow \mathrm{He}_2^+ + \mathrm{e}^-, & (6.2) \end{aligned}$$

where both ions (He^+ and He_2^+) and ground-state-atoms $\mathrm{He}(1^1S)$ escape from the trap. To get a deeper understanding of the process the energy of the escaping ions was measured by time-of-flight method and compared with theoretical predictions reported below. We would like to stress that the processes (6.1) and (6.2) are of resonance character and are in many aspects very similar to associative detachment studied in the previous chapter.

The spectrum of electron released in the Penning and associative ionization (6.1), (6.2) was investigated both experimentally and theoretically in the recent article of Müller et al. [99]. They investigated $He^*(2^3S) + He^*(2^3S)$ collisions in detail. In the experiments with He in magnetooptical trap the collisions of helium in the 2^3P state are important. This chapter is an attempt to estimate the shape of the electron spectra for $He^*(2^3S) + He^*(2^3P)$ collisions from the incomplete information about the adiabatic potentials and autoionization widths and an attempt to find out which parameters are most important for the shape of the spectra. The treatment of Müller et al. [99] is generalized here by inclusion of more potentials relevant for $He^*(2^3S)+He^*(2^3P)$ collisions and considering the coupling among them. We demonstrate that this coupling is important for the shape of the spectra.

6.1 Electronic structure of He*+He* system

Before going to the system of two excited helium atoms we would like to give the table of few first energy levels of a single helium atom:

State	Configuration	Energy[eV]
1^1S	$1s^2$	-24.586
2^3S	**1s2s**	**-4.768**
2^1S	1s2s	-3.972
2^3P	**1s2p**	-3.**623**
2^1P	1s2p	-3.369
3^3S	1s3s	-1.869
⋮	⋮	⋮

Energies in the table are given relative to the ground state of He^+. States used for the laser cooling are printed in bold face. The live-time of the metastable 2^3S state is sufficiently long to be treated as stable in the experiment. All combinations of He(2^3S or 2^3P) + He(2^3S or 2^3P) collisions may occur in the MOT.

Let us now investigate the electronic structure of the $He^* + He^*$ system. The possibility of the transition to a different electronic state by spontaneous emission of light will be neglected in the following treatment. The potential curves of the metastable states calculated by Müller et. al. [99] are shown in Figure 6.1 and He_2^+ potentials [100] are plotted at the bottom of the figure. All considered metastable states lie high in the continuum of $He_2^+ + e^-$. Unlike all systems discussed in the previous two chapters the metastable states are not bound for any internuclear coordinate R. However, the autoionization probability is very small for large R since some interaction between the outermost electrons of the two helium atoms has to take place in order to autoionize. If the two excited He atoms come close together one of the excited electrons can give part of its energy to the other excited electron and the respective atom will end in the ground state while the other electron have enough energy to escape. One possible way to define the discrete

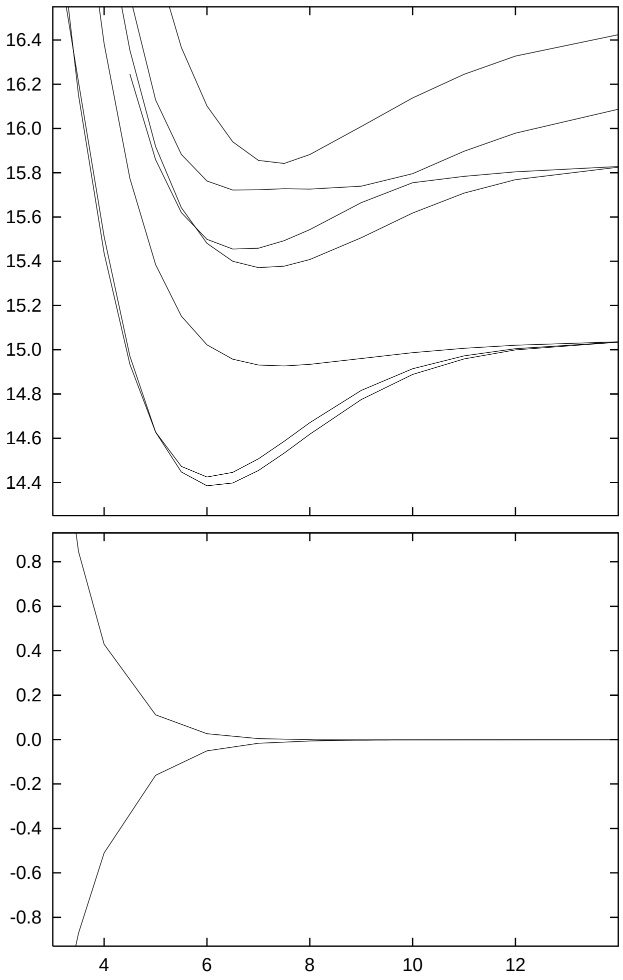

Asymptote	Energy	Potentials
$\leftarrow$ $\mathrm{He}^*(2^3\mathrm{S})+\mathrm{He}^*(2^1\mathrm{P})$	16.45	$3^3\Sigma_g^+$
$\leftarrow$ $\mathrm{He}^*(2^3\mathrm{S})+\mathrm{He}^*(2^3\mathrm{P})$	16.19	$2^3\Sigma_g^+$
$\leftarrow$ $\mathrm{He}^*(2^3\mathrm{S})+\mathrm{He}^*(2^1\mathrm{S})$	15.85	$1^3\Sigma_g^+$ $2^3\Sigma_u^+$
$\leftarrow$ $\mathrm{He}^*(2^3\mathrm{S})+\mathrm{He}^*(2^3\mathrm{S})$	15.05	$1^5\Sigma_g^+$ $1^3\Sigma_u^+$ $1^1\Sigma_g^+$
$\leftarrow$ $\mathrm{He}(1^1\mathrm{S})+\mathrm{He}^+(1\mathrm{s})$	0	${}^2\Sigma_g^+$ ${}^2\Sigma_u^+$

Figure 6.1: Potentials for $\mathrm{He}^*+\mathrm{He}^*$ and $\mathrm{He}^*+\mathrm{He}^+$. Energies are given in eV, R in a_0.

states and the respective potential curves is to restrict the Hilbert space not to contain the configurations with three electrons tightly bound and one diffuse very weakly bound electron [99]. Let us denote $\mathcal{Q}$ this part of the total electronic Hilbert space $\mathcal{H}$ and $\mathcal{P}$ the rest of it (containing the continuum). Potential curves $V_*^{(m)}(R)$ for metastable states $\phi_*^{(m)}(R,r)$ are then obtained by diagonalization of electronic Hamiltonian H_{el} (including nucleus-nucleus Coulomb interaction) in the space $\mathcal{Q}$ for each inter-nuclear distance R

$$\left(QH_{\mathrm{el}}(R,r)Q - V_*^{(m)}(R)\right)\phi_*^{(m)}(R,r) = 0. \tag{6.3}$$

Here we denoted with Q the projection operator on the $\mathcal{Q}$-space and r stands for all electron coordinates. Similarly the diagonalization in the $\mathcal{P}$ yields the continuum states

$$\left(PH_{\mathrm{el}}(R,r)P - V_+^{(i)}(R) - \epsilon\right)\phi_+^{(i)}(\epsilon,R,r) = 0, \tag{6.4}$$

where ϵ is the electron energy, $V_+^{(i)}(R)$ is the potential of the $i-$th He_2^+ state and the function $\phi_+^{(i)}(\epsilon,R,r)$ describes the scattering on this state. We thus have situation similar to that assumed in the Chapter 2 but with many discrete states $\phi_*^{(m)}(R,r)$ and two continua $\phi_+^{(i)}(\epsilon,R,r)$. Now we can define a coupling between each of the states and each continuum

$$V_{+*}^{(im)}(\epsilon,R) = \int dr\, \phi_+^{(i)}(\epsilon,R,r)^* H_{\mathrm{el}} \phi_*^{(m)}(R,r) \equiv V_{*+}^{(mi)}(\epsilon,R)^* \tag{6.5}$$

and

$$\Gamma^{(im)}(\epsilon,R) = 2\pi \int d\hat{\epsilon} |V_{+*}^{(im)}(\epsilon,R)|^2 \tag{6.6}$$

can be interpreted as autoionization width of the state $\phi_*^{(m)}$ relative to continuum $\phi_+^{(i)}$. The diagonalization in the $\mathcal{P}$ part of the Hilbert space is more difficult, because it contains the continuum. In the Chapter 2 we briefly described the construction of the continuum states $\phi_+^{(i)}$ from the solution of the Lippmann-Schwinger equation with the additional constraint $Q\phi_+^{(i)} = 0$. Another possible strategy is to calculate approximation of continuum states within finite, square integrable basis in $\mathcal{P}$ and then to extract continuous functions $\Gamma^{(im)}(\epsilon,R)$ using Stieltjes imaging (See [101, 99, 22] for the details). Standard methods of quantum chemistry for calculation of molecular bound states can thus be used. If the continuum wave functions $\phi_+^{(i)}$ are expanded into partial waves, like in the section 2.3, the width can be written in the form

$$\Gamma^{(im)}(\epsilon,R) = 2\pi \sum_l |V_{+*l}^{(im)}(\epsilon,R)|^2, \tag{6.7}$$

where l refers to an angular momentum of the electron released in the autoionization process.

Before we start to investigate the dynamics of the nuclei in such a system we have to overcome one additional difficulty in order to be able to introduce Born-Oppenheimer approximation.

Construction of diabatic curves

It is apparent from the Figure 6.1 that there are avoided crossings among the three lowest $^3\Sigma_g^+$ potentials. Such a phenomenon occurs in the place where electronic wave function suddenly changes its character. In order to apply the resonance formalism for the calculation of the nuclear dynamics we would like to find the diabatic representation where the electronic wave function behaves smoothly with R. This requires the construction of six curves—three potentials (let us call them $V_*^{(1)}(\mathrm{R})$, $V_*^{(2)}(\mathrm{R})$ and $V_*^{(3)}(\mathrm{R})$) and three couplings $C_{12}(\mathrm{R})$, $C_{23}(\mathrm{R})$ and $C_{13}(\mathrm{R})$. No *ab initio* calculation is available for the diabatic potentials and the couplings. We used the *ab initio* data for adiabatic curves depicted in Figure 6.2 instead (see [99] for the table of the data) and determined the diabatic curves in the following way. Let us assume certain analytic form of the diabatic potentials

$$\begin{aligned} V_*^{(1)}(R) &= A_1 e^{-\alpha_1(R-R_2)} - b\left[(R-c)^2+d\right]^{-3} + E_1 & (6.8)\\ V_*^{(2)}(R) &= A_2(e^{-\alpha_2(R-R_2)}-1)^2 - A_2 + E_2 & (6.9)\\ V_*^{(3)}(R) &= A_3(e^{-\alpha_3(R-R_3)}-1)^2 - A_3 + E_3. & (6.10)\end{aligned}$$

The last two functions are Morse potential functions shifted to match the proper asymptote. Minimum of the first potential is too shallow to be properly described with Morse function and we took exponential function with an additional term vanishing like R^{-6} at infinity. The constants E_1, E_2 and E_3 are the asymptotic energies of each potential (the values given in the Figure 6.1). For the couplings we assumed

$$C_{12} = C_{13} = Ae^{-\alpha R} \tag{6.11}$$

and $C_{23} = 0$ (the two curves $V_*^{(2)}$, $V_*^{(3)}$ do not cross each other and the coupling should not be so important). Now we can find the adiabatic potentials U_1, U_2 and U_3 for each R from the solution of the algebraic equation

$$\begin{vmatrix} x - V_*^{(1)}(R) & C_{12} & C_{13} \\ {C_{12}}^* & x - V_*^{(2)}(R) & C_{23} \\ {C_{13}}^* & {C_{23}}^* & x - V_*^{(3)}(R) \end{vmatrix} = 0. \tag{6.12}$$

The constants A_i, α_i, R_i, b, c, d, α and A are chosen in such a way, that the solutions $x = U_1$, U_2, U_3 are the best least square fit to the data of Müller et al [99]. The resulting values are given in the following table (R in a.u., energies in meV).

$A_1 = 203.1$	$\alpha_1 = 0.9379$		$b = 7528000$
$A_2 = 739.2$	$\alpha_2 = 0.3362$	$R_2 = 6.682$	$c = 7.269$
$A_3 = 707.1$	$\alpha_3 = 0.3948$	$R_3 = 6.46$	$d = 33.59$
$A\ = 1381$	$\alpha\ = 0.4582$		

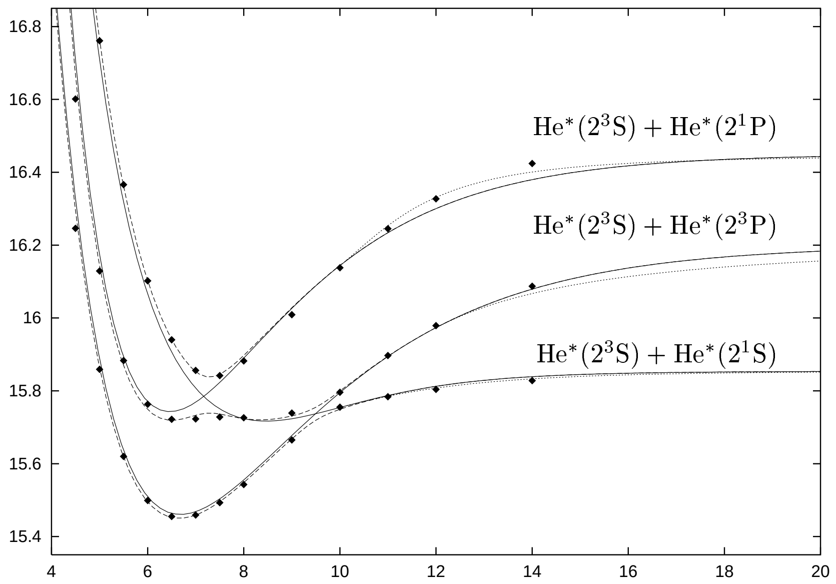

Figure 6.2: Diabatic potentials for the ${}^3\Sigma_g^+$ metastable states (full lines). The dots show corrections to the long range behavior. Adiabatic potentials are plotted with long dashes and the *ab initio* data with the diamonds.

Resulting diabatic potentials $V_*^{(1)}(R)$, $V_*^{(2)}(R)$ and $V_*^{(3)}(R)$ are depicted in the Figure 6.2 together with adiabatic curves U_1, U_2, U_3 and with the *ab initio* data of Müler et al. [99]. We expect that the diabatic curves $V_*^{(i)}(R)$ obtained with just described procedure are quite accurate, because the curves should lie near adiabatic *ab initio* data except in the vicinity of the crossings where they switch from one curve to another. On the other hand the *ab initio* data provide an information about the $C_{12}(R)$ and $C_{13}(R)$ couplings only in the vicinity of the respective crossings. The assumption (6.11) is just one of the ways how to put no more than two parameters into all coupling curves $C_{12}(R)$, $C_{13}(R)$ and $C_{23}(R)$. To test the sensitivity of the predictions for PI and AI on this kind of artificial assumptions, we constructed the second model in the same way as the first, but with the assumption

$$C_{12} = B_2 e^{-(R-X_2)^2} \tag{6.13}$$
$$C_{13} = B_3 e^{-(R-X_3)^2}, \tag{6.14}$$

where $X_2 = 9.48$ and $X_3 = 7.16$ are the crossing points obtained by linear interpolation of the *ab initio* data. In this case we have got the best fit of the adiabatic potentials for the values:

$R_2 = 6.65$	$A_1 = 239.4$	$\alpha_1 = 0.8931$	$b = 7996000$
$R_3 = 6.414$	$A_2 = 750.6$	$\alpha_2 = 0.3368$	$c = 7.223$
$B_2 = 10.3$	$A_3 = 721.5$	$\alpha_3 = 0.3982$	$d = 33.95$
$B_3 = 56.6$			

We will call the first model with the couplings (6.11) the model $\mathcal{A}$ and the second the model $\mathcal{B}$. Note that the two models differ significantly only in C_{12}, and C_{13}, but $C_{12}^{\mathcal{A}}(X_2) \simeq C_{12}^{\mathcal{B}}(X_2)$ and $C_{13}^{\mathcal{A}}(X_3) \simeq C_{13}^{\mathcal{B}}(X_3)$. No information about C_{12} and C_{13} far from X_2 and X_3 can be obtained from the adiabatic potentials.

The functions (6.8)-(6.10) do not meet the correct van der Waals asymptotes for large R. The values of the C_6 and C_8 coefficients for the $1^1\Sigma_g^+$, $1^3\Sigma_u^+$, $1^5\Sigma_g^+$, $2^3\Sigma_u^+$ and $1^3\Sigma_g^+$ ($\rightarrow V_*^{(1)}(R)$) potentials are given in [99]. The values of C_3 for other two $^3\Sigma_g^+$ states $V_*^{(2)}(R)$ and $V_*^{(3)}(R)$ are $C_3 = 12.83$ and 2.93 (in a.u.) respectively [102]. We added another two terms to join the curves (6.8)-(6.10) smoothly. The resulting asymptotes are

$$\begin{aligned}
V_*^{(1)} &= -5.839\mathrm{E}3R^{-6} - 4.194\mathrm{E}5R^{-8} + 1.0325\mathrm{E}8R^{-10} - 3.9594\mathrm{E}9R^{-12} && \text{for } R > 10,\\
V_*^{(2)} &= -12.83R^{-3} + 1.5295\mathrm{E}3R^{-6} - 6.0928\mathrm{E}5R^{-8} && \text{for } R > 12,\\
V_*^{(3)} &= -2.93R^{-3} - 3.5278\mathrm{E}8R^{-10} + 2.6949\mathrm{E}10R^{-12} && \text{for } R > 10,
\end{aligned}$$

for the model $\mathcal{A}$ and the same for the model $\mathcal{B}$ except that it is better to match the potential curve $V_*^{(3)}(R)$ with the asymptote at $R = 10.8$ rather then at $R = 10$.

6.2 Theoretical description

As we have mentioned before the theory for Penning and associative ionization has much in common with the theory of the associative detachment process. We therefore start with the simplified case of one discrete state interacting with one continuum in the next paragraph and we try to point out similarities and deviations from the theory used in the previous sections to describe electron-molecule and ion-atom collisions. Some approximations which are known to work well if the separation of the potentials V_* and V_+ is large are introduced and application to He$^*(2^3$S) + He$^*(2^3$S) collisions is discussed. Finally we give a few notes about the complications arising from the model containing more discrete states and more continua.

Interaction of one metastable state with one continuum

If we consider only one discrete state $\phi_*^{(m)}$ and one continuum $\phi_+^{(i)}$ we can omit unnecessary superscripts m, i and we can repeat the derivation from the Chapter 2 to get equation (2.36) for the projection of the wave function on the discrete electronic state ϕ_* and after partial wave expansion we end with the equation (2.55). It is further known [30] that for well separated potentials $V_*(R)$ and $V_+(R)$ (it is $V_* - V_+ \sim 15$eV for He*+He*collisions) the local approximation (3.27)-(3.30) can be used so that the final equation for the partial wave component of the projected wave function reads

$$\psi_{*J}(R) = u_J(E_*, R) + \int dR'\, G_J(E_*, R, R')\, [V_{\mathrm{loc}}(R') - \tfrac{i}{2}\Gamma_{\mathrm{loc}}(R')]\, \psi_{*J}(R'). \quad (6.15)$$

In the case of metastable helium collisions the autoionization width Γ is very small and its Hilbert transform Δ can be neglected in comparison with $V_*(R)$ so that

$$V_{\mathrm{loc}}(R) = V_*(R), \quad (6.16)$$

$$\Gamma_{\mathrm{loc}}(R) = \Gamma(\epsilon, R, R)\big|_{\epsilon = V_*(R) - V_+(R)}. \quad (6.17)$$

This local approximation can also be derived from semiclassical arguments and the quantity $E_{\mathrm{res}}(R) = V_*(R) - V_+(R)$ is interpreted as the energy of the electron emitted in the autoionization at a given point R. The quantity $\Gamma_{\mathrm{loc}}(R)$ then gives the autoionization rate at the given point R. Another nice derivation of the local approximation within the time-dependent picture can be found in [4] including the first order nonlocal corrections to the approximation (see footnote on the page 28).

For the calculation of the spectra of electrons released in the process (6.1), (6.2) we also need the scattering wave function for He+He$^+$channel, i. e. we have to solve

$$\left(-\frac{1}{2\mu}\frac{d^2}{dR^2} + V_+(R) + \frac{J(J+1)}{2\mu R^2} - E_*\right)\psi_*^J(R) = 0 \quad (6.18)$$

or the equivalent Lippmann-Schwinger equation. The energy spectrum of the electrons released after the ionization is given by formula[1] (see [10, 99])

$$\begin{aligned} \frac{\mathrm{d}\sigma}{\mathrm{d}\epsilon} &= \frac{2g_*}{E_*\sqrt{E_* E_+}} \sum_J (2J+1)\, |T_J(E_+, E_*)|^2 && \text{PI region } (E_+ > 0) \\ &= \sum_{\nu J} \sigma_\nu^J \delta(\epsilon - E_\nu^J) && \text{AI region } (E_+ < 0), \end{aligned} \quad (6.19)$$

where E_ν^J are the energies of bound states in $V_+ + \frac{J(J+1)}{2\mu R^2}$, σ_ν^J is the cross section for AI into individual levels

$$\sigma_\nu^J = \frac{2\pi g_*}{E_* K_*}\,(2J+1)\left|T_J(E_\nu^J, E_*)\right|^2 \quad (6.20)$$

[1] For the normalization of the wave function see Appendix C.

and

$$T_J(E_+, E_*) = \int \mathrm{d}R'\, \psi_+^J(E_+, R') V_{+*}(E_* - E_+, R') \psi_*^J(E_*, R') \tag{6.21}$$

is the T-matrix element for ionization. In the formula (6.21) we have assumed again that the angular momentum transfer from light electron to the heavy nuclei can be neglected. In this case we can write

$$V_{+*} \approx \sqrt{\Gamma(E_* - E_+, R)} \approx \sqrt{\Gamma(R)} \tag{6.22}$$

in the formula (6.21). Replacement of $\Gamma(E_* - E_+, R)$ with $\Gamma(R)$ can be justified by stationary phase arguments, if the wave functions ψ_{+J} and ψ_{*J} in the formula (6.21) are replaced with their WKB approximation [103].

Application to He*(2³S) + He*(2³S) collisions

The potential curves $V_*(R)$ connected to He*(2³S) + He*(2³S) asymptote do not have crossings with another curves of the same symmetry and they can be treated independently. The cross sections are obtained as sums over contributions from each individual curve and each contribution is calculated from the model of one discrete state interacting with one continuum. The statistical g-factors are $g_* = 1/9$ for $^1\Sigma_\mathrm{g}^+$ state, $g_* = 3/9$ for $^3\Sigma_\mathrm{u}^+$ state and $g_* = 5/9$ for $^5\Sigma_\mathrm{g}^+$ state. These numbers give statistical probability for a particles to come to each other along given potential curve and they can be changed if the scattering state is specially prepared (for example manipulated by laser light or spin oriented in a strong magnetic field). Few additional remarks are necessary

1. The state $^5\Sigma_\mathrm{g}^+$ does not contribute because $\Gamma = 0$ for the quintet states (quintet state with all electron spins parallel can not directly decay in doublet plus electron because of total spin conservation).

2. We have two final states $^2\Sigma_\mathrm{u}^+$ and $^2\Sigma_\mathrm{g}^+$ of He_2^+. This manifests itself in the fact that Γ is the sum of two terms $\Gamma = \Gamma_\mathrm{u} + \Gamma_\mathrm{g}$, where Γ_u and Γ_g are auto-ionization widths into each final state. This full Γ has to be used in the optical potential $V_* - \frac{i}{2}\Gamma$ in the equation of motion and equations for the cross sections describing thus ionization into two possible final states but we have to put the individual Γ_u and Γ_g into the formula (6.21) for the spectra. Thus full spectrum is the sum of four terms (two for each V_* potential curve times two possible final states).

3. Neglection of $l > 0$ is not possible for $^3\Sigma_\mathrm{g}^+ \to {}^2\Sigma_\mathrm{u}^+$ and $^1\Sigma_\mathrm{u}^+ \to {}^2\Sigma_\mathrm{g}^+$ transition since l has to be an odd number in order to conserve overall gerade (ungerade) symmetry of the system. We can, however, use the single partial wave approximation again neglecting all $l > 1$ and preserving only $l = 1$. The formula (6.21) has to be generalized (see [10, 99]). We faced the similar problem in the Chapter 4.

4. Exchange symmetry imposes restrictions on homo-nuclear systems like investigated He*+He*. Partial waves with an even/odd J are not allowed for

the wave function in the case of potential with Σ_u^+/Σ_g^+ symmetry respectively. Thus the sum in (6.19) has to be performed only over even or odd values of J for Σ_g^+ and Σ_u^+ potential, respectively. Lack of half of the terms has to be compensated with an additional factor of 2 in the formula (6.19).

Fore more detailed discussion of the $\mathrm{He}^*(2^3\mathrm{S}) + \mathrm{He}^*(2^3\mathrm{S})$ collisions see [99].

Several states and several continua

As in the previous case we can define projections $\psi_*^{(m)}$ of the wave function on the discrete states $\phi_*^{(m)}$. The equation for $\psi_*^{(m)}$ has in fact been already contained in the general expression (2.28). After partial wave expansion we obtain for the vector ψ_{*J} with the components $\psi_{*J}^{(m)}$ formally the same equation as before for the single function ψ_{*J} but now with the nonlocal potential F being the matrix

$$F_{mn}(E,R,R') = \int \mathrm{d}\epsilon \sum_i V_{*+}^{(mi)}(\epsilon,R)(E - T_\mathrm{N} - \epsilon - V_+^{(i)}(R) + i\varepsilon)^{-1} V_{+*}^{(in)}(\epsilon,R'). \tag{6.23}$$

The electron spectra are then obtained from formulae very similar to (6.19)–(6.21)

$$\frac{\mathrm{d}\sigma}{\mathrm{d}\epsilon} = \frac{2g_*}{E_*\sqrt{E_*E_+}} \sum_{Jf} (2J+1) \left| \sum_i T_J^{(fi)}(E_+,E_*) \right|^2 \tag{6.24}$$

for PI ($E_+ > 0$) and

$$\sigma_{\nu_f}^J = \frac{2\pi g_*}{E_* K_*} (2J+1) \left| \sum_i T_J^{(fi)}(E_{\nu_f}^J, E_*) \right|^2 \tag{6.25}$$

for associative ionization. Contributions to the T-matrix are

$$T_J^{(fi)}(E_+,E_*) = \int \mathrm{d}R'\, \psi_+^{(f)J}(E_+,R') V_{+*}^{(fi)}(\epsilon_f,R) \psi_*^{(i)J}(E_*,R'), \tag{6.26}$$

where $\epsilon_f = E_* - E_+$ is the energy of the electron released in the ionization process.

To obtain the local approximation to the nonlocal operator F_{mn} for example the time dependent treatment used in [4] could be generalized. Here we use an intuitive derivation based on the conservation of the probability flux. First, we assume that there is some local approximation

$$F_{mn} \approx V_{mn}(R) - \tfrac{i}{2}\Gamma_{mn}(R) \tag{6.27}$$

and we try to find its properties. Treatment of collisions for such a coupled channel problem is briefly summarized in the appendix C and the numerical methods introduced in the Chapter 3 are generalized for several coupled channels, also in the appendix C.1.

Like in the case of one state interacting with continuum we can neglect the influence of the continuum on V_* if the decay width is small in comparison with the differences in the potential relevant for the process. For the $^3\Sigma_g^+$ symmetry, the Hermitian part V_* of the potentials relevant for $\mathrm{He}^*(2^3\mathrm{S}) + \mathrm{He}^*(2^3\mathrm{P})$ collisions is given by diabatic potentials $V_*^{(m)}$ and the couplings C_{mn} constructed in the section 1. It is an natural assumption that the diagonal terms Γ_{mm} of the anti-Hermitian part of the potential are given by sum over possible final states of the decay widths for the metastable state m

$$\Gamma_{mm}(R) = \sum_f \Gamma^{(fm)}(R) \tag{6.28}$$

in the analogy with the case of one metastable state interacting with several continua. It is not clear however, how to obtain the non-diagonal terms.

Let us assume that, in the analogy with (6.22), it is

$$V_{+*}^{(fi)} \approx \sqrt{\Gamma^{(fi)}(R)} \tag{6.29}$$

where $\Gamma^{(fi)}(R)$ is a decay width of the state i relative to continuum f. Total ionization cross section is calculated integrating the spectra over all possible electron energies ϵ

$$\begin{aligned}\sigma_{\text{ion}} &= \int \mathrm{d}\epsilon \frac{\mathrm{d}\sigma}{\mathrm{d}\epsilon} = \frac{2\pi g_*}{E_* K_*} \sum_J (2J+1) \times \\ &\times \sum_{mn} \int \mathrm{d}R\, \psi_*^{(m)}(R)^* \sum_f \sqrt{\Gamma^{(fm)}(R)\Gamma^{(fn)}(R)}\psi_*^{(n)}(R). \end{aligned} \tag{6.30}$$

To obtain this expression equations (6.24)-(6.26) and the approximation (6.29) has been employed. Integration over ϵ has been performed using the completeness of the states in the ionization channel. Comparison of (6.30) with the ionization cross section (C.24) obtained from the flux lost in all the channels in the appendix C yields

$$\Gamma_{mn}(R) = \sum_f \sqrt{\Gamma^{(fm)}(R)\Gamma^{(fn)}(R)}. \tag{6.31}$$

This formula gives the local approximation to the antihermitian part Γ_{mn} of the potential in terms of the autoionization width $\Gamma^{(im)}$ of the discrete state $\phi_*^{(m)}$ relative to the continuum $\phi_+^{(i)}$. The formula (6.31) is also consistent with the results of Devriani et al [104] who studied two states interacting with continuum using the classical (time-dependent) description of the nuclear motion and quantum treatment of electronic degrees of freedom.

6.3 Results

We give a brief account of numerical results in this section. First, we investigate the He*$(2^3$S) + He*$(2^3$S) collisions, which have already been studied in detail by Müller et. al. [99] both theoretically and experimentally. In this way we test numerical performance of our software and we get some understanding of the PI/AI electron spectra. Later we proceed with the He*$(2^3$S) + He*$(2^3$P). There should be potentials of $^1\Sigma$, $^3\Sigma$, $^5\Sigma$, $^1\Pi$, $^3\Pi$ and $^5\Pi$ symmetry connected to the He*$(2^3$S) + He*$(2^3$P) asymptote. Only the $^3\Sigma_g^+$ potentials (shown in the Figure 6.2) were calculated in [99]. Quintet states can not autoionize and some of the other potentials might be repulsive and thus not important for a very-low energy collisions but we do not have any information about them. In this work we study only the ionization spectra due to $^3\Sigma_g^+$ manifold and especially the effects connected with the curve crossings and interaction of the discrete states due to the coupling via continuum. Sensitivity to other unknown or uncertain parameters in the model is also tested.

He*(2³S) + He*(2³S) collisions

To calculate the cross sections for the $\mathrm{He}^*(2^3\mathrm{S}) + \mathrm{He}^*(2^3\mathrm{S})$ collisions we used the method of section 3.1 to solve the Lippmann-Schwinger equation (6.15) and formulae (C.10)–(C.15) to get the cross sections. The following table contains the contributions to elastic (σ_{el}), ionization (σ_{ion}) and total (σ_{tot}) cross sections (in a_0^2) from $^1\Sigma_\mathrm{g}^+$ and $^3\Sigma_\mathrm{u}^+$ potentials. The statistical g-factors are not included in the results.

	$^1\Sigma_\mathrm{g}^+$			$^3\Sigma_\mathrm{u}^+$		
E	σ_{tot}	σ_{el}	σ_{ion}	σ_{tot}	σ_{el}	σ_{ion}
1neV	628420	26595	601825	936	0	936
10neV	204807	25107	179700	2957	0	2957
100neV	68377	20899	47478	9151	67	9084
1μeV	22078	11671	10407	18913	2557	16356
10μeV	11770	4989	6781	10827	5126	5701
100μeV	5515	2622	2893	5545	2810	2735
1meV	3574	2222	1352	3432	2105	1327

Cross sections for $^3\Sigma_\mathrm{u}^+$ state vanish for small collision energies because $J = 0$ contribution is forbidden for this symmetry (see point 4 on page 87). This property is important for cold collisions, however, observe that the vanishing of the ionization cross section is much slower than the vanishing of the elastic cross section.

In Figure 6.3 we show electron spectra for $\mathrm{He}^*(2^3\mathrm{S}) + \mathrm{He}^*(2^3\mathrm{S})$ collisions for the collision energy 1μeV. This particular energy has been chosen for checking of our calculation by comparison with the Figure 15 of the reference [99]. In the left part of the figure we show the potential difference $V_*(R) - V_+(R)$ which gives the energy of electron released at given inter-nuclear distance R in the semi-classical picture [105]. The classically forbidden region for potential $V_*(R)$ is indicated in the picture with dots. Characteristic features of the spectra can well be understood from the Figure 6.3. For both $^1\Sigma_\mathrm{g}^+ \to {}^2\Sigma_\mathrm{u}^+$ and $^1\Sigma_\mathrm{g}^+ \to {}^2\Sigma_\mathrm{g}^+$ contributions there is a maximum for electron energy just above the minimum of the difference potential. This maximum is due to large region of R where electrons contribute to a small interval in energy. The second broad maximum in the spectra corresponds to electron energies just bellow the turning point for the respective difference potential. This enhancement is due to slow motion of nuclei thus giving a larger time for the electron to escape near the turning point. Both maxima are modulated by oscillations which origin in interference phenomena. The shape of the oscillations can be understand to some extend from semi-classical calculations based on WKB [105]. Oscillations above 15.05 eV origin in discrete electron energies for associative ionization. The spectrum is convoluted with the Gaussian (FWHM=35 meV) to simulate finite electron spectrometer resolution.

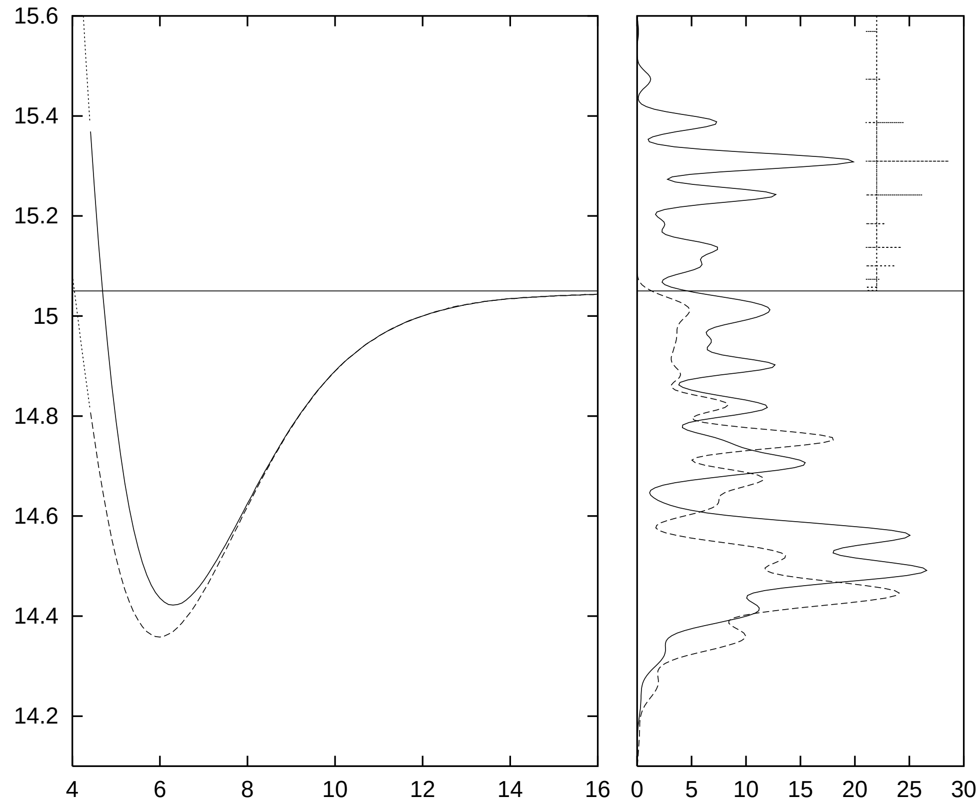

Figure 6.3: Interpretation of the electron spectra $\frac{d\sigma}{d\epsilon}$ [$1000a_0^2$/eV] (right) for the $He^*(2^3S) + He^*(2^3S)$ collisions using difference potential $V_*(R) - V_+(R)$ (left). Collision energy is 1μeV. The two curves are contributions from $^2\Sigma_u^+$ (full line) and $^2\Sigma_g^+$ (dashes) final states ($= V_+$). Only $^1\Sigma_g^+$ metastable helium molecular state ($= V_*$) is considered. The classically forbidden region is indicated with dots. The spectra are convoluted with Gaussian resolution of the electron spectrometer (FWHM=35 meV). Parts of the spectra corresponding to PI and AI are separated with horizontal line and positions of peaks due to individual final states of He_2^+ are indicated.

$He^*(2^3S) + He^*(2^3P)$ collisions

As we have emphasized in the introduction to this section we do not have complete information about all the relevant potentials to treat $He^*(2^3S) + He^*(2^3P)$ collisions. Here we present calculations for model describing only the contribution of the $^3\Sigma_g^+$ potential manifold to the collisions. We use the potentials and the couplings described in the section 6.1 (model $\mathcal{A}$ and model $\mathcal{B}$) as the Hermitian part of the local complex potential matrix (6.27). The autoionization rates $\Gamma^{(im)}$ in the expression (6.31) are not known and we have used the same values as for $^1\Sigma_g^+$ potential connected to $He^*(2^3S) + He^*(2^3S)$ asymptote. These values should be of the same order as the correct ones [99]. The calculations have been performed using the method described in the appendix C, which is the generalization for coupled channels of the method of the Chapter 3 for the solution of the Lippmann-Schwinger equation. Spectra are calculated from (6.24)-(6.25). Let us note that the points 1-4 on page 87 are valid also for the $He^*(2^3S) + He^*(2^3P)$ collisions.

We present a series of tests below to find the sensitivity to a different features of the model and to give an estimate of the uncertainty of the results.

Test 1: Non-diagonal terms in $\Gamma(R)$

As we have seen in the previous section the assumption

$$\Gamma(R) = \begin{pmatrix} \Gamma_{11}(R) & 0 & 0 \\ 0 & \Gamma_{22}(R) & 0 \\ 0 & 0 & \Gamma_{33}(R) \end{pmatrix} \tag{6.32}$$

(Γ_{ii} is the total auto-ionization width for each of the three states) is not consistent with the formula for the electron spectra (lost flux from all three channels does not give $\int d\epsilon\, d\sigma/d\epsilon$). These problems do not occur in the nonlocal treatment where the non-diagonal terms are present (see (6.31)). In the section section 6.2 we gave some arguments that the matrix Γ should look like

$$\Gamma = \begin{pmatrix} \Gamma_1 & \sqrt{\Gamma_1\Gamma_2} & \sqrt{\Gamma_1\Gamma_3} \\ \sqrt{\Gamma_2\Gamma_1} & \Gamma_2 & \sqrt{\Gamma_2\Gamma_3} \\ \sqrt{\Gamma_3\Gamma_1} & \sqrt{\Gamma_3\Gamma_2} & \Gamma_3 \end{pmatrix} \tag{6.33}$$

in the local approximation. The comparison of electron spectra for both diagonal and non-diagonal matrix Γ is shown in the Figure 6.4. The non-diagonal terms do not have a large influence on the electron spectra.

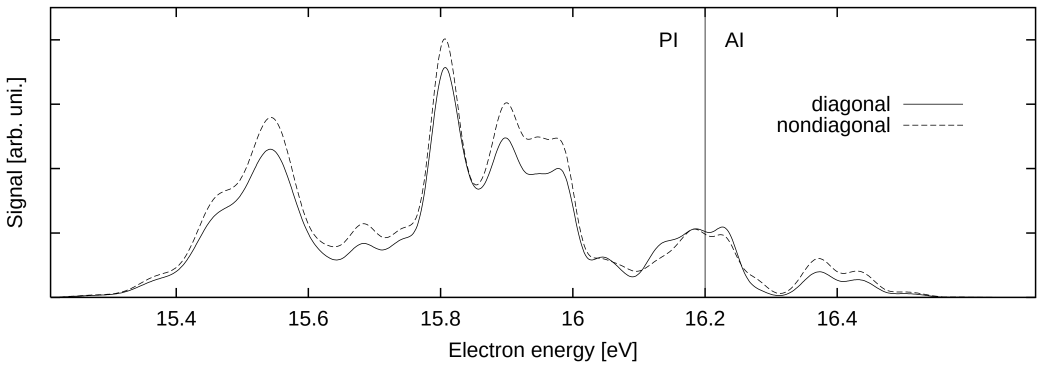

Figure 6.4: Test 1. Comparison of the spectra for diagonal and non-diagonal matrix Γ. Parts of the spectra corresponding to PI and AI are separated with vertical line as in the all following figures.

Test 2: Coupling terms $C_{12}(R)$ and $C_{13}(R)$

The coupling terms $C_{12}(R)$ and $C_{13}(R)$ can not be determined well from the *ab initio* data [99], which were constructed mainly for the calculation of $He^*(2^3S) + He^*(2^3S)$ collisions. Our algorithm for construction of the model gives accurate value of $C_{12}(R)$ only near the crossing point $R = X_2$ of $V_*^{(1)}$ and $V_*^{(2)}$ and value of $C_{13}(R)$ near the crossing point $R = X_3$ of $V_*^{(1)}$ and $V_*^{(3)}$. To estimate the influence of this uncertainty on the results we constructed two models $\mathcal{A}$ and $\mathcal{B}$ in the section one. Resulting electron spectra are depicted in the Figure 6.5. It is apparent that the effect of the coupling on the shape of the spectra is quite large. We think that the coupling for small R is overestimated with the ansats (6.11) in the model $\mathcal{A}$ leading thus to too large interference among the curves even far form crossing.

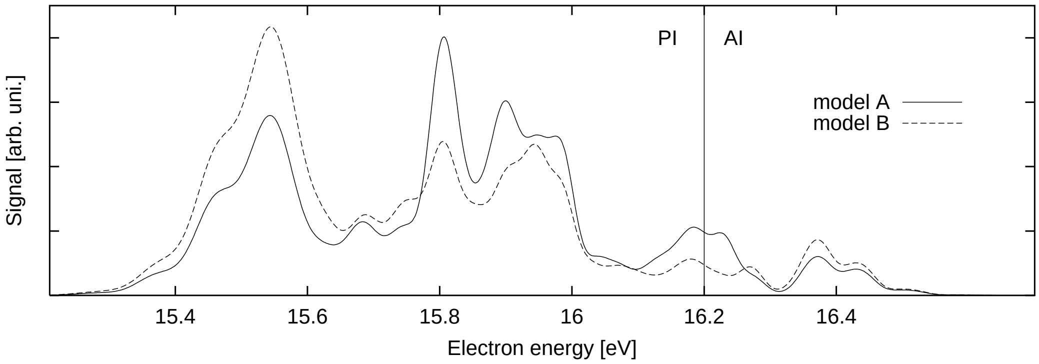

Figure 6.5: Test 2. Comparison of the spectra for the models $\mathcal{A}$ and $\mathcal{B}$.

Test 3: Sensitivity to $\Gamma_i(R)$

Individual auto-ionization widths for the states connected to $\mathrm{He}^*(2^3\mathrm{S})+\mathrm{He}^*(2^3\mathrm{S})$ asymptote are tabulated in the paper by Müller *et al.* [99]. They also calculated electron spectra for $\mathrm{He}^*(2^3\mathrm{S})+\mathrm{He}^*(2^1\mathrm{S})$ collisions using the same auto-ionization widths. Because of the lack of any *ab initio* information about the widths we have also used the same width for all three states

$$\Gamma^{(fi)}(R) = \Gamma^{(f)}(R)$$

where $\Gamma^{(f)}$ are the widths for the ${}^1\Sigma_g$ state connected to $\mathrm{He}^*(2^3\mathrm{S}) + \mathrm{He}^*(2^3\mathrm{S})$. To estimate the effect of the uncertainty in the knowledge of the widths we did another calculation for “arbitrarily” modified widths

$$\begin{aligned} \gamma^{(1)}(R) &= (1.5 - \sin(R/2))\Gamma^{(1)} \\ \gamma^{(2)}(R) &= (0.8 - 0.5\sin(R/2))\Gamma^{(2)}. \end{aligned}$$

Width $\Gamma^{(1)}$ is thus multiplied by R-dependent factor 0.5-2.5 and $\Gamma^{(2)}$ with factor 0.3-1.3. Sensitivity of the results to Γ is not large as can be seen in the Figure 6.6.

Test 4: Interference

The main goal of this chapter was to study the influence of curve crossings among several discrete states on electron spectra after the PI/AI process. Such a problem was in a simplified manner addressed by Müller et al [99] for $\mathrm{He}^*(2^3\mathrm{S})+\mathrm{He}^*(2^1\mathrm{S})$

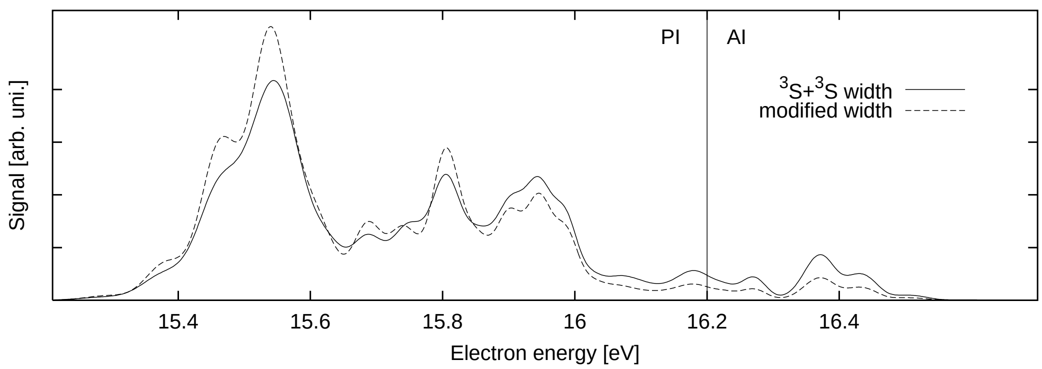

Figure 6.6: Test 3. Influence of the modification of auto-ionization width Γ.

collisions. To deal with the curve crossings they used the Landau-Zener probability as weighting factor for contributions from the two potentials neglecting thus interference effects. To see what is the effect of the neglection of the interference in our calculation we calculated the spectra using the expression $\sum |T^{(fi)}|^2$ instead of $|\sum T^{(fi)}|^2$ in the formula for the electron spectra. Figures 6.7a,b show the contributions from the each term $|T^{(fi)}|^2$ and the comparison of the coherent and non-coherent sum is shown in the third plot 6.7c. Note that the character of each contribution in Fig 6.7a,b is very similar to the character of the spectra for the model of one state interacting with one continuum studied in the previous paragraph and some of the features are easily understood from similar semi-classical discussion. Interference among the contributions is apparent from the Figure 6.7c. It is clear that the neglection of the interference gives final spectra of a quite different character.

6.4 Conclusions

We have developed a new method for solving of integral scattering equations in the presence of several complex coupled potentials (see Appendix C) and applied it to calculation of energy-spectra for electron released in Penning ionization in He*(2^{3}S) + He*(2^{3}P) collisions. Only three crossing $^3\Sigma_{\rm g}^+$ potentials have been taken into account. No information about potentials for other auto-ionizing metastable molecular states ($^1\Sigma_{\rm u,g}^+$, $^3\Sigma_{\rm u}^+$, $^1\Pi_{u,g}$, $^3\Pi_{u,g}$) is available. Some of them may be repulsive and thus not so important for low-energy collisions. Test calculations show that proper coherent summation of contributions from all crossing $^3\Sigma_{\rm g}^+$ metastable states is necessary to obtain correct result for electron spectra. More information about all potentials and also about the direct couplings between crossing metastable states is important for the correct prediction of the spectra. The spectra are not so sensitive to exact behavior of the auto-ionization width.

It is quite easy to translate the electron spectra into the time-of-flight spectra for the ions, thanks to conservation of energy. Recent experiments of the Utrecht group [106] show the spectra consistent with our calculations. Fine details are

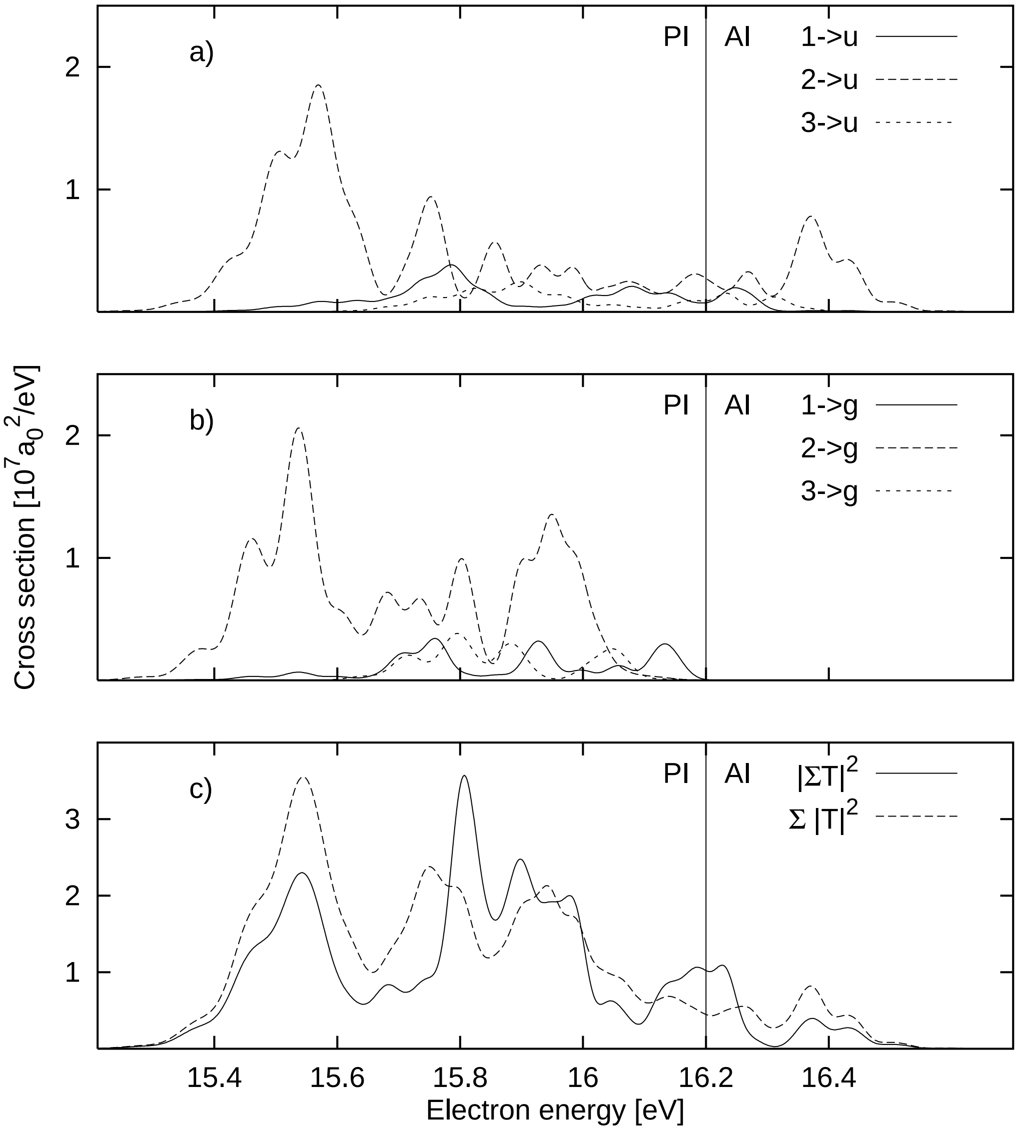

Figure 6.7: Test 4. Coherence effects.

not seen in the experiments but it is likely that the experiment can resolve larger differences like that resulting from the comparison of the model $\mathcal{A}$ and $\mathcal{B}$. However, as we have stressed above, more detailed calculation is necessary for direct comparison with experiments.

Chapter 7

Concluding remarks

The main objective of this work—to apply the nonlocal resonance description to associative detachment of negative ions—has been successfully fulfilled. In the course to meet this goal we had to revise the old work of Bieniek [10] describing the expansion of resonance wave function into partial waves. We extended his work to include also the electron-diatomic-molecule collisions (DA and VE), since rotations have not been included in the previous treatment of nonlocal resonance dynamics (see the review [4]). We did not remove the simplifying assumption that the projection of the angular momentum of electrons on the internuclear axis remains unchanged after the resonance process. This assumption is fulfilled for all processes investigated in this work since only Σ states of diatomic molecules and molecular ions are involved.

Special attention has been payed to generalization of numerical procedures (Schwinger-Lanczos algorithm [31]) previously used to calculate cross sections resulting from the nonlocal resonance dynamics. Only small changes were required to include the rotational degrees of freedom by means of partial wave expansion, however, since the computational expenses increased substantially we had to optimize carefully all the numerical procedures.

In our application to concrete examples of low-energy inelastic collisions we could build on previous extensive work of Domcke and collaborators, who constructed nonlocal resonance models for a number of interesting systems. Nevertheless the treatment of negative-ion-atom collisions in low energy region required careful revision of long range part of the ion-atom interaction. Building thus new models for several systems we found that even cross sections for electron-molecule collisions are sensitive to this part of the interaction. We thus, together with a new calculation of the associative detachment cross sections in nonlocal resonance model, also revised previously published results for dissociative attachment and vibrational excitation in electron-molecule collisions. Inclusion of the rotational degrees of freedom makes possible the direct comparison with experiments, since the molecules colliding with electrons can be considered rotationally hot in the calculation. We would like to stress that all the processes have been (for each system) calculated within single model containing no adjustable semiempirical parameters and compared with experiments.

In the second part of the thesis the applications of our treatment are discussed. The most detailed discussion follows the calculation for $H_2 + e^-$ and

HCl+e^-. We would like to stress that our calculation is the first resonance treatment of the associative detachment with full account of the complexity of the nonlocal dynamics. In the case of H_2 the performance of the local complex approximation has been tested. This approximation was previously used to describe both ion-atom and electron-molecule collisions. In contrast to electron-molecule scattering we found that our new nonlocal calculation agrees quite well with the local one. Reason is found to be the population of highly excited states of H_2 after the detachment process. Cross sections for these states are less sensitive to the details of the model then for ground and low-excited states, which are involved in electron-molecule collisions. We found factor of three discrepancy of our low-energy associative detachment rate in comparison with experiment. Note, however, that the uncertainty of the experimental value is believed to be a factor of two. Discrepancy with experiment has also been found for the dissociative attachment unless systematic error (~20%) in experimental temperature is assumed (see also discussion for HCl). The same holds for comparison of dissociative attachment of electron to hot D_2 molecules. Further improvements of the model are also possible within nonlocal resonance formalism. In the case of H_2^- system there are two resonance states, which go asymptotically to H+H$^-$ state as the internuclear separation R goes to infinity. In our model only the state which is attractive at long range is considered. For the energies in the range of several 100 meV the second state might also be important.

In the case of HCl we found a good agreement with the experiments for the total associative detachment cross section in the collision energy range 0.7-3eV and also for vibrational excitations $0 \to 1$, $0 \to 2$,...,$0 \to 4$. Even minute details of the threshold peaks in $0 \to 1$ and $0 \to 2$ cross sections are reproduced. Unprecedented agreement with experiments for dissociative attachment of electron to hot HCl molecules is obtained if the same shift of experimental temperature as for H_2 is accepted. In the study of the H+Cl$^-$ collisions we have payed a special attention to the details of the dynamics since our calculation reveals threshold structures not predicted before for the AD process, related to opening of new channels. These structures can not be understood in the framework of the local complex approximation. Drop in the total detachment probability in the vicinity of a new threshold is observed in the calculation. Threshold structures (Wigner cusps) are also predicted in the spectrum of an electron released in the detachment. Important property of these cusps is that they are not smeared out by broad collision energy distribution in the initial H+Cl$^-$ channel. Since the position of the cusp is insensitive to collision energy, the broad distribution even enhances the effect. Measurement of the electron spectra would provide similar information as dissociative attachment to hot molecules, but from a different view. Further improvement of the model within the nonlocal resonance formalism is possible as is discussed in the section 5.1.

A further insight into the dynamics of the resonant collisions is still needed. Despite of two decades of theoretical effort the nature of the threshold peaks in VE cross sections is still not clearly understood. The newly discovered phenomenon of oscillations in VE cross sections under DA threshold has also not been fully comprehended although our calculations prove that they are closely related to the shape of the long range part of the potential of negative molecular ion formed in the electron molecule collision and it is clear that these structures are caused by some kind of resonance. In principle exact nonlocal resonance description is a good tool for deeper understanding of the processes. Its advantage over close-coupling or R-matrix calculations is its clarity and possibility to visualize simply the resonance wave functions. Sequence of the molecules H_2, HF, HCl, HBr, HI represents, in terms of electron-molecule collisions, a sequence of similar models with varying parameters and its investigation will deepen our understanding of the nonlocal dynamics. In this work we have only briefly presented some preliminary results for HF and HBr. In future we would like to study these systems in more details and to compare with new experiments.

Further possibilities for future work lie in the generalization of the nonlocal resonance model to describe more complicated molecules or to include more discrete states and more continua. First step in this direction has already been made in the previous chapter. Here we investigated the process of ionization of metastable helium atoms similar to associative detachment. Also the description of the process within the resonance model is very similar. We prepared numerical procedures to treat the problem within the local-complex-potential approximation. This approximation is known to work well in the case of Penning ionization, where the potential curves for resonance and the final system are well separated in energy. On the other hand the solution of the local problem is the necessary first step towards generalization of our nonlocal subroutines to this more complicated case. Results presented in the Chapter 6 should be regarded as illustrative more than prediction for real physical output of experiments because of lack of *ab initio* data to build reliable models. Nevertheless, the resulting electron spectra are in reasonable qualitative agreement with preliminary data from experiments carried out at Utrecht university.

Appendix A

Angular momentum

In this appendix we show few relations and formulae for spherical harmonics and Wigner 3J symbols employing the conventions of Edmonds [107].

Spherical harmonic with $m = 0$ can be written in terms of Legendre polynomial

$$Y_{l0} = \sqrt{\frac{2l+1}{4\pi}} P_l(\cos\theta). \tag{A.1}$$

Other useful relation between Lagendre polynomials and spherical harmonics is:

$$\frac{2l+1}{4\pi} P_l(\hat{a}\cdot\hat{b}) = \sum_{m=-l}^{l} Y_{lm}(\hat{a}) Y^*_{lm}(\hat{b}). \tag{A.2}$$

Complex conjugation of a spherical harmonic can be performed with

$$Y^*_{lm}(\hat{n}) = (-1)^m Y_{l-m}(\hat{n}), \tag{A.3}$$

and the integral of product of three harmonics is

$$\begin{aligned} &\int \mathrm{d}\hat{n} Y_{l_1 m_1}(\hat{n}) Y_{l_2 m_2}(\hat{n}) Y_{l_3 m_3}(\hat{n}) \\ &\quad = \frac{(2l_1+1)(2l_2+1)(2l_3+1)}{4\pi} \begin{pmatrix} l_1 & l_2 & l_3 \\ 0 & 0 & 0 \end{pmatrix} \begin{pmatrix} l_1 & l_2 & l_3 \\ m_1 & m_2 & m_3 \end{pmatrix} . \end{aligned} \tag{A.4}$$

Wigner 3J symbols satisfy the orthogonality relations

$$\sum_{m_1 m_2} \begin{pmatrix} l_1 & l_2 & J \\ m_1 & m_2 & M \end{pmatrix} \begin{pmatrix} l_1 & l_2 & J' \\ m_1 & m_2 & M' \end{pmatrix} = \frac{1}{2J+1} \delta_{JJ'} \delta_{MM'} \delta(l_1, l_2, J). \tag{A.5}$$

Wigner 3J symbols can easily be evaluated in some special cases, for example

$$\begin{pmatrix} 0 & J' & J \\ 0 & 0 & 0 \end{pmatrix} = (-1)^J \delta_{JJ'} / \sqrt{2J+1}, \tag{A.6}$$

$$\begin{pmatrix} J & J' & 0 \\ M & -M' & 0 \end{pmatrix} = (-1)^{J-M} \delta_{JJ'} \delta_{MM'} / \sqrt{2J+1} \tag{A.7}$$

and

$$\begin{aligned} \begin{pmatrix} J_1 & J_2 & J_3 \\ 0 & 0 & 0 \end{pmatrix} &= (-1)^{J/2} \left[\frac{(J-2J_1)!(J-2J_2)!(J-2J_3)!}{(J+1)!} \right]^{\frac{1}{2}} \times \\ &\times \frac{(J/2)!}{(J/2-J_1)!(J/2-J_2)!(J/2-J_3)!} \end{aligned} \tag{A.8}$$

for $J = J_1 + J_2 + J_3$ even and it is zero for J odd.

Appendix B

Description of the models

We describe the models used in the previous chapters in details in this appendix. All the numerical values are given in a. u. unless stated otherwise in the text.

In all the models (except HF) it is possible to calculate

$$\Delta(\epsilon) = \wp \int \mathrm{d}\epsilon' |V_{\mathrm{d}\epsilon'}|^2/(\epsilon - \epsilon') \tag{B.1}$$

analytically using the formula (see [67])

$$\int \frac{x^\alpha e^{-\beta x}}{\epsilon - x} \mathrm{d}x = \begin{cases} -\Gamma(1+\alpha)(-\epsilon)^\alpha \Gamma(-\alpha, -\beta\epsilon) e^{-\beta\epsilon} & \epsilon < 0, \\ \epsilon^\alpha e^{-\beta\epsilon} [\pi \cot \alpha\pi - \Gamma(\alpha)(\beta\epsilon)_1^{-\alpha} F_1(-\alpha, 1-\alpha; \beta\epsilon)] & \epsilon > 0, \end{cases} \tag{B.2}$$

where $\Gamma(\alpha, x)$ is the incomplete gamma function and ${}_1F_1(a, b, x)$ is the confluent hypergeometric function. These functions are conveniently evaluated via continued fraction [108, p.263]

$$\Gamma(\alpha, x) = e^{-x} x^\alpha \left(\frac{1}{x+} \frac{1-\alpha}{1+} \frac{1}{x+} \frac{2-\alpha}{1+} \frac{2}{x+} \cdots \right) \tag{B.3}$$

and a series expansion [108, p.504]

$${}_1F_1(a, b, x) = 1 + \frac{ax}{b} + \frac{a(a+1)}{b(b+1)} \cdot \frac{x^2}{2!} + \frac{a(a+1)(a+2)}{b(b+1)(b+2)} \cdot \frac{x^3}{3!} + \cdots \tag{B.4}$$

B.1 Models for H_2^- $^2\Sigma_u^+$ resonance

In the construction of our new model we have started from the model of Mündel, Berman, Domcke (MBD) [6] constructed from their "fixed-R" ab initio electron-molecule scattering calculations. The function $V_0(R)$ in the MBD model is constructed as the spline interpolation of the data of Kołos and Wolniewicz [55]. The other model functions are given by

$$V_\mathrm{d}(R) = D_1 \left\{ e^{-2\alpha_1(R-R_1)} - 2te^{-\alpha_1(R-R_1)} \right\} + Q, \tag{B.5}$$

$$V_{\mathrm{d}\epsilon}(R) = \frac{1}{\sqrt{2\pi}} \sum_{i=1}^{3} f_i(\epsilon) g_i(R), \tag{B.6}$$

where

$$\begin{aligned} f_i(\epsilon) &= A_i \epsilon^{\frac{\alpha}{2}} e^{B_i \epsilon} & i=1,2,3 && \text{(B.7)} \\ g_i(R) &= \exp(-C_i^2 (R-R_0)^2) & i=1,2 && \text{(B.8)} \\ g_3(R) &= \exp(-C_3(R-R_0)). & && \text{(B.9)} \end{aligned}$$

The threshold exponent $\alpha = \frac{3}{2}$ in the equation (B.7) is determined by the threshold law of Wigner for p-wave electron-molecule scattering [4]—see also (2.83). The values of the other constants are given in the following table

A_1= 1.6618	A_2=1.3603	A_3=1.0467
B_1=18.863	B_2=4.6559	B_3=1.4504
C_1= 0.0	C_2=0.3302	C_3=0.489
D_1= 0.06247	α_1=1.19	t=0.0

The equilibrium distance of the nuclei in the H_2 molecule is $R_0 = 1.4014$ a. u. [55].

New model

We have constructed a new model changing the $V_{\rm d}(R)$ of the MBD model to account for the long range behaviour of the H_2^- bound state Senekowitsch et al. [57] (see the section 4.3 for the details). The resulting potential is

$$V_d(R) = \begin{cases} 1.74e^{-2.37R} - \frac{94.4e^{-22.5/R}}{((R-2.54)^2+3.11)^2} & \text{for } R \le 10.6 \\ -0.00845Re^{-0.35R} - \frac{2.25}{R^4} - \frac{97}{R^6} & \text{for } R > 10.6 \end{cases} \quad \text{(B.10)}$$

We have also found the value $C_1 = 0$ unphysical since $V_{\rm d\epsilon}(R)$ does no vanish with $R \to \infty$. The value was obtained from the best fit of electron-molecule scattering data for $R = 1.4 - 2.75$ like the other parameters, but the quality of the fit is not deteriorated when C_1 is slightly increased. At the same time the results for calculation of the nuclear dynamics are not sensitive to this small increase of C_1 if the potential $V_{\rm d}(R)$ is also changed at the same time to be consistent with the data for H_2^- bound state. We set $C_1 = 0.2$ in the final model.

Values of the reduced mass are

$$2\mu = 1.008\,\text{a.m.u.} = 1837.47\,\text{a.u.}$$

for H_2 and

$$2\mu = 2.01410\,\text{a.m.u.} = 3671.48\,\text{a.u.}$$

for D_2.

B.2 Models for the HCl^- $^2\Sigma^+$ resonance

In the original model of Domcke and Mündel [67] the potential for the neutral HCl molecule is assumed to be

$$V_0(R) = 0.169414e^{-1.002(R-R_0)}(\mathrm{e}^{-1.002(R-R_0)} - 2) + Q_0. \quad \text{(B.11)}$$

The free parameters in the Morse form of the function were derived from spectroscopic data [67]. The equilibrium distance in HCl is $R_0 = 2.409$ and the electron affinity of Cl is

$$Q_0 = 3.605\,\mathrm{eV} \doteq 0.132481\,\mathrm{a.u.}$$

The discrete state potential $V_\mathrm{d}(R)$ and the coupling $V_{\mathrm{d}\epsilon}(R)$ derived from the fixed-nuclei electron-molecule scattering calculation of Padial and Norcross [80] read

$$V_\mathrm{d}(R) = 0.08636.e^{-1.746(R-R_0)}, \tag{B.12}$$

$$V_{\mathrm{d}\epsilon} = a\left(\frac{\epsilon}{b}\right)^{\alpha/2} e^{-\epsilon/2b} g(R), \tag{B.13}$$

with $a = 0.428785$, $b = 0.199732$ and

$$g(R) = \begin{cases} e^{-0.031(R-R_0)} & R < 3 = R_1, \\ e^{-0.031(R-R_0)}e^{-0.78(R-R_1)} & R > R_1. \end{cases} \tag{B.14}$$

DMH model

The threshold exponent α determines the behavior of the coupling $V_{\mathrm{d}\epsilon}(R)$ at low energies. Its value for given R depends on the electric dipole of the neutral molecule. The dependence on R was neglected in the DM model. We investigated the influence of the R-dependence of this quantity using the functions $V_0(R)$, $V_\mathrm{d}(R)$ and $V_{\mathrm{d}\epsilon}(R)$ from the previous model, but with the threshold exponent $\alpha(R)$ given by the following interpolation formula [83]

$$\alpha(R) = \tfrac{1}{2} + a_1M^2 + a_2M^4 + a_3M^6 + a_4M^8, \tag{B.15}$$

with

$$M(R) = M_0(1+R)^3(1+\textstyle\sum e_iR^i)^{-1}. \tag{B.16}$$

The parameters a_i, e_i and M_0 are collected in the following table

$a_1 = -0.0101157$	M_0=1.09333	e_4= 1.829
$a_2 = -0.14833$	e_1=1.897	e_5=−4.137
$a_3 = -0.07486$	e_2=0.871	e_6= 13.886
$a_4 = -0.03735$	e_3=1.465	e_7= 0.416.

The dependence of the dipole moment of the HCl molecule on the internuclear distance is thus taken into account.

DMHC-2 model

In the final model we have also taken the *ab initio* data for HCl^- into account, which results in modification of the $V_\mathrm{d}(R)$. The resulting function consistent with both the molecular anion potential data and the *ab initio* electron-molecule scattering data is given by the formula

$$\begin{aligned} V_d(R) &= 0.086361\mathrm{e}^{-1.74628(R-R_0)} - \\ &\quad - \frac{2.25}{((R-3.5)^2+51.37)^2-2500} \end{aligned} \tag{B.17}$$

The function $g(R)$ was modified in order to remove the kink at $R = 3$

$$g(R) = 1.07758(1 - 0.03101R)(1 + \mathrm{e}^{4.2(R-3.28)})^{-1}. \tag{B.18}$$

B.3 Model for the HF$^-$

The functions needed for calculation of the nuclear dynamics are taken from the calculation of Gallup, Xu and Fabricant [52]

$$\begin{aligned} V_0(R) &= 0.2252 \cdot e^{-1.1735(R-R_0)}\left[e^{-1.1735(R-R_0)} - 2\right] + Q_0, && \text{(B.19)} \\ V_\mathrm{d}(R) &= 0.03307e^{-3.7276(R-R_0)}, && \text{(B.20)} \\ \Gamma(R,\epsilon) &= \Gamma(\epsilon)g(R)^2, && \text{(B.21)} \\ \Delta R,\epsilon &= \Delta(\epsilon)g(R)^2. && \text{(B.22)} \end{aligned}$$

The energy and the R-dependence of the width and level shift were parametrized as follows:

$$\begin{aligned} g(R) &= 1.31e^{-0.1233(R-0.25)^2}, && \text{(B.23)} \\ \Gamma(\epsilon) &= 0.0169 + 0.537\epsilon^{0.511}e^{-1.113\epsilon}, && \text{(B.24)} \\ \Delta(\epsilon) &= \begin{cases} -0.2016 + 0.2(0.00106 - \epsilon)^{0.131} & \epsilon < 0 \\ -0.1115 + 0.3882\epsilon 0.008555e^{-118.7\epsilon} & \epsilon > 0 \end{cases} && \text{(B.25)} \end{aligned}$$

The equilibrium distance in HF is $R_0 = 1.732517$ and the electron affinity to F is 0.125. After taking the *ab initio* data for HF$^-$ of Piecuch [94] into account we had to modify the discrete state potential for $2.4 < R < 4.9$ as follows

$$V_\mathrm{d}(R) = 5.2615 \times 10^{-2} - 3.2915 \times 10^{-2}R + 5.7226 \times 10^{-3}R^2 - 2.7739 \times 10^{-4}R^3. \tag{B.26}$$

For $R < 2.4$ we used the original form B.20 and polarization potential $-2.25/R^4$ for $R > 4.9$. We used the value $2\mu = 2\,\text{a.m.u.} = 3645.8\,\text{a.u.}$ for the reduced mass in the calculation.

B.4 Model for the HBr$^-$

For the sake of completeness we give also the functions for the model of HBr constructed by Horáček and Domcke [32]:

$$\begin{aligned} V_0(R) &= 0.1441 \cdot e^{-0.96(R-R_0)}\left[e^{-0.96(R-R_0)} - 2\right] + Q_0, && \text{(B.27)} \\ V_\mathrm{d}(R) &= 0.0638e^{-1.9742(R-R_0)}, && \text{(B.28)} \end{aligned}$$

with $R_0 = 2.67$, $Q_0 = 0.12348$ and the reduced mass $\mu = 0.99558\,\text{a.m.u.}$ Further more

$$\begin{aligned} \Gamma(R,\epsilon) &= \Gamma(\epsilon)g(R)^2, && \text{(B.29)} \\ \Gamma(\epsilon) &= 0.3145\epsilon^{0.424}e^{-5.896\epsilon}, && \text{(B.30)} \\ g(R) &= \begin{cases} e^{-0.1176(R-R_0)} & R < 2.9 = R_1, \\ e^{-0.1176(R-R_0)}e^{-0.4(R-R_1)} & R > R_1. \end{cases} && \text{(B.31)} \end{aligned}$$

Appendix C

Scattering in complex potential

In this appendix we give a short account of formulae used to calculate cross section for scattering processes in a complex potential. We will start with the case of single complex potential; the case of several coupled states follows in the next section.

Single complex potential

The wave function[1] $\psi(R)$ is the unique solution of the Lippmann-Schwinger equation

$$\psi(R) = u(E,R) + \int_0^\infty dR'\, G(E,R,R')\, W(R')\, \psi(R'), \tag{C.1}$$

where we have introduced the complex potential $W(R) = V(R) - \frac{i}{2}\Gamma(R)$ and

$$\begin{aligned} G(E,R,R') &= -\frac{2\mu}{K} u(E,R_<) v(E,R_>), && \text{(C.2)} \\ u(E,R) &= KR j_J(KR), && \text{(C.3)} \\ v(E,R) &= iKR h_J(KR). && \text{(C.4)} \end{aligned}$$

With $R_>$ and $R_<$ we denoted larger and smaller of R and R' respectively and $j_J(z)$, $h_J(z)$ denote the spherical Bessel and Hankel functions respectively. Equation (C.1) fixes both the boundary condition and the normalization

$$\int_0^\infty dR\, \psi(E,R)\, \psi(E',R) = \int_0^\infty dR\, u(E,R)\, u(E',R) = \frac{\pi}{2}\delta(K-K'). \tag{C.5}$$

Usual energy normalized wave function $\bar{\psi}_E$ and K-normalized $\bar{\psi}_K$ are related to this function

$$\bar{\psi}_K = e^{-i\gamma}\sqrt{2/\pi}\,\psi, \qquad \bar{\psi}_E = e^{-i\gamma}\sqrt{2\mu/\pi K}\,\psi \tag{C.6}$$

where $\gamma = \delta + i\eta$ is (complex) phase shift defined by asymptotic condition

$$\psi(R) \underset{R\to\infty}{\longrightarrow} e^{-i\gamma} \sin(KR - \tfrac{\pi}{2}J + \gamma). \tag{C.7}$$

If we define scattering amplitude

$$a_J = -\frac{2\mu}{K}\int_0^\infty dR\, u_J(E,R)\, W(R)\, \psi_J(E,R) \equiv -\frac{2\mu}{K}\langle u|W\psi\rangle \tag{C.8}$$

[1] We will suppress indexes J and $*$ whenever it will be possible without confusion.

then it is possible to show that

$$a_J = e^{i\gamma} \sin \gamma = \frac{i}{2}(1 - e^{2i\gamma}) \tag{C.9}$$

and the angle integrated elastic cross section is

$$\sigma_{\rm el} = \frac{4\pi}{K^2} \sum_J (2J+1)|a_J|^2 = \frac{4\pi}{E^2} \sum_J (2J+1)|\langle u|W\psi\rangle|^2 \tag{C.10}$$

or

$$\sigma_{\rm el} = \frac{\pi}{K^2} \sum_J (2J+1) \left[1 - e^{-4\eta} - 2e^{-2\eta}\cos 2\delta\right]. \tag{C.11}$$

Inelastic cross section which is, in our case the ionization cross section, reads

$$\sigma_{\rm ion} = \frac{\pi}{K^2} \sum_J (2J+1) \left[1 - e^{-4\eta}\right] \tag{C.12}$$

or

$$\sigma_{\rm ion} = \frac{4\pi}{K^2} \sum_J (2J+1) \left[\mathrm{Im}\, a_J - |a_J|^2\right] = \sigma_{\rm tot} - \sigma_{\rm el}, \tag{C.13}$$

where total scattering cross section $\sigma_{\rm tot}$ is

$$\sigma_{\rm tot} = \frac{4\pi}{K^2} \sum_J (2J+1)\mathrm{Im}\, a_J = \frac{2\pi}{K^2} \sum_J (2J+1) \left[1 - e^{-2\eta}\cos 2\delta\right]. \tag{C.14}$$

Ionization cross section can also be found from an independent formula

$$\sigma_{\rm ion} = \frac{2\pi}{EK} \sum_J (2J+1)\langle\psi|\Gamma|\psi\rangle \tag{C.15}$$

which may serve as cross check for numerical results. Let us note that the Γ is in general defined as the antihermitian part of W, i. e. $\Gamma = i(W - W^+)$.

Several coupled states

Lippmann-Schwinger equation (C.1) in the case of several coupled channels reads

$$\psi_m^{(c)}(R) = \delta_{mc} u(E_m, R) + \int_0^\infty dR'\, G(E_m, R, R') \sum_n W_{mn}(R')\, \psi_n^{(c)}(R'), \tag{C.16}$$

where subscripts m, n denote components of the wave function and superscript (c) indicates in which channel the particles originally come to each other. Let us note that the potential matrix W_{mn} contains also the imaginary part and that this matrix should vanish at infinity. In particular the diagonal terms has to be shifted

$$W_{mm}(R) = V_m(R) - \tfrac{i}{2}\Gamma_m(R) - V_m(\infty) \tag{C.17}$$

and the channel energies E_m are defined as $E_m = E - V_m(\infty)$, where E is the total energy conserved in the scattering process. For closed channels $E_m < 0$ and the wave number K_m needed for calculation of G and u (equations (C.2)-(C.4)) is defined as $K_m = i\sqrt{|2\mu E|}$. If we introduce the vector $\Psi^{(c)}(R)$ with the components $\psi_m^{(c)}(R)$, the vector $\Phi^{(c)}(R)$ with all components being zero except $\phi_m^{(c)}(R) = u(E_m, R)$ and the matrix $\mathcal{W}$ then the equation (C.16) may simply be written as

$$|\Psi^{(c)}\rangle = |\Phi^{(c)}\rangle + \mathcal{G}(E)\mathcal{W}|\Psi^{(c)}\rangle, \tag{C.18}$$

where we have employed bracket notation for the integration over R. The expression $\mathcal{G}\mathcal{W}|\Psi^{(c)}\rangle$ thus contains both the integration and the matrix multiplication. Quantity $\mathcal{G}_{mm}$ is diagonal matrix with elements $\mathcal{G}_{mm} = G(E_m, R, R')$. Let us define the scattering amplitude

$$a_m^{(c)} = -\frac{2\mu}{\sqrt{K_c K_m}} \int_0^\infty dR\, u(E_m, R) \sum_n W_{mn}(R)\, \psi_m^{(c)}(R) \equiv -\frac{2\mu}{\sqrt{K_c K_m}} \langle \Phi^{(m)} | \mathcal{W} \Psi^{(c)} \rangle. \tag{C.19}$$

Cross section for the scattering process starting in the channel c and ending in c' is

$$\sigma_{c\to c'} = \frac{4\pi}{K_c^2} \sum_J (2J+1) |a_{c'}^{(c)}|^2 = \frac{4\pi}{E_c^2} \sum_J (2J+1) |\langle \Phi^{(c')} | \mathcal{W} \Psi^{(c)} \rangle|^2 \tag{C.20}$$

For $c = c'$ the quantity $\sigma_{c\to c}$ gives (angle integrated) elastic cross section. The total cross section for an inelastic process reads

$$\sigma_{\text{inel}} = \frac{4\pi}{K_c^2} \sum_J (2J+1) \left[\text{Im}\, a_c^{(c)} - |a_c^{(c)}|^2 \right] = \sigma_{\text{tot}}^{(c)} - \sigma_{c\to c}, \tag{C.21}$$

where

$$\sigma_{\text{tot}}^{(c)} = \frac{4\pi}{K_c^2} \sum_J (2J+1) \text{Im}\, a_c^{(c)} \tag{C.22}$$

is the total scattering cross section in the potential $\mathcal{W}$. The cross section for ionization (absorption by non-Hermitian part of the potential) is given by

$$\sigma_{\text{ion}}^{(c)} = \sigma_{\text{tot}}^{(c)} - \sum_{c'} \sigma_{c\to c'} = \frac{4\pi}{K_c^2} \sum_J (2J+1) \sum_{c'} \left[\delta_{cc'} \text{Im}\, a_{c'}^{(c)} - |a_{c'}^{(c)}|^2 \right]. \tag{C.23}$$

The sum is performed over all opened channels c'. An alternative formula for absorption cross section in the potential $\mathcal{W}$ is

$$\sigma_{\text{ion}}^{(c)} = \frac{2\pi}{K_c E_c} \sum_J (2J+1) \langle \Psi^{(c)} | \Gamma | \Psi^{(c)} \rangle, \tag{C.24}$$

with $\Gamma \equiv i[\mathcal{W} - \mathcal{W}^+]$. Some of the formulae given above can be rewritten in simpler form using the S-matrix

$$S_{cc'} = \delta_{cc'} + 2i a_{c'}^{(c)}, \tag{C.25}$$

which is not unitary for $\mathcal{W} \neq \mathcal{W}^+$. Like in the case of one state the S-matrix and the scattering amplitude can also be found from asymptotic behavior of the wave function $\psi_m^{(c)}(R)$ for $R \to \infty$.

C.1 Solution of the Lippmann-Schwinger equation for coupled channels

The Lippmann-Schwinger equation (C.1) can be solved using the method described in detail in [27] which is based on a transformation of the integral equation into the equation of Volterra type. The method was outlined briefly in the section 3.1 and generalized for finding of the irregular solution needed for the construction of Green function. In the following we generalize the method for several coupled states (C.16). The advantage of solving the integral equation instead of traditional description by differential equations is that the boundary conditions for the problem are already incorporated into integral equation and need not be added separately as in case of differential equations. Furthermore the integral equations are more suitable for solution of problems involving nonlocal potentials. A disadvantage is that the spherical Bessel functions are needed at many points and in the case of coupled states we need the Bessel functions of the complex argument for the closed channels.

Like in the section 3.1 the equation (C.16) can be rearranged into the form

$$\begin{aligned}\psi_m^{(c)}(R) = &\left[\delta_{mc} - \frac{2\mu}{K_m}\int_0^\infty dR' v(E_m,R') \sum_n W_{mn}(R')\,\psi_n^{(c)}(R')\right] u(E_m,R) - \\ &- \frac{2\mu}{K_m}\int_0^R dR' \; [v(E_m,R)u(E_m,R') - u(E_m,R)v(E_m,R')] \sum_n W_{mn}(R')\,\psi_n^{(c)}(R').\end{aligned} \tag{C.26}$$

It is obvious that if we define $f_m^{(c)}$ being the unique solution of the equation

$$\begin{aligned}f_m^{(c)}(R) = &\delta_{mc} u(E_m,R) - \\ &- \frac{2\mu}{K_m}\int_0^R dR' \; [v(E_m,R)u(E_m,R') - u(E_m,R)v(E_m,R')] \sum_n W_{mn}(R')\, f_n^{(c)}(R')\end{aligned} \tag{C.27}$$

and

$$B_{cm} = -\frac{2\mu}{K_m}\int_0^\infty dR' v(E_m,R') \sum_n W_{mn}(R')\,\psi_n^{(c)}(R') \tag{C.28}$$

then it is

$$\psi_m^{(c)}(R) = \sum_{c'} (\delta_{cc'} + B_{cc'})\, f_m^{(c')}(R). \tag{C.29}$$

Introducing integrals

$$\alpha_{cm}(R) = -\frac{2\mu}{K_m}\int_0^R \mathrm{d}R' u(E_m,R') \sum_n W_{mn}(R') f_n^{(c)}(R'), \tag{C.30}$$

$$\beta_{cm}(R) = -\frac{2\mu}{K_m}\int_0^R \mathrm{d}R' v(E_m,R') \sum_n W_{mn}(R') f_n^{(c)}(R'), \tag{C.31}$$

in analogy with the case of one state, we can rewrite the equation (C.27) in the form

$$f_m^{(c)} = (\delta_{cm} - \beta_{cm}(R)) u(E_m,R) + \alpha_{cm}(R) v(E_m,R). \tag{C.32}$$

The matrix B can be expressed in terms of the matrix $\beta \equiv \beta(\infty)$

$$B = \beta(1-\beta)^{-1}. \tag{C.33}$$

It follows that the original wave function $\psi_m^{(c)}$ is

$$\psi_m^{(c)}(R) = \sum_{c'} (1-\beta)^{-1}_{cc'} \, f_m^{(c')}(R) \tag{C.34}$$

and the scattering amplitude $a_m^{(c)}$ is ($\alpha \equiv \alpha(\infty)$)

$$a_m^{(c)} = \sqrt{\frac{K_m}{K_c}} \sum_{c'} (1-\beta)^{-1}_{cc'} \, \alpha_{c'm}. \tag{C.35}$$

The equation (C.32) can be used to calculate the functions $f_m^{(c)}$ on a grid starting from the boundary condition near $R = 0$ in the same way as in the section 3.1. The functions $f_m^{(c)}$ are finally renormalized using the relation (C.34) to obtain the wave function $\Psi^{(c)}$. A few notes are necessary concerning the numerical properties of the outlined algorithm. The algorithm becomes numerically unstable if $E_m \ll 0$ for some m. Sometimes we can avoid these difficulties starting integration at sufficiently large R (if the problem appears near origin) or not considering the closed channel which causes the problem. General solution for the problem is to perform the renormalization

$$f_m^{(c)} \;\rightarrow\; \sum_{c'} [1-\beta(R_0)]^{-1}_{cc'} f_m^{(c')}(R_0) \tag{C.36}$$

$$\alpha_{cm}(R_0) \;\rightarrow\; \sum_{c'} [1-\beta(R_0)]^{-1}_{cc'} \alpha_{c'm}(R_0) \tag{C.37}$$

$$\beta_{cm}(R_0) \;\rightarrow\; 0 \tag{C.38}$$

at certain point R_0, before the matrix $1-\beta(R)$ starts to be nearly singular and to continue the integration with the new quantities $f_m^{(c)}$, $\alpha(R)$, $\beta(R)$ according to the same scheme. If the matrix $1-\beta(R)$ starts to be singular after a few more steps, we can repeat the renormalization.

Bibliography

[1] M A Huels, J A Fedchak, R L Champion, L D Doverspike, J P Gauyacq, and D Teillet-Billy. Electron detachment in low-energy collisions of halogen anions with atomic hydrogen. *Phys. Rev. A*, 49(1):255–264, January 1994.

[2] A Chutjian, A Garscadden, and J M Wadehra. Electron attachment to molecules at low electron energies. *Phys. Rep.*, 264:393–470, 1996.

[3] K Rohr and F Linder. Vibrational excitation of polar molecules by electron impact I. Threshold resonances in HF and HCl. *J. Phys. B*, 9(14):2521–2537, 1976.

[4] W Domcke. Theory of resonance and threshold effects in electron-molecule collisions: The projection-operator approach. *Phys. Rep.*, 208(2):97–188, 1991.

[5] R J Bieniek. A source of errors in cross sections of curve-crossing processes. *J. Phys. B*, 13:4405–4416, 1980.

[6] C Mündel, M Berman, and W Domcke. Nuclear dynamics in resonant electron-molecule scattering beyond the local approximation: Vibrational excitation and dissociative attachment in H_2 and D_2. *Phys. Rev. A*, 32(1):181–193, July 1985.

[7] M Allan and S F Wong. Effect of vibrational and rotational excitation on dissociative attachment in hydrogen. *Phys. Rev. Lett.*, 41(26):1791–1794, December 1978.

[8] M Allan and S F Wong. Dissociative attachment from vibrationally and rotationally excited HCl and HF. *J. Chem. Phys.*, 74(3):1687–1691, February 1981.

[9] W Domcke. Projection-operator approach to potential scattering. *Phys. Rev. A*, 28(5):2777–2791, November 1983.

[10] R J Bieniek. Complex potential and electron spectrum in atomic collisions involving fast electronic transitions: Penning and associative ionization. *Phys. Rev. A*, 18(2):392–413, August 1978.

[11] O Schafer and M Allan. Measurement of near-threshold vibrational excitation of HCl by electron impact. *J. Phys. B*, 24:3069–3076, 1991.

[12] S Cvejanović. Threshold and resonant features in the vibrational excitation functions of hydrogen halides. In *Rev. at the 18th ICPEAC*, Aarhus, 1993.

[13] R Abouaf and D Teillet-Billy. Fine structure in dissociative-attachment cross sections for HCl and DCl. *J. Phys. B*, 10(11):2261–2268, 1977.

[14] R G Newton. *Scattering Theory of Waves and Particles.* Springer, Berlin, 1982.

[15] Taylor. *Scattering theory: the quantum theory of nonrelativistic collisions.* 1975.

[16] M Berman, C Mündel, and W Domcke. Projection-operator calculations for molecular shape resonances: The $^2\Sigma_u^+$ resonance in electron-hydrogen scattering. *Phys. Rev. A*, 31(2):641–651, February 1985.

[17] H Feshbach. A unified theory of nuclear reactions. II. *Annals of Phys.*, 19:287–313, 1962.

[18] W Domcke. Analytic theory of resonances, virtual states and bound states in electron-molecule scattering and related processes. *J. Phys. B*, 14:4889–4922, 1981.

[19] T F O'Malley. Theory of dissociative attachment. *Phys. Rev.*, 150(1):14–29, October 1966.

[20] A K Kazansky and S A Kalin. Semiclassical approximation in the non-local theory of resonance processes in slow collisions of two atoms and an electron. *J. Phys. B*, 23:809–819, 1990.

[21] A K Kazansky and S A Kalin. The semiclassical version of the non-local resonance theory of electron-molecule collisions. *J. Phys. B*, 23:4377–4400, 1990.

[22] M Movre and W Meyer. Theoretical investigation of the autoionization process in molecular collision complexes: Computational methods and applications to He$^*(2^3S)$+H(1^2S). *J. Chem. Phys.*, 106(17):7139–7160, May 1997.

[23] E P Wigner. On the behavior of cross sections near thresholds. *Phys. Rev.*, 73(9):1002–1009, May 1948.

[24] O H Crawford. Bound states of a charged particle in a dipole field. *Proc. Phys. Soc.*, 91:279, 1967.

[25] R G Gordon. New method for constructing wavefunctions for bound states and scattering. *J. Chem. Phys.*, 51(1), July 1969.

[26] R G Gordon. Constructing wavefunctions for nonlocal potentials. *J. Chem. Phys.*, 52(12), June 1970.

[27] J Horáček. Extrapolation technique for solution of scattering integral equations. *J. Phys. A*, 22:355–363, 1989.

[28] E Gillman and H R Fiebig. Accurate recursive generation of spherical Bessel and Neumann functions for a large range of indices. *Computers in Physics*, pages 62–72, February 1988.

[29] J Horáček, F Gemperle, and H.-D. Meyer. Calculation of dissociative attachment of electrons to diatomic molecules by the Schwinger-Lanczos approach. *J. Chem. Phys.*, 104(21):8433–8441, June 1996.

[30] H Morgner. The validity of the local approximation in Penning ionization as studied by model calculations. *Chem. Phys.*, 145:239–252, 1990.

[31] H.-D. Meyer, J Horáček, and L S Cederbaum. Schwinger and anomaly-free kohn variational principles and a generalized Lanczos algorithm for nonsymmetric operators. *Phys. Rev. A*, 43(7):3587–3596, April 1991.

[32] J Horáček and W Domcke. Calculation of cross sections for vibrational excitation and dissociative attachment in electron collisions with HBr and DBr. *Phys. Rev. A*, 53(4):2262–2271, April 1996.

[33] F Gemperle and J Horáček. Threshold peak structures in the vibrational excitation of HCl by low-energy electron impact. *Czech. J. Phys.*, 47(3):305–315, 1997.

[34] B A Lippmann and J Schwinger. Variational principles for scattering processes I. *Phys. Rev.*, 76:469–480, 1950.

[35] H-D Meyer and S Pal. A band-Lanczos method for computing matrix elements of a resolvent. *J. Chem. Phys.*, 91:6195, 1989.

[36] J Horáček and T Sasakawa. Method of continued franctions with application to atomic physics. *Phys. Rev. A*, 28:2151, 1983.

[37] J Horáček and T Sasakawa. Method of continued franctions with application to atomic physics. II. *Phys. Rev. A*, 30:2274, 1984.

[38] J Horáček and T Sasakawa. Method of continued fractions for on- and off-shell t matrix of local and nonlocal potentials. *Phys. Rev. C*, 32(1):70–75, July 1985.

[39] D Shanks. *J. Math. and Phys.*, 34:1, 1955.

[40] P Wynn. On a device for computing the $e_m(s_n)$ transformation. *Math. Tables Aids Comput.*, 10:91, 1956.

[41] P L Gertitschke and W Domcke. Time-dependent wave-packet description of dissociative electron attachment. *Phys. Rev. A*, 47(2):1031–1044, February 1993.

[42] W Domcke. Private communication.

[43] J H Black, A Porter, and A Dalgarno. The emission spectrum of H_2 from associative detachment and ultraviolet pumping. *Astrophys. J.*, 249:138–144, October 1981.

[44] A Herzenberg. Electron-detachment in slow collisions between atoms and negative ions. *Phys. Rev.*, 160(1):80–94, August 1967.

[45] J C Y Chen. Theory of atomic collisions with negative ions: Associative detachment. *Phys. Rev.*, 156(1):12–25, April 1967.

[46] J Mizuno and J C Y Chen. Theoretical investigation of complex potentials for atomic collisions. I. Numerical solution of model (H^-,H) collisions. *Phys. Rev.*, 187(1):167–192, November 1969.

[47] J M Wadehra and J N Bardsley. Vibrational- and rotational-state dependence of dissociative attachment in e-H_2 collisions. *Phys. Rev. Lett.*, 41(26):1795–1798, December 1978.

[48] N Bardsley and J M Wadehra. Dissociative attachment and vibrational excitation in low-energy collisions of electrons with H_2 and D_2. *Phys. Rev. A*, 20(4):1398–1404, October 1979.

[49] J M Wadehra. Dissociative attachment to rovibrationally excited H_2. *Phys. Rev. A*, 29(1):106–110, January 1984.

[50] R J Bieniek and A Dalgarno. Associative detachment in collisions of H and H^-. *Astrophys. J.*, 228:635–639, March 1979.

[51] A P Hickman. Dissociative attachment of electrons to vibrationally excited H_2. *Phys. Rev. A*, 43(7):3495–3502, April 1991.

[52] G A Gallup, Y Xu, and I I Fabrikant. Nonlocal theory of dissociative electron attachment to H_2 and HF molecules. *Phys. Rev. A*, 57(4):2596–2607, April 1998.

[53] J P Gauyacq. Dissociative attachment in $e^- - H_2$ collisions. *J. Phys. B*, 18:1859–1872, 1985.

[54] I F Schneider, C Strömholm, L Carata, X Urbain, M Larsson, and A Suzor-Weiner. Rotational effects in HD^+ dissociative recombination: Theoretical study of resonant mechanisms and comparison with ion storage ring experiments. *J. Phys. B*, 30:2687–2705, 1997.

[55] W Kołos and L Wolniewicz. Potential-energy curves for the $X^1\Sigma_g^+$, $b^3\Sigma_u^+$ and $C^1\Pi_u$ states of the hydrogen molecule. *J. Chem. Phys.*, 43(7):2429–2441, October 1965.

[56] A Dalgarno and A E Kingston. Van der Waals forces. *Proc. Phys. Soc. London*, 73:455–464, 1959.

[57] J Senekowitsch, P Rosmus, W Domcke, and H-J Werner. An accurate potential energy function of the H_2^- ion at large internuclear distances. *Chem. Phys. Lett.*, 111(3):211–214, November 1984.

[58] K Sakimoto. Ion-molecule reactions at extremely low energies: $H^-+H \to H_2+e$. *Chem. Phys. Lett.*, 164(2):294–298, December 1989.

[59] J M Launay, M Le Dourneuf, and C J Zeippen. The $H+H^- \leftrightarrow H_2(\nu, j) + e^-$ reaction: A consistent description of the associative detachment and dissociative attachment processes using the resonant scattering theory. *Astron. Astrophys.*, 252:842–852, 1991.

[60] A L Schmeltekopf, F C Fehsenfeld, and E E Ferguson. Laboratory measurement of the rate constant for $H^-+H \to H_2+e$. *Astrophys. J.*, 148:L155–156, June 1967.

[61] J C Browne and A Dalgarno. Detachment in collisions of H and H^-. *J. Phys. B*, 2:885–889, 1969.

[62] G J Schulz and R K Asundi. Isotope effect in the dissociative attachment in H_2 at low energy. *Phys. Rev.*, 158(1):25–29, June 1967.

[63] K Rohr and F Linder. Vibrational excitation in e^-+HCl collisions at low energies. *J. Phys. B*, 8:L200, 1975.

[64] F Fiquet-Fayard. Theoretical investigation of dissociative attachment in HCl and DCl. *J. Phys. B*, 7:810, 1974.

[65] W Domcke and L S Cederbaum. On the interpretation of low-energy electron-HCl scattering phenomena. *J. Phys. B*, 14:149–173, 1981.

[66] N Bardsley and J M Wadehra. Dissociative attachment in HCl, DCl, and F_2. *J. Chem. Phys.*, 78(12):7227–7234, June 1983.

[67] W Domcke and C Mündel. Calculation of cross sections for vibrational excitation and dissociative attachment in HCl and DCl beyond the local-complex-potential approximation. *J. Phys. B*, 18:4491–4509, 1985.

[68] P L Gertitschke and W Domcke. Time-dependent wave-packet dynamics with memory: The electron-HCl collision complex. *Z. Phys. D*, 31:171–179, 1994.

[69] I I Fabrikant. R-matrix theory of inelastic processes in low-electron collisions with HCl molecule. *Z. Phys. D*, 3:401–410, 1986.

[70] L A Morgan, P G Burke, and C J Gillan. Low-energy electron scattering by HCl. *J. Phys. B*, 23:99–113, 1990.

[71] I I Fabrikant, S A Kalin, and A K Kazansky. Inelastic processes in e-HCl collisions in the energy range including the dissociation threshold. *J. Chem. Phys.*, 95(7):4966–4971, October 1991.

[72] J P Gauyacq and A Herzenberg. Nuclear-excited Feshbach resonances in e^{-}+HCl scattering. *Phys. Rev.*, 25:2959, 1982.

[73] D Teillet-Billy and J P Gauyacq. Dissociative attachment in $e^{-}-$HCl, DCl collisions. *J. Phys. B*, 17:4041–4058, 1984.

[74] M A Morrison. Near-threshold electron-molecule scattering. *Adv. At. Mol. Phys.*, 24:51–156, 1988.

[75] J Horáček, W Domcke, and H Nakamura. Electron attachment and vibrational excitation in hydrogen iodide: Calculations based on the nonlocal resonance model. *Z. Phys. D*, 42:181–185, 1997.

[76] J P Gauyacq. Associative detachment in collisions between negative halogen ions and hydrogen atoms. *J. Phys. B*, 15:2721–2739, 1982.

[77] P-O Åstrand and G Karlström. A bound HCl^{-} species: An *ab initio* quantum-chemical study. *Chem. Phys. Lett.*, 175(6):624–628, December 1990.

[78] I I Fabrikant. Threshold behavior of the cross sections for scattering of electrons by polar molecules. *Sov. Phys. JETP*, 46(4):693–697, October 1977.

[79] J Horáček, M Čížek, and W Domcke. Generalization of the nonlocal resonance model for low-energy electron collisions with hydrogen halides: The variable threshold exponent. *Theor. Chem. Acc.*, 100:31–35, 1998.

[80] N T Padial and D W Norcross. Ro-vibrational excitation of HCl by electron impact. *Phys. Rev. A*, 29:1590, 1984.

[81] S V ONeil, P Rosmus, D W Norcross, and H-J Werner. Bound electronic states of HCl^{-}. *J. Chem. Phys.*, 85(12):7232–7240, December 1986.

[82] H-J Werner and P Rosmus. Theoretical dipole moment functions of the HF, HCl and HBr molecules. *J. Chem. Phys.*, 73:2319, 1980.

[83] J F Ogilvie, W R Rodwell, and R H Tipping. Dipole moment functions of the hydrogen halides. *J. Chem. Phys.*, 73:5221, 1980.

[84] H Bateman. On the numerical solution of linear integral equations. *Proc. R. Soc. London Ser. A*, 100:441, 1922.

[85] V Pless, B M Nestmann, and S D Peyerimhoff. Vibrational excitation and dissociative attachment in low-energy scattering from diatomic molecules. *J. Phys. B*, 25:4649–4659, 1992.

[86] G Knoth, M Gote, M Rädle, F Leber, K Jung, and H Ehrhardt. Electron impact rovibrational excitation close to threshold of the $\nu = 2$ and $\nu = 3$ levels of HF and HCl. *J. Phys. B*, 22:2797–2816, 1989.

[87] G Knoth, M Rädle, M Gote, H Ehrhardt, and K Jung. Near-threshold electron impact rovibrational excitation of HCl and HF. *J. Phys. B*, 22:299–326, 1989.

[88] M Rädle, G Knoth, K Jung, and H Ehrhardt. Rotational and rovibrational excitation of HCl and HF by low-energy electron impact. *J. Phys. B*, 22:1455–1476, 1989.

[89] M Čížek, J Horáček, and W Domcke. Nuclear dynamics of the H_2^- collision complex beyond the local approximation: Associative detachment and dissociative attachment to rotationally and vibrationally excited molecules. *J. Phys. B*, 31:2571–2583, 1998.

[90] C J Howard, F C Fehsenfeld, and M McFarland. Negative ion-molecule reactions with atomic hydrogen in the gas phase at 296°K. *J. Chem. Phys.*, 60(12):5086–5089, June 1974.

[91] P L Gertitschke. *Zeitabhängige Wellenpaket-Dynamik von Electron-Molekül-Stoßkomplexen.* PhD thesis, Institut für Physikalische und Theoretische Chemie der Technischen Universität München, 1992.

[92] F Thiel. Private communication.

[93] I I Fabrikant. Private communication.

[94] P Piecuch. Potential energy curves for the HF^- and CH_3F^- anions: A coupled cluster study. *J. Mol. Structure*, 436–437:503–536, 1997.

[95] M H Anderson, J R Enser, M R Matthews, C Wieman, and C A Cornell. Observation of Bose-Einstein condensation in a dilute atomic vapor. *Science*, 269, 1995.

[96] J J Blangé. *Ionization Processes in Thermal and Ultracold Collisions Between Sodium Atoms.* PhD thesis, Universiteit Utrecht, 1996.

[97] H Metcalf and P van der Straten. Cooling and traping of neutral atoms. *Phys. Rep.*, 244(4):203–286, August 1994.

[98] P A Molenaar. *PHOTOASSOCIATIVE REACTIONS OF LASER-COOLED SODIUM.* PhD thesis, Universiteit Utrecht, 1996.

[99] M W Müller, A Merz, M-W Ruf, H Hotop, W Meyer, and M Movre. Experimental and theoretical studies of the bi-excited collision systems $He^*(2^3S)$+$He^*(2^3S, 2^1S)$ at thermal and subthermal kinetic energies. *Z. Phys. D*, 21:89–112, 1991.

[100] R Broeke. Ab initio calculations on the potential energy curves and cross sections for the photodissociation $X^2\Sigma_u^+ \rightarrow A^2\Sigma_g^+$ of He_2^+. Master's thesis, Universiteit Utrecht, January 1998. Supervised by Henrik Rudolph and Morten Lundsgaard.

[101] A U Hazi. A purely L^2 method for calculating resonance widths. *J. Phys. B*, 11(8):L259–264, 1978.

[102] P van der Straten. Private communication.

[103] W H Miller. Theory of Penning ionization. i. atoms. *J. Chem. Phys.*, 52(7):3563–3572, April 1970.

[104] A Z Devdariani, V N Ostrovskii, and Y N Sebyakin. Crossing of quasistationary levels. *Sov. Phys. JETP*, 44(3):477–482, September 1976.

[105] R J Bieniek, M W Müller, and M Movre. Uniform stationary-phase methods for energy spectra resulting from collisions in a complex potential: Penning and associative ionization of $He^*(2^3S) + He^*(2^3S)$. *J. Phys. B*, 23:4521–4538, 1990.

[106] M Pieksma, G R Woestenenk, M van Rijnbach, D van Oosten, J W Thomsen, P van der Straten, and A Niehaus. Energy distributions of He^+ and He_2^+ ions formed in ultracold $He(2^3S_1)$+$He(2^3P_2)$ collisions. Euroconference on Slow COllisions between LAseR manipulated systems (ESCOLAR), Elounda, Crete, Greece, May 1999.

[107] A R Edmonds. *Angular Momentum in Quantum Mechanics.* Princeton University Press, revised printing of the second edition, 1968.

[108] M Abramowitz and I A Stegun, editors. *Handbook of Mathematical functions.* Dover Publications, Inc., New York, 1965.